Constraints on the Structure and Evolution of the Malawi Rift from Active- and Passive-Source Seismic Imaging

Natalie Jean Accardo

Submitted in partial fulfillment of the

requirements for the degree of

Doctor of Philosophy

in the Graduate School of Arts and Sciences

COLUMBIA UNIVERSITY

2018

Abstract

Constraints on the Structure and Evolution of the Malawi Rift from Active- and Passive-Source Seismic Imaging

Natalie Jean Accardo

Located at the southernmost sector of the Western Branch of the East African Rift System, the Malawi Rift exemplifies an active, magma-poor, weakly extended continental rift. This work focuses on the northern portion of the Malawi Rift, which is flanked by long (>100 km) basin-bounding border faults and crosses several significant remnant structures. This combination of characteristics makes the Malawi Rift the ideal location to investigate the controlling processes governing present-day extension throughout the lithosphere. To investigate these processes I image shallow basin- to uppermost-mantle structure beneath the region using a combination of passive- and active-source seismic datasets. I conduct passive-source imaging of the crust and upper mantle using ambient-noise and teleseismic Rayleigh-wave phase velocities between 9 and 100 s period. This study includes six lake-bottom seismometers located in Lake Malawi (Nyasa), the first time seismometers have been deployed in any of the African rift lakes. I utilize the resulting phase-velocity maps to invert for a shear velocity model of the Malawi Rift discussed below.

I utilize active-source tomographic imaging to obtain new constraints on rift basin structure in the Malawi Rift from a 3-D compressional velocity (Vp) model. The velocity model uses observations from the first wide-angle refraction study conducted using lake-bottom seismometers in one of the great lakes of East Africa. The 3-D velocity model reveals up to ∼5 km of synrift sediments, which smoothly transition from eastward thickening against the Livingstone Border Fault in the North Basin to westward thickening against the Usisya Border Fault in the Central Basin. I use new constraints on synrift sediment thickness to construct displacement profiles for both faults. Both faults accommodate large throws (>7

km) but the Livingstone Fault is ∼30 km longer. The dimensions of these faults suggest they are nearing their maximum size. The presence of >4 km of sediment within the accommodation zone suggests fault length was established early pointing the "constant length" model of fault growth. The presence of an intermediate velocity unit with velocities of 3.75-4.5 km/s is interpreted to represent prior rifting (Permo-Triassic and/or Cretaceous) sedimentary deposits beneath Lake Malawi. These thick (up to 4.6 km) packages of preexisting sedimentary strata improve the understanding of the Tanganyika-Rukwa-Malawi rift system and the role of earlier stretching phases on synrift basin development.

I use the previously obtained local-scale measurements of Rayleigh wave phase velocities between 9 and 100 s combined with constraints on basin structure and crustal thickness to robustly invert for shear velocity from the surface to 135 km for the Malawi Rift. We compare our resulting 3-D model to a 3-D model of shear velocity obtained for the mature Main Ethiopian Rift and Afar Depression using commensurate datasets and identical methodologies. Comparing the Vs models for the two regions reveals markedly different seismic velocities particularly pronounced in the upper mantle (average velocities in the Malawi Rift are ∼9% faster than the Main Ethiopian Rift). Our 3-D Vs model of the Malawi Rift reveals a strong, localized low velocity anomaly associated with the Rungwe Volcanic Province within the crust and upper mantle that can be explained without requiring the presence of partial melt. Away from the Rungwe Volcanic Province, velocities within the plateau regions are fast (>4.6 km/s) and representative of depleted lithospheric mantle to depths of 100 and >135 km to the west and east of the rift, respectively. Thinned lithosphere, represented by the absence of similarly high velocities, is centered directly beneath the rift axis and footwall escarpments of the rift basins. The correlation between the localization of lithospheric thinning, the boundaries between abutting Proterozoic mobile belts, and the positions of the basin-bounding border faults may point to the controlling role of preexisting large-scale structures in localizing strain and allowing extension to occur here.

Contents

List of Figures

List of Tables

Acknowledgements

I owe immeasurable gratitude to my two outstanding advisors Jim Gaherty and Donna Shillington who have acted as some of the best mentors a student could ask for. They have never wavered in their support of my endeavors whether I am asking them to go on yet another field excursion or to pursue a new scientific question. They have shown me unending kindness in guiding my way when I have gotten lost and inspiring me to persevere when I have encountered obstacles. I hope to one day emulate their remarkable scientific intuition when pursuing the joy of scientific discovery.

I owe special thanks to my third committee member Göran Ekström who early on remarked that I seemed fearless and has such inspired me to try and live fearlessly every day. His unending patience to answer questions carefully and thoughtfully whether they are big or small inspires me to try to acquire his excellent qualities as a professor and as a mentor. I also would like to thank my final two committee members Roger Buck and M. Beatrice Magnani. Roger's natural inquisitiveness inspires me to pursue every new question and to always step back and remember the bigger scientific context when interpreting data. I also owe great thanks to other researchers and faculty at Lamont who've held their doors open to me no matter the presence of an impending deadline or the nature of the scientific question: Bill Menke, Anne Bécel, Ben Holtzman, Connie Class, Paul Richards, Felix Waldhauser, Heather Savage, Meredith Nettles, and Maya Tolstoy.

Special thanks to my to peers and the postdocs at Lamont: Kira Olsen, Genevieve Coffey, Ge Jin, Yang Zha, Zach Eilon, Steve Veitch, James Gibson, Bridgit Boulahanis, Yen Joe Tan, Rachel Marzen, Mike Howe, Josh Russell, Anna Barth, Chris Carchedi, Emily Hopper, Chris Havlin, Lucia Gaultieri, Jean Arthur Olive, and Samer Naif. And of course my sisters

in seismology: Hannah Rabinowitz, Helen Janiszewski, and Celia Eddy. The three of you have made the hard times seem easy, the lonely times feel less lonely, and the good times great. I can't imagine graduate school without the three of you there along side me.

Finally, I would like to express my eternal gratitude to the unending love shown to me by my parents. They have supported me during this endeavor in every way possible. My success at Columbia could not have been found without their incredible support.

Dedication

I dedicate this work to my two late grandmothers, Jean Beckman and Jeanne Accardo, for whom I am named. While you passed before I began this epic endeavor I know that you would both be so proud of all that I've achieved. I will love and miss you forever.

1 Introduction

Since the onset of plate tectonics, more than 2.5 billion years ago, Earth's tectonic plates have been colliding and breaking apart in a cyclic pattern (*Wilson*, 1966). The intrinsic heat of the Earth drives these cycles through the transfer of energy from the convecting mantle into the overlying plates. Several cycles have occurred since the onset of plate tectonics with the present day configuration of the seven continents and five major oceans resulting from the last major breakup of a supercontinent, Pangea, beginning approximately 200 Myr ago (for a review see *Müller et al.*, 2016).

A fundamental component of plate tectonics is the breakup of previously intact continents whereby the stretching and subsequent thinning of the crust and mantle lithosphere ultimately leads to the formation of new ocean basins. The process of rifting results in high surface heat flow, sustained seismicity, extensive volcanism in some locations, and the formation of sedimentary basins that can host important hydrocarbon deposits. Understanding the mechanics of continental rifting is thus both societally relevant as well as important for a fundamental understanding of Earth processes. Despite the central role of continental rifting in plate tectonics, the mechanics of continental breakup is still not fully understood. Ongoing debate surrounds the role and nature of weakening mechanisms that allow continental rifting to initiate and proceed. Fundamentally, how is stretching of the continental crust and underlying mantle lithosphere accommodated when the continental plate is thick, cold, and strong? Diverse geophysical studies of magma-rich rift systems have established a strong context for the ability of melt products to weaken the lithosphere (e.g., *Armitage et al.*, 2015; *Ebinger and Scholz*, 2012; *Buck*, 2006; *Kendall et al.*, 2006). However, equal understanding

of the weakening mechanisms in magma-poor rift systems has yet to be found. Studies of such systems increasingly point to the controlling role of preexisting structures in localizing extensional strain, yet, identification of such large-scale structures is not ubiquitous and the scale-dependence of both the controls and the expressions of those controls are not well understood (e.g., *Corti et al.*, 2011; *Keranen et al.*, 2009; *Fagereng*, 2013; *Wilde-Piórko et al.*, 2010). Gaining access to basin- to mantle-scale expressions of continental extension in regions of limited magmatism and thick lithosphere is a critical step to better understanding this question.

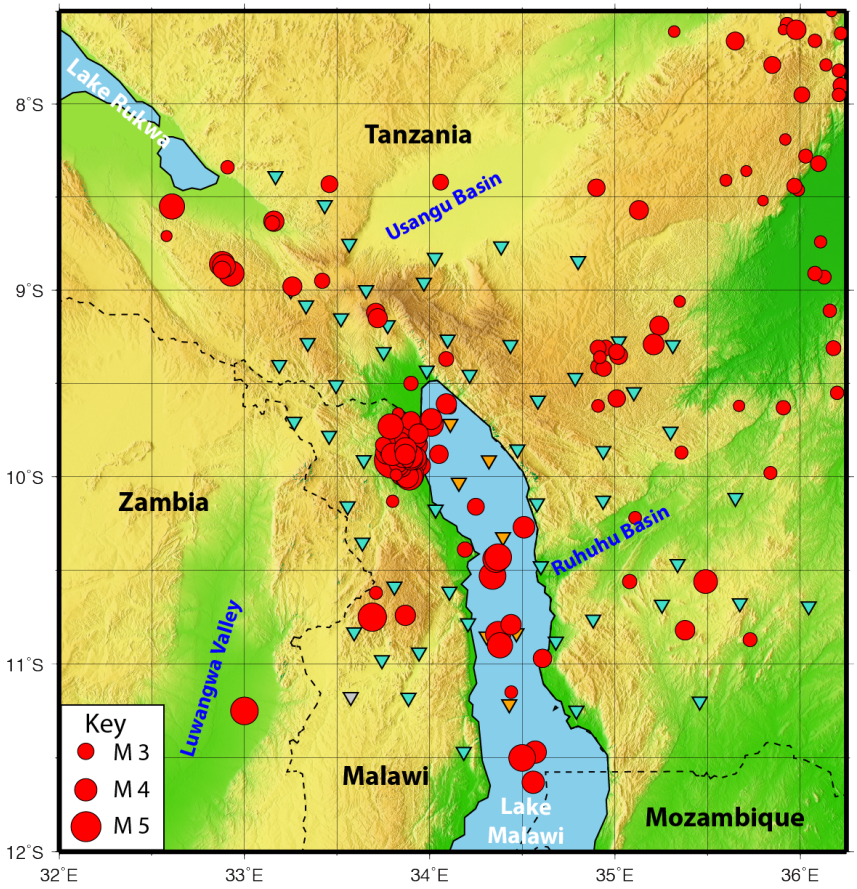

Figure 1.1: Topographic map of the northern Malawi Rift showing locations of interest, the distribution of seismicity (red circles)(*Mulibo and Nyblade*, 2016), and the locations of seismic stations (triangles) used in this study. The size of the circles represents earthquake magnitude. Turquoise triangles show the locations of the onshore SEGMeNT stations and orange triangles show the locations of the offshore SEGMeNT broadband stations. Grey triangles show the locations of the three Malawi Seismic Network stations.

One of the most spectacular active continental rifts today is the East African Rift System (EARS). The EARS incorporates long rift valleys situated within diverse terranes that transition from incipient seafloor spreading in the north to the very earliest stages of breakup in the south. My thesis focuses on one of the most enigmatic sectors of the EARS, the Malawi Rift (Fig.1.1), which is characterized by a succession of rift basins bounded by long normal faults of alternating polarity (termed border faults) (*Ebinger et al.*, 1987; *Scholz*, 1989), thick and strong lithosphere (e.g., *Ebinger et al.*, 1999; *Pérez-Gussinyé et al.*, 2009; *Stamps et al.*, 2014), deep crustal to upper mantle seismicity (e.g., *Craig et al.*, 2011), and limited magmatism (e.g., *Furman*, 2007). The Malawi Rift represents the southernmost segment of the Western Rift of the EARS and like other Western Rift systems, is filled by a narrow and deep rift lake, Lake Malawi.

Numerous techniques are available to probe the evolution of continental rift systems, with seismic observations representing one of the best methods to constrain Earth structure from the shallow depths of extensional sedimentary basins all the way the core-mantle boundary where mantle plumes may originate. In this thesis, I present results from active- and passive-source seismic imaging of the Malawi Rift to constrain 3-D rift system structure. In Chapters 2 and 4 passive-source imaging from surface waves constrains the crust to upper mantle structure, and in Chapter 3, active-source imaging constrains detailed basin-scale structure. The images of seismic velocity produced by this work are leveraged to constrain the temperature/composition of the crust and upper mantle, faulting in the upper crust and resulting basin formation, and the presence and influence of preexisting structures throughout the lithosphere in this system. Techniques to invert seismic observables (like surface wave phase velocities and body wave arrival times) are typically non-linear, limiting access to accurate estimation of model uncertainty and can suffer from influences in the choice of starting models. To minimize these influences, in Chapters 3 and 4, I wrap standard inversion methods inside of Monte Carlo techniques to invert a family of diverse, randomized starting models. Inverting a family of starting models allows direct access to error estimation

through quantification of model posterior variance.

The SEGMeNT (Study of Extension and maGmatism in Malawi aNd Tanzania) is a multidisciplinary study focused on the weakly-extended Malawi Rift (*Shillington et al.*, 2016). The goal of this experiment is to constrain the controls on tectonic segmentation (the subdivision of the rift into discrete basins) and magmatism in the Malawi Rift from geochemical, geodetic, magnetotelluric, and active- and passive-source seismic observations. Uniquely, the seismic component of this work "stepped into the lake" and combined 32 (short and long period) offshore instruments within Lake Malawi with a broader array of 55 instruments onshore to blanket the study area. The lake-bottom instruments represent some of the first seismometers ever deployed in a fresh water environment. Analysis of the noise characteristics of the lake-bottom seismometers show that noise-levels in the lake are lower than that of shallow oceanic environments and allow successful application of compliance corrections and instrument orientation determination.

In Chapter 2, I implement an array-based technique (Automated Surface Wave Measuring System) (*Jin and Gaherty*, 2015) to calculate maps of teleseismic Rayleigh wave phase velocity across the study region. Analysis of earthquake-derived Rayleigh waves are limited to intermediate and longer periods (>25 s) due to degraded signal at high-frequencies. Measurements at these periods are sensitive to deep crustal and upper mantle structure. To constrain shallow structure, I augment these measurements with estimates of Rayleigh wave phase velocity derived from the ambient wavefield. Measurements of ambient-noise Rayleigh waves have gained significant popularity in the last 15 years (e.g., *Bensen et al.*, 2007) because they provide high-resolution imaging of shallow earth structure. Combining measurements from ambient-noise and teleseismic Rayleigh waves provides robust estimates of phase velocity over a broad period band (9-100 s), which provide constraints on shallow crust through upper mantle structure.

To constrain basin-scale structure, in Chapter 3, I present results from a 3-D first-arrival time tomography model of Lake Malawi from refraction imaging. The refracted waves uti-

lized in this work were generated from airgun sources on the *M/V* Katundu in Lake Malawi and recorded on the array of 32 lake-bottom seismometers. To generate a smooth 3-D velocity model of basin-scale structure, I picked more than 100,000 first arrivals and inverted them using the iterative first-arrival tomographic inversion code FAST (First Arrival Seismic Tomography; *Zelt and Barton*, 1998). I implement a Monte Carlo approach and invert 200 unique initial models to create a posterior distribution of acceptable models (e.g., *Delescluse et al.*, 2015; *Korenaga et al.*, 2000; *Watremez et al.*, 2015). The primary result of this work was the first ever 3-D image of basin-scale structure for the Malawi Rift. This chapter produces estimates of sediment distribution along the basin-bounding border faults that can be combined with measurements of onshore elevation to calculate fault displacement profiles. The resulting estimates of fault throw represent some of the only estimates of fault displacement for faults of such significant length (>140 km). Additionally, I identify packages of higher velocity sediment that are found to be co-located with onshore outcrops of preexisting rift basins (formed in the Late Paleozoic and the Cretaceous). This observation points to large-scale preexisting extensional structures underlying the Malawi Rift.

In Chapter 4, I utilize these newly constrained 3-D distributions of sediment thickness from Chapter 3 and maps of phase velocity from Chapter 2 to invert for shear velocity structure (velocity varying with depth). We invert for absolute shear velocity which has the advantage of allowing direct access to estimates of temperature, composition, and the presence of fluids. The primary observation from this work is a strong, localized, velocity anomaly associated with the volcanic province as well as distinct changes in lithospheric structure across the axis of the rift that correlate well with boundaries between disparate Proterozoic terrains. Robust but lower-magnitude low-velocity anomalies follow the trace of the Malawi Rift and extend beneath the footwall escarpments and are interpreted to represent lithospheric thinning beneath the rift. The correlation between the locations of maximum thinning and the locations of the border faults in both basins points to the potential role of a single controlling mechanism like the role of abrupt changes in lithospheric thickness or

large-scale weaknesses. We compare these models of velocity structure in the Malawi Rift to models of shear velocity beneath the Main Ethiopian Rift (MER) and Afar Depression using the same measurement techniques. Our results show that the distributions of upper mantle velocity between these two rift systems are clearly distinct. In line with previous work (e.g., *Bastow et al.*, 2010; *Gallacher et al.*, 2016; *Kendall et al.*, 2005), our results illustrate the magma-rich nature of the Ethiopian upper mantle and in contrast, reveal that the upper mantle beneath the Malawi Rift likely is likely largely melt-free.

The goal of this thesis is to constrain the controlling mechanisms that have allowed rifting to initiate and proceed in the Malawi Rift and more broadly, magma-poor rift systems as a whole. By combining onshore and offshore instruments with robust tomographic techniques for shallow basin-scale to upper mantle scale structure, we show that the Malawi Rift is situated at the juncture between distinct and thick lithospheric blocks that host significant and likely deeply penetrating faults. Velocities away from the volcanic center are high and minimize the possibility of partial melt as the governing weakening mechanism that has allowed extension to initiate here. The secret to the extension of the Malawi Rift likely lies in the structures that built the system hundreds of millions of year ago.

2 Surface-wave imaging of the weakly-extended Malawi Rift from ambient-noise and teleseismic Rayleigh waves from onshore and lake-bottom seismometers

Co-authors: J. B. Gaherty, D. J. Shillington, C. J. Ebinger, A. A. Nyblade, G. J. Mbogoni, P. R. N. Chindandali, R. W. Ferdinand, G. D. Mulibo, G. Kamihanda, D. Keir, C. Scholz, K. Selway, J.P. O'Donnell, G. Tepp, R. Gallacher, K. Mtelela, J. Salima, A. Mruma

This chapter has been published: *Accardo, N. J. et al. (2017), Surface wave imaging of the weakly extended Malawi Rift from ambient-noise and teleseismic Rayleigh waves from onshore and lake-bottom seismometers, Geophys. J. Int., 209(3), 1892-1905, doi:10.1093/gji/ggx133..*

Abstract: Located at the southernmost sector of the Western Branch of the East African Rift System, the Malawi Rift exemplifies an active, magma-poor, weakly extended continental rift. To investigate the controls on rifting, we image crustal and uppermost mantle structure beneath the region using ambient-noise and teleseismic Rayleigh-wave phase velocities between 9 and 100 s period. Our study includes six lake-bottom seismometers located in Lake Malawi (Nyasa), the first time seismometers have been deployed in any of the African rift lakes. Noise-levels in the lake are lower than that of shallow oceanic environments and allow successful application of compliance corrections and instrument orientation determina-

tion. Resulting phase-velocity maps reveal slow velocities primarily confined to Lake Malawi at short periods (T <= 12 s), indicating thick sediments in the border-fault bounded rift basin. The slowest velocities occur within the Central Basin where Malawi Rift sedimentary strata may overlie older (Permo-Triassic) Karoo group sediments. At longer periods (T >25 s) a prominent low-velocity anomaly exists beneath the Rungwe Volcanic Province at the northern terminus of the rift basin. Estimates of phase-velocity sensitivity indicates these low velocities occur within the lithospheric mantle and potentially uppermost asthenosphere, suggesting that mantle processes may control the association of volcanic centers and the localization of magmatism. Beneath the main portion of the Malawi Rift, a modest reduction in velocity is also observed at periods sensitive to the crust and upper mantle, but these velocities are much higher than those observed beneath Rungwe.

2.1 Introduction

A fundamental question in continental dynamics asks how strong lithospheric plates rupture, given the modest magnitude of available tectonic forces (i.e., slab pull and ridge push) (e.g., *Bott*, 1991; *Forsyth and Uyeda*, 1975). Lithospheric strain localization and strength reduction during early-stage rifting is achieved in models that include weakening mechanisms like magmatic intrusions to enable continental rupture (*Buck*, 2004, 2006). In the past two decades, field, laboratory, and modeling studies of mature continental rift systems increasingly point to the influential role of melt products on the evolution of continental rifting (e.g., *Bastow and Keir*, 2011; *Buck*, 2006; *Corti et al.*, 2003; *Dugda et al.*, 2005; *Ebinger and Casey*, 2001; *Kendall et al.*, 2005; *Armitage et al.*, 2015). However, many ancient and active rift systems display evidence of volumetrically limited magmatic activity, for example the Western Branch of the East African Rift System (EARS) (*Furman*, 2007) and the Newfoundland-Iberia rifted margins (e.g., *Van Avendonk et al.*, 2009; *Whitmarsh et al.*, 2000). To shed light on extensional processes in an immature rift, including the controls of magmatism on extension, the SEGMeNT (Study of Extension and maGmatism in Malawi

aNd Tanzania) experiment acquired a suite of datasets including GPS, active- and passive-source seismic, geochemical, and magnetotelluric data across the Malawi Rift (*Shillington et al.*, 2016) where volcanism is restricted to the northern axial termination. Data from the Southern Lake Tanganyika Experiment (TANGA) are used to help constrain structure

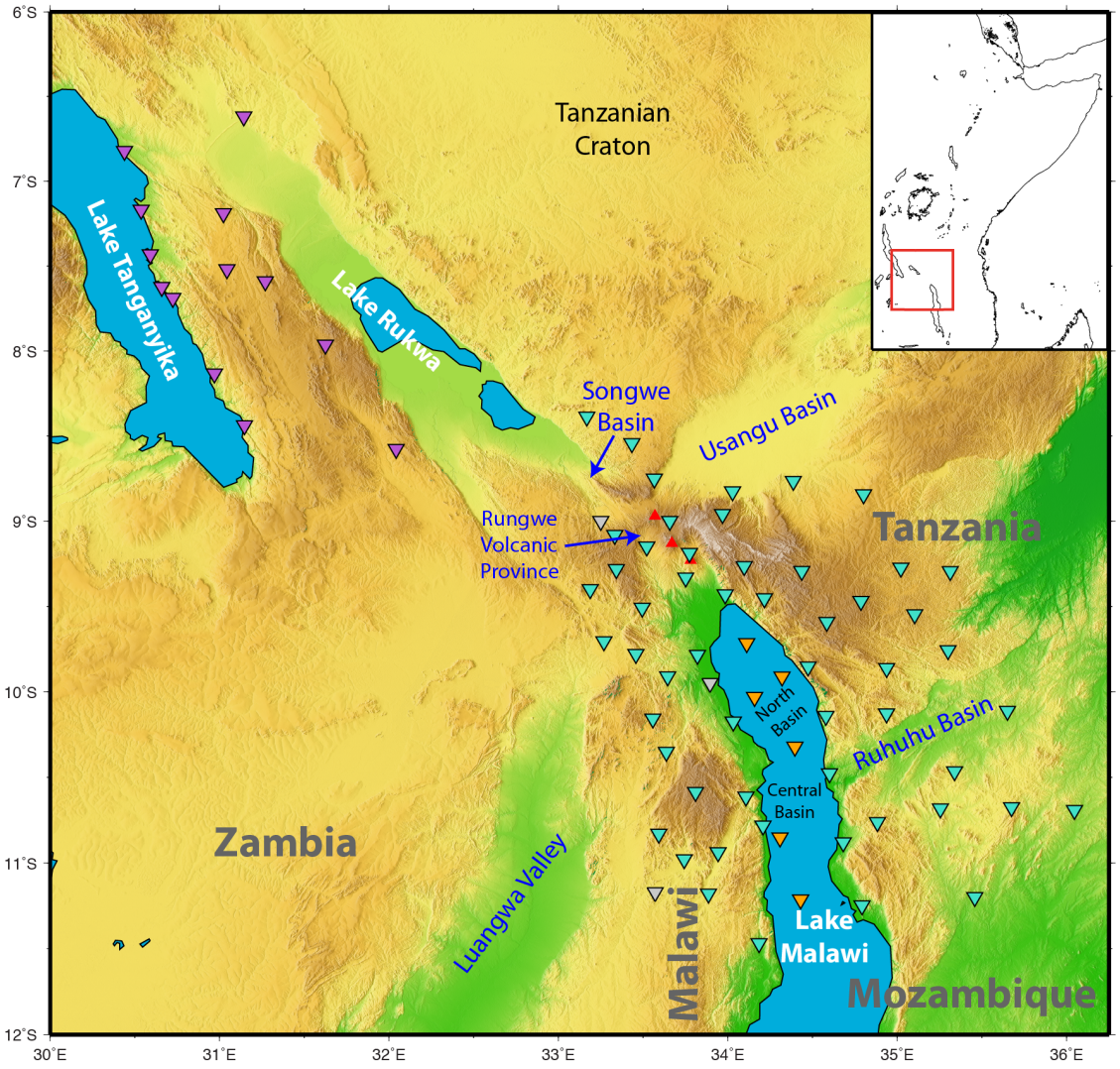

Figure 2.1: Map of the Malawi-Rukwa region with major tectonic features labeled. Inset map shows location of the study region. Upside-down triangles indicate the locations of the four seismic arrays used in this study: purple - TANGA, turquoise - SEGMeNT onshore, orange - SEGMeNT offshore, grey - Africa Array, Malawi Seismic Network. Red triangles represent the locations of the three volcanoes of the Rungwe Volcanic Province (RVP).

beyond the northern limits of the Rungwe Volcanic Province (RVP). Our study presents the first locally constrained seismic tomographic maps of surface-wave phase velocity of the

Malawi Rift with the aim of illuminating crust and upper-mantle structure beneath the region.

2.2 Tectonic Setting

The Malawi Rift, located in the southernmost sector of the EARS, is a seismically active, magma-poor, weakly-extended continental rift. The Malawi Rift extends over 800 km from the RVP in the north to the Urema Graben (Mozambique) in the south (Fig. 2.1). Lake Malawi (Nyasa) covers approximately 550 km of the rift axis, and is a type example of a narrow and deep East African rift lake. The Malawi Rift shares many similarities with other Western Branch rift basins, including strong lithosphere with deep seismicity (*Craig et al.*, 2011; *Ebinger et al.*, 1989; *Fagereng*, 2013; *Jackson and Blenkinsop*, 1993a), limited surface magmatism (*Furman*, 2007), and asymmetric border-fault-bounded half grabens with polarities that vary along the rift (*Crossley and Crow*, 1980; *Rosendahl et al.*, 1992).

The border-fault-bounded half grabens partition Lake Malawi into three basins (North, Central, and South) linked via complex transfer zones (*Scholz*, 1989). These basins developed within Proterozoic mobile belts, with the eastern boundary of Lake Malawi abutting the juncture between the Irumide Belt to the west and the Mozambique and Ubendian belts to the north and east (e.g., *Begg et al.*, 2009; *Chorowicz*, 2005). Fault-bounded depressions to the west and east of the Central Basin (Luangwa Valley and Ruhuhu Basin, respectively) represent Karoo rift basins (e.g., *Catuneanu et al.*, 2005) formed in the Late Carboniferous associated with early Gondwana breakup (*Wopfner*, 2002, 1994). Little stretching is thought to have occurred in the Malawi Rift with crustal stretching estimates from flexural models of basin and flank morphology and fault reconstructions suggesting <20% (*Ebinger et al.*, 1987). Furthermore, data from a single GPS within the Malawi Rift estimates a plate-opening velocity of ca. 1 mm/yr (*Saria et al.*, 2014).

The RVP at the northern end of the Malawi Rift is one of four volcanic centers within the Western Branch of the EARS (*Furman*, 2007) and represents the southernmost expression of volcanism in the entire rift system. The RVP sits within the complex accommodation zone

between the Malawi, Rukwa, and the apparently inactive Usangu rifts. Three volcanoes within the RVP (from north to south : Ngozi, Rungwe, and Kyejo, Fig. 2.1) have erupted in the past 10 Ka (*Ebinger et al.*, 1989; *Fontijn et al.*, 2012, 2010a,b). Debate continues concerning the relative timing of the onset of rifting within the Rukwa-Malawi rift zones, owing to the lack of deep drill data. Magmatism in the RVP may have commenced as early as 25 Ma (*Roberts et al.*, 2012), much earlier than the onset of faulting estimated at 8.6 Ma (*Ebinger et al.*, 1993b) along the northern basin bounding fault (*Ebinger et al.*, 1989).

Previous seismic investigations of the Malawi Rift have been limited to the extremes of the spatial spectrum: basin-scale investigations of Lake Malawi's shallow stratigraphy (e.g., *Scholz and Rosendahl*, 1988; *Specht and Rosendahl*, 1989), and regional- to continental-studies of the entire EARS (e.g., *Weeraratne et al.*, 2003; *Pasyanos and Nyblade*, 2007; *Fishwick*, 2010). Recent regional-scale studies using surface and body waves image a circular low-velocity region centered on the RVP within the uppermost mantle, which weakens and becomes more diffuse at greater depths (∼140 km) (*Adams et al.*, 2012; *Mulibo and Nyblade*, 2013; *O'Donnell et al.*, 2013)). The Pn/Sn study of *O'Donnell et al.* (2016) attribute the RVP low-velocity anomaly to pervasive thermal alteration of the uppermost mantle and potentially the presence of melt. These larger-scale studies lack the resolution to delineate the detailed structure of the low-velocity region and the degree to which it extends south into the Malawi rift basin, and to characterize the crustal and upper mantle manifestation of the rift. The combined SEGMeNT and TANGA experiments include a unique broadband seismic array that utilizes onshore and offshore instrumentation to span the RVP and Lake Malawi. Rayleigh waves traversing the array provide unsurpassed sampling of crustal and upper-mantle structure across the Malawi Rift.

2.3 Data and Methods

We collected Rayleigh waves derived from both ambient-noise and teleseismic earthquakes recorded on the onshore/offshore SEGMeNT and onshore TANGA stations (Fig. 2.1). Com-

bined, these two temporary networks provide 72 intermediate-period and broadband seismometers with a total array aperture of ∼400 km. The utilization of both ambient-noise and earthquake-generated Rayleigh waves to constrain Earth structure is increasingly employed due to the complementary nature of the two datasets (e.g., *Jin et al.*, 2015). Ambient-noise surface waves allow access to shorter periods where regional and teleseismic surface waves become attenuated and scattered, while earthquake observations provide considerably higher SNR at longer periods (∼ >25 s) where ambient-noise observations commonly suffer from decreased quality.

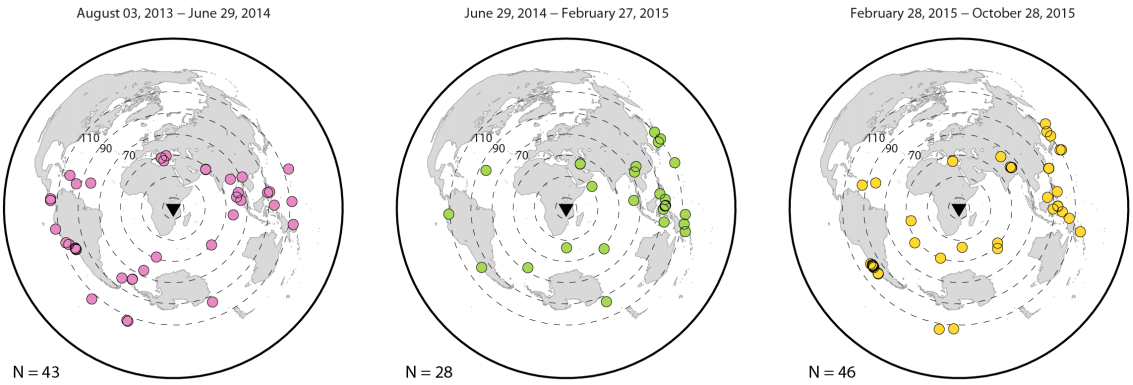

Figure 2.2: Event distribution used in this study. The distribution of events is shown for the three time periods of interest for the SEGMeNT study. August 3rd, 2013- June 29th, 2014: Deployment of initial 13 instruments in the Rungwe/Tukuyu area. June 29th, 2014 - February 27th, 2015: Addition of 42 broadband stations in Malawi and Tanzania. February 28th - October 28th, 2015: Addition of six broadband LBS in Lake Malawi. The entire array was pulled out by October 28th, 2015. Locations of events are shown by the circles, and the study region is shown by the triangle. All events were above a magnitude (Mw) 6.0 and occurred at depths <50 km. The number of events for each time period are shown in the bottom left of each panel.

2.3.1 Earthquake Processing: Determination of dynamic and structural phase velocity

We measured Rayleigh-wave phase velocities between 20-100 s from regional and teleseismic records. We initially selected all events (total of 141) with Mw greater than 6.0 between epicentral distances of 5°and 115°and depths <50 km. All events selected were visually in-

spected for quality and were required to have been recorded on a minimum of 7 stations. This has resulted in the inclusion of a total of 117 earthquakes that are well distributed in azimuth in the final phase-velocity images (Fig. 2.2). An example of a high-quality event can be seen in Fig. 2.3(a).

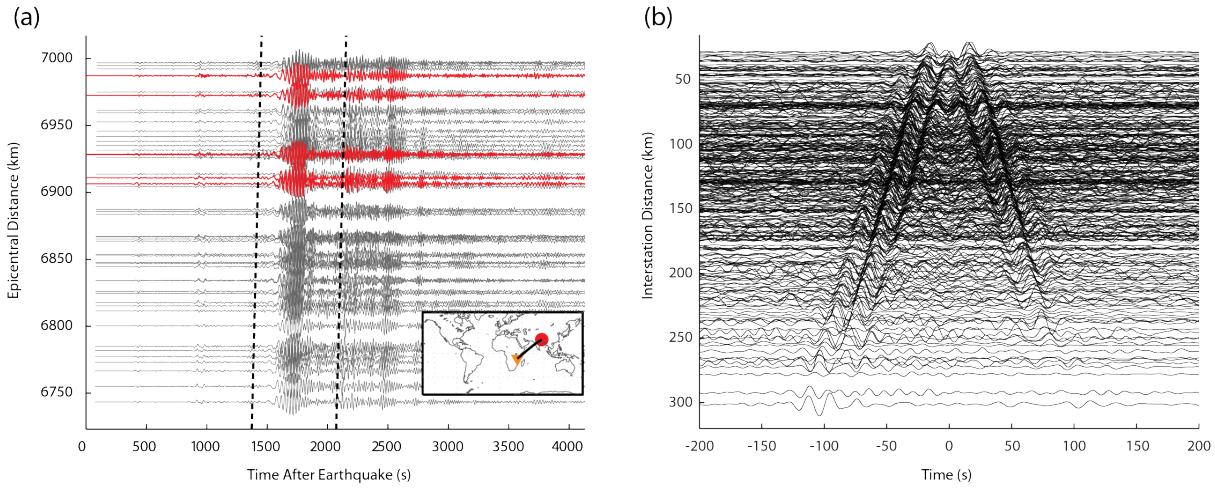

Figure 2.3: Examples of teleseismic (a) and ambient-noise (b) Rayleigh waves used in this study. (a) Record section from the Mw 7.8 event on April 25th, 2015. Location of the event (red circle) and seismic array (orange triangle) are shown in the inset. Grey: onshore stations; Red: lake bottom seismometers. Data have been filtered from 10-100 s. Dashed black lines show the time window used for the surface wave analysis. (b) Ambient noise cross-correlation functions in the time domain for all stations pairs that include a lake bottom seismometer. Data have been filtered from 8-25 s.

We utilize the multi-channel cross-correlation technique of *Jin and Gaherty* (2015) that leverages the coherency between traces from nearby stations to determine Rayleigh-wave phase velocity. This method recovers frequency-dependent phase and amplitude information via the narrow-band filtering of the broadband (10-150 s) cross-correlation function (CCF) between the vertical-component seismic trace from a given station and time-windowed traces from all stations where interstation distances were between 20 - 200 km. For this study, the filters were constructed as zero-phase Gaussian filters centered at 20, 25, 32, 40, 50, 60, 80, and 100 s and a bandwidth of 10% of the center frequency. The phase and amplitude information is determined by fitting the narrow-band filtered CCF with a Gaussian wavelet characterized by 5 parameters: the positive scale factor A, the center frequency ω_s, the

half-bandwidth θ_s, the group delay t_g, and the phase delay t_p.

Assuming that the broadband seismograms recorded at nearby stations are similar, the network of multi-channel phase delays (t_p) provide highly precise, robust constraints on the spatial variation of phase speed. To remove the influence of poor quality seismic traces, we estimate the coherence between waveforms from nearby stations at a series of frequencies. For this study we include only those measurements with coherence >0.5. We further test for outlying phase observations (potentially resulting from poor signal quality or undetected cycle-skipping) by comparing each measurement to that predicted from the average apparent phase velocity for a given frequency across the entire network. We discard individual phase delay measurements ($\sim$2%) with outlying values that would require greater than 20% perturbation to the predicted determined reference value. Additionally, we minimize the likelihood of erroneous phase measurements arising from cycle-skipping by limiting available station pairs to those with interstation distances <200 km. This length-scale is less than three-times the wavelength of the shortest period teleseismic Rayleigh wave (20 s).

At each frequency, we invert the network of phase delays for spatial variations in dynamic phase velocity via the Eikonal equation (*Lin et al.*, 2009). We tested the influence of smoothness choices on the inversion for individual event results and also on the final stacked solutions. To stabilize the inversion for individual event phase-velocity maps we applied a smoothness constraint that minimizes the second derivative of the slowness vector calculated from derived maps of phase delay. The weight of the smoothness constraint was chosen based on the frequency of interest and after testing the influence of smoothness on data fit. We applied the same weighting parameters to all events. After stacking all individual event results, we smooth the resulting phase velocity map based on the wavelength of the frequency of interest. We set the length of smoothing to be 25% of the average wavelength at each frequency.

We next correct for the influence of focusing and defocusing of the wave field via Helmholtz tomography (*Lin and Ritzwoller*, 2011), producing maps of structural phase ve-

locity at each frequency for each event. After applying strict quality control standards to each individual event result (discussed below), final event solutions are stacked to obtain robust structural phase velocity estimates at all periods at every grid point within the array. Additional information concerning the determination of structural phase velocity (i.e., standard deviation of the resulting phase velocity maps and the total number of crossing interstation paths) can be found in Appendix A.

The Helmholtz equation is given by

$$\frac{1}{c(\overrightarrow{r})^2} = \frac{1}{c'(\overrightarrow{r})^2} - \frac{\nabla^2 A(\overrightarrow{r})}{A(\overrightarrow{r})\omega^2} \tag{2.1}$$

where c is the structural phase velocity, c' is dynamic phase velocity, A is the amplitude field, ω is angular frequency, and $\overrightarrow{r}$ is the path connecting two stations. Henceforth we call this amplitude-correction term applied to the dynamic phase velocity as the "correction term". *Jin and Gaherty* (2015) discuss several complexities inherent in the construction of this correction term including ensuring smoothness in the amplitude field, smoothness in the resulting Laplacian of the amplitude field, and avoiding the influence of site-specific amplification effects. In the ideal case all stations in an array would have a site amplification term of unity. However, variations in local geology or instrument and/or installation conditions can cause amplification terms to deviate away from unity causing the resulting amplitude and correction terms to be biased.

To minimize such biases, we first correct event-specific amplitude fields with estimated station amplification terms prior to applying Helmholtz tomography. We calculate the median normalized amplitude value for a given station across all events, where normalized amplitude is calculated as a station's amplitude measurement normalized by the median of all amplitude measurements for the network for that event. Figure 2.4 shows an example of the resulting station amplification terms. We then normalize individual event amplitude measurements for a given station prior to constructing the event-specific amplitude field and correction term.

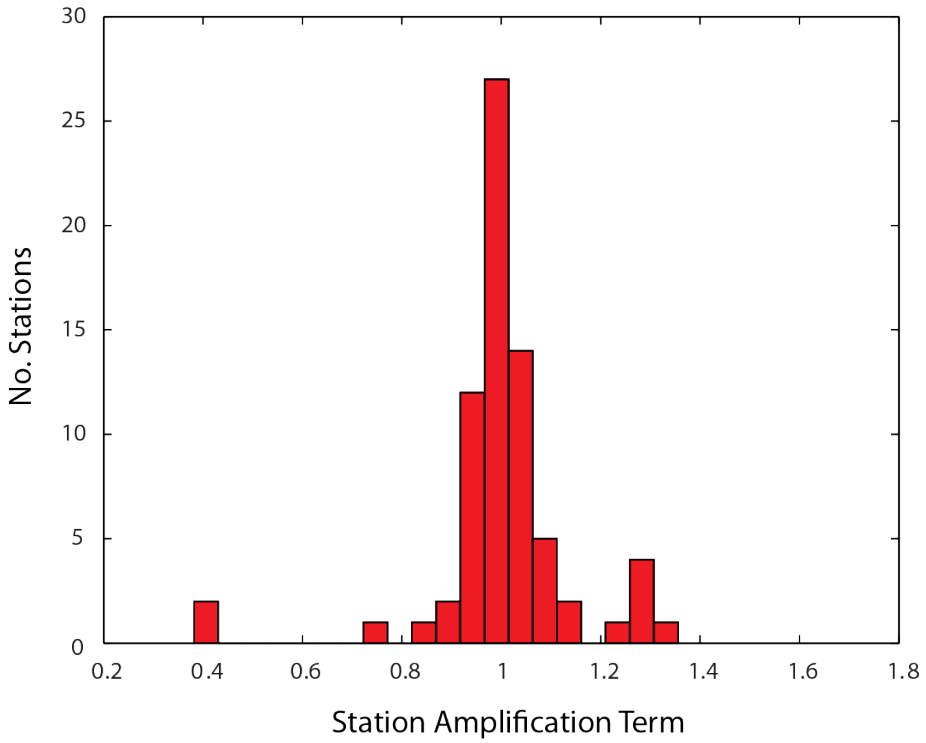

Figure 2.4: Example of determined station amplification terms at 40 s for entire network. The majority of the amplification terms hover around the expected value of 1. Stations with amplification terms >2 or <0.2 were not corrected for and their amplitude measurements were not used in determining the final structural phase velocity. The two stations with amplification terms of ~ 0.4 are VWZM and KIFA. VWZM exhibits an amplification value at all periods of ~ 0.4 which is related to uncertainties in the instrument response.

Quality control checks are also applied prior to the construction of the amplitude field. We reject amplitude measurements greater than or less than a period dependent factor of the median amplitude calculated for all stations within 200 km of the station of interest for each event. We chose this factor to be 2 at periods less than 60 s and 1.6 at periods greater than or equal to 60 s. This variation was determined after testing the influence of different values for the allowed amplification factor and identifying the value that would best reject outliers while maintaining realistic variations in the amplitude field.

2.3.2 Ambient Noise Processing

We conducted ambient noise processing following the technique of *Menke and Jin* (2015), which aims to estimate the phase velocity from ambient-noise cross-correlograms in the fre-

Table 2.1: Water depths and locations of LBS used in this study. LBS are ordered from shallowest to deepest in terms of water depth.

LBS	**Water Depth (m)**	**Latitude**	**Longitude**
103B	265	-9.716	34.112
203B	312	-10.031	34.158
206B	402	-9.912	34.32
110B	485	-10.322	34.396
302B	512	-10.853	34.31
118B	605	-11.214	34.43

quency domain (termed cross-spectra) via waveform fitting using Aki's formula. We cut all available continuous data into three-hour-long windows with 50% overlap, filtered the traces between 2-100 s, applied an amplitude normalizing procedure to reduce the effects of earthquakes and other discrete signals (*Bensen et al.*, 2007), and applied spectral whitening. Cross-correlating these traces for all available stations with interstation distances >20 km produced cross-spectra for 4,200+ station pairs. Coherent Rayleigh waves are observed for nearly all stations including the lake-bottom instruments (Fig. 2.2b). We invert individual station-pair dispersion curves for maps of Rayleigh-wave phase velocity between 9-25 s following the inversion procedure used in *Zha et al.* (2014). This method performs the tomographic inversion via a generalized least-squares algorithm. We tested the influence of damping/smoothness choices in the inversion step and chose those parameters that provided the best fit to the data while maintaining realistic variations in phase velocity. Further information concerning the tomographic inversion of the ambient noise data (i.e., checkerboard tests for resolution, maps of the number of raypaths per grid cell, and a comparison of the predicted phase velocity from the earthquake processing and ambient noise processing) can be found in Appendix A.

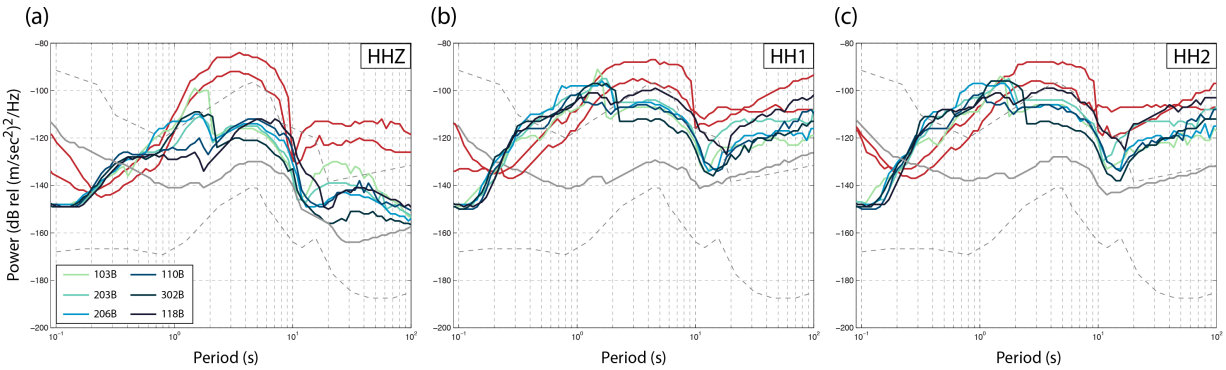

Figure 2.5: Comparison of noise power spectra for the 6 LBS in this study (light green to black lines), 2 Cascadia Initiative shielded OBS at $\sim$ 350 m water depth (red), and a representative onshore SEGMeNT station SCH (grey). The colored lines show the average power spectra over 8 months for all instruments. The dashed grey lines indicate the Peterson high- and low-noise models. Spectra were acquired from the Modular Utility for STAtistical kNowledge Gathering (MUSTANG) system (*Ahern et al.*, 2015). The spectra are shown for the (a) vertical component (HHZ), (b) horizontal component 1 (HH1), and (c) horizontal component 2 (HH2). The LBS are colored according to water depth with the lightest colors representing the shallowest instruments (see inset in (a)). LBS water depths are given in Table 2.1.

2.4 Special Considerations for Lake Bottom Seismometers (LBS)

The addition of 6 broadband LBS to the SEGMeNT experiment provides consistent station spacing across the axis of the Malawi Rift which lies beneath Lake Malawi (Fig. 2.1). This experiment is one of the only deployments of ocean-bottom-seismometers (OBS) in a freshwater, lake environment. Additionally, Lake Malawi, as with other large African rift lakes, is characterized by a permanent temperature-induced density stratification and is anoxic below $\sim$220 m (*Vollmer et al.*, 2005). Here we present the first attempt to apply standard OBS processing techniques like compliance/tilt corrections and determination of instrument orientation to data acquired on instruments deployed in a lake. We apply these corrections prior to estimating phase velocity in the teleseismic band but find that the corrections are not required in the ambient noise period band (see below).

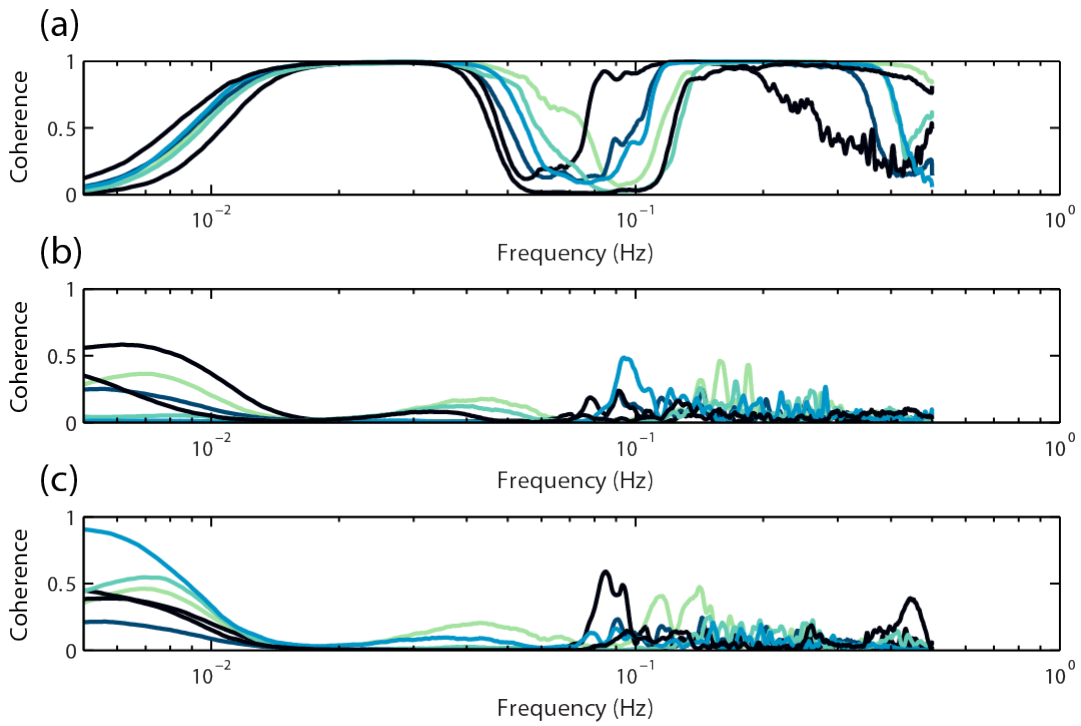

Figure 2.6: Coherence between the vertical component and the differential pressure gauge (a), horizontal component 1 (b), and horizontal component 2 (c). Coherence was averaged for all broadband LBS over the 8-month deployment. Data has been high-passed filtered with a corner at 0.005 Hz. Obvious influence from infragravity waves is apparent in the high coherence between the vertical and pressure gauge between 0.01-0.08 Hz. Refer to Fig. 2.5 for the color-scale used to identify individual LBS.

2.4.1 Noise Characteristics and Compliance Corrections

Similar to ocean-bottom deployments, the LBS data suffer from higher noise levels than their onshore counterparts (Fig. 2.5) primarily due to the presence of additional noise sources like infragravity water waves, bottom currents, and out-of-level sensors (e.g., *Webb*, 1998). Figure 2.5 shows a comparison of noise levels between the lake-bottom instruments used in this study (in 200 - 600 m of water, see Table 2.1), two shielded OBS in comparable water depths (∼350 m) off the coast of Washington, USA (*Toomey et al.*, 2014), and one of our nearby SEGMeNT onshore stations (SCH). Similar to the OBS, noise on the LBS on the vertical component at long period (T >20 s) is much higher than the nearby land station. Noise levels remain higher through the microseism peak, but then are much lower than the land station at short periods, where cultural noise dominates the onshore recordings. Noise

levels for the LBS are lower than the comparable components of the OBS at nearly all periods, despite the fact that the LBS are not shielded. OBS studies have shown that on the vertical-component ground motion, long period (T >20 s) noise often can be significantly reduced using observations of infragravity waves on the accompanying pressure gauge, and tilt inferred from the horizontals (*Crawford and Webb*, 2000). These corrections are especially useful for deployments in shallow water where the strength of noise sources greatly increases (e.g., *Webb*, 1998; *Webb and Crawford*, 1999).

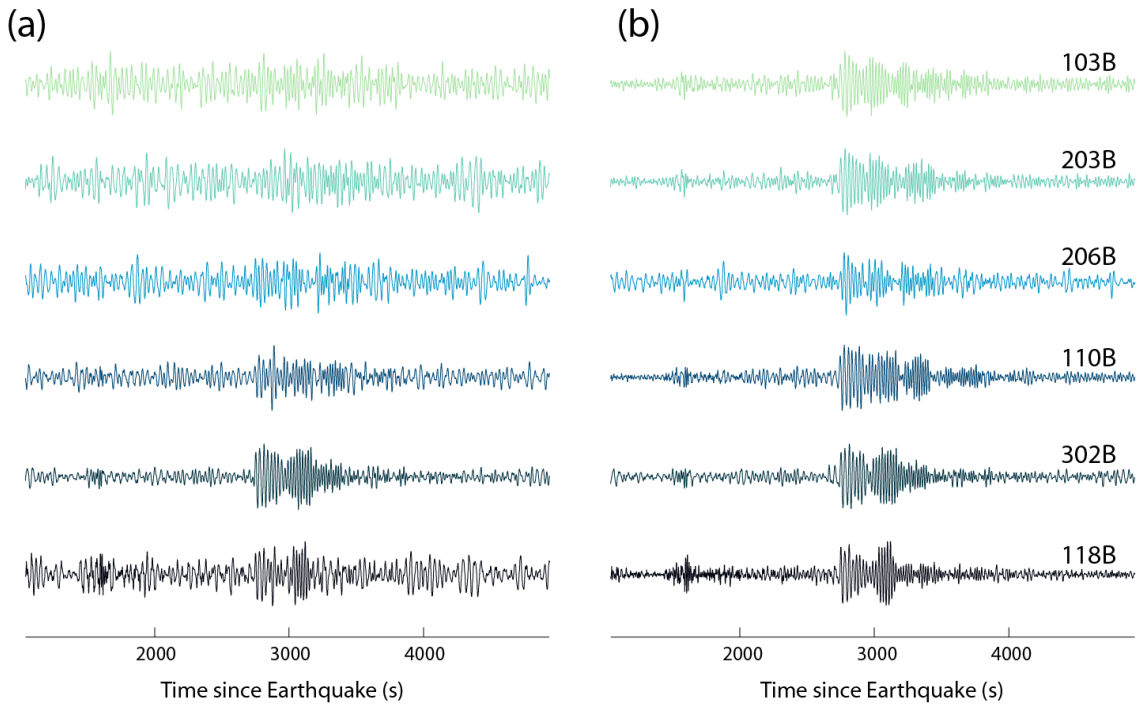

Figure 2.7: Comparison between original (left) and corrected (right) seismic traces recorded on LBS for the Mw 6.4 event on July 3, 2015 in Yilkiqi, China (epicentral distance 93.5°). The colors of the traces represent the individual instruments in both the left and right panels. Refer to Fig. 2.5 for the color-scale used to identify individual LBS.

To identify noise sources, we calculated coherence between the pressure gauge, vertical, and horizontal components (Fig. 2.6). This revealed high coherence between the vertical component and pressure gauge at periods between 20 - 80 s related to pressure gradients in the water column from long-wavelength infragravity waves. Little coherence was observed between the vertical and horizontal components suggesting that noise from bottom currents

and/or poorly-leveled sensors were not significant.

To remove the influence of noise resulting from infragravity waves, termed seafloor compliance, we followed the procedures of *Webb and Crawford* (1999). For each teleseismic event recorded on the LBS, we calculated the transfer function between the pressure gauge and vertical component for each instrument using 24-hours of continuous data from 1 or 2 days prior to the event of interest. To ensure that the continuous data from which the transfer

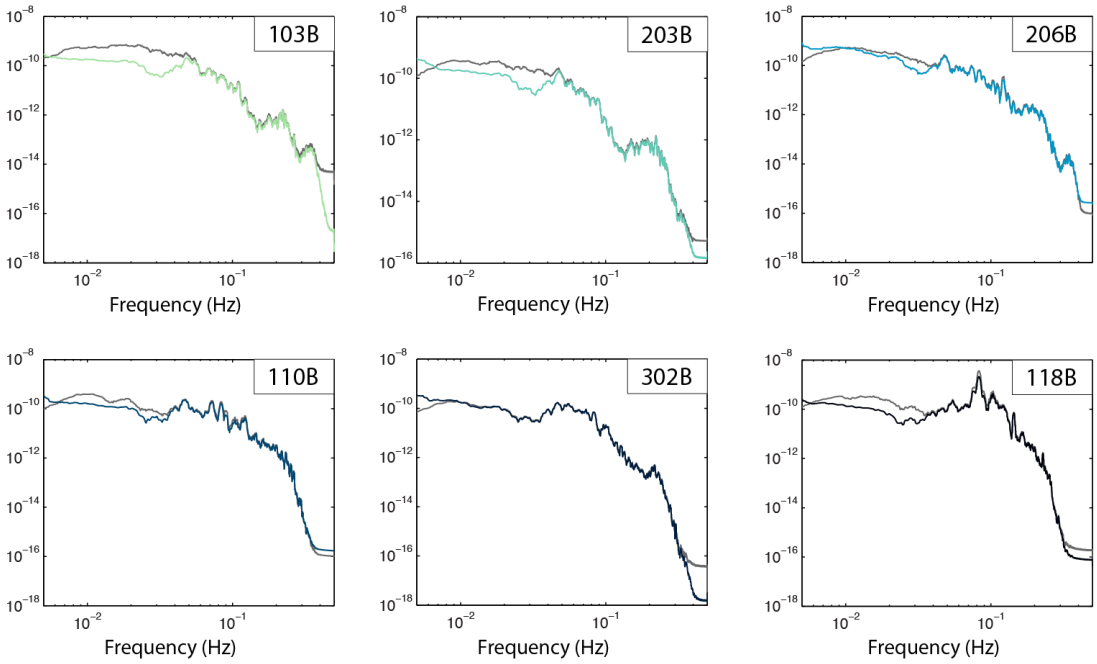

Figure 2.8: Comparison between the original (black) and corrected (colored) power spectra for the earthquake shown in Fig. 2.7. Noticeable reduction in noise is observed between ∼20 and 100 s.

functions were used did not include spurious noise or earthquakes, we cut the continuous data into 2-hour long windows and estimate the average power spectra. We discard any windows that lie outside the standard deviation of the mean, and we throw out the entire day of data if less than 10 windows are available. When the entire day of data is bad, we utilize the data from two-days prior to the event. Transfer functions between the pressure and vertical components were calculated after stacking the resulting high-quality windows. The vertical component for each event is then corrected by subtracting the product of the transfer function and the observed seafloor pressure for the event. Figures 2.7 and 2.8 show

the marked reduction in noise in both the frequency and time domain after applying these corrections. The noise from infragravity waves was not significant in the ambient noise band, so these traces do not require any correction.

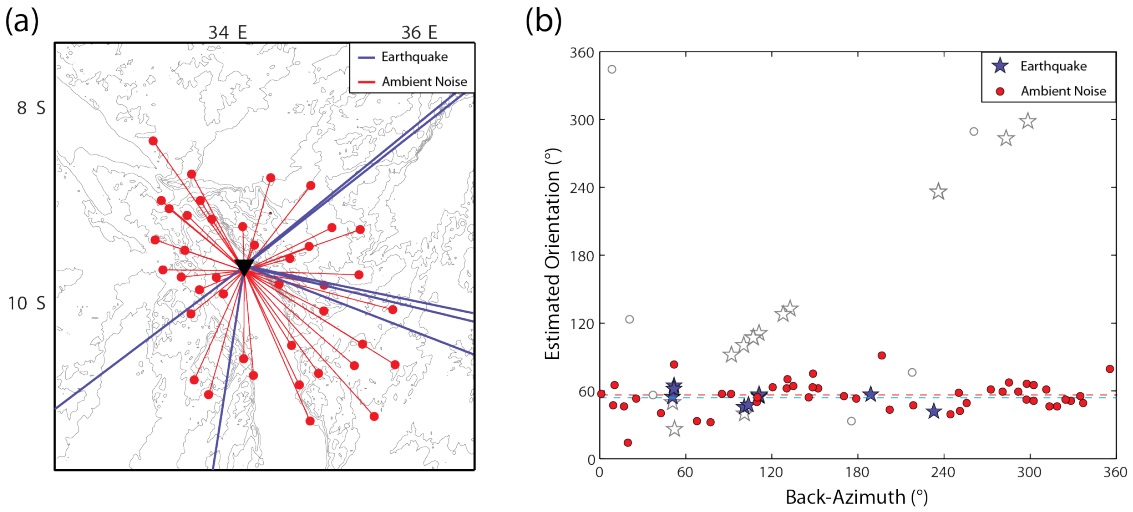

Figure 2.9: (a) Ray coverage map shown for orienting LBS 103B (location shown by black triangle). Red lines: interstation paths used in the ambient noise orientation method; blue lines: event-station great circle paths used in the earthquake orientation method. Topographic contours from NASA SRTM 30 m (*Farr et al.*, 2007) are shown in grey. (b) Comparison of determined station orientation for 103B across back-azimuth from ambient noise station pairs (red circles) and earthquakes (blue stars). Open symbols represent poor quality measurements thrown out by both methods. The final determined orientations from these two methods are shown by the red and blue dashed lines, respectively.

2.4.2 Determination of LBS Orientations

We successfully determined the orientations for 5 out of the 6 LBS (instrument 110B recorded only one independent horizontal component, making orientation impossible to determine). To ensure robust orientation estimates, we employed both the earthquake orientation method of *Stachnik et al.* (2012) (hereafter termed Method 1) and the ambient noise orientation method of (*Zha et al.*, 2013) (hereafter termed Method 2). Fig. 2.9 shows a comparison of the results from these two methods for instrument 103B. Both approaches rely on the same general principle of determining the orientation of the instrument by finding the rotation angle of the horizontal components that maximizes the coherence between the Rayleigh waves observed on the vertical component and the 90 phase shifted Rayleigh

Table 2.2: Final determined orientations for all LBS in the SEGMeNT experiment. Estimated orientations of horizontal component 1 (HH1) and their respective errors are shown for both the ambient-noise and earthquake orientation methods. We also present the determined orientation for the 3 misoriented onshore stations (MAND, MUDI, SCH). For these stations the estimated orientation represents the orientation of the N component relative to true North.

Instrument	**Est. Orientation from Earthquakes (°)**	**Standard Deviation (°)**	**Est. Orientation from Ambient Noise (°)**	**Standard Deviation (°)**
103B	54	5.5	54	9.9
110B	NA	NA	NA	NA
118B	28	3.6	29	19
203B	6	9.4	3	11.4
206B	56	6.4	55	13.6
302B	29	4.3	27	14.5
MAND	172	7.3	NA	NA
MUDI	175	9.9	NA	NA
SCH	175	9.3	NA	NA

waves on the rotated horizontal component. Table 2.2 gives a comparison of the results for all LBS from both methods. The two methods resulted in extremely consistent estimates of orientation with a mean difference of 1 and a maximum difference of 3.5°.

For Method 1 we used all events in our original catalogue with Mw >6.5 which resulted in 30 total events. However, given the high-noise level on the horizontal components individual stations averaged only 7-10 high quality events when determining the estimated orientation. Because of the small number of events used, gaps in azimuthal coverage were commonplace, motivating the use of Method 2 as an additional constraint. As a quality control check, we also employed Method 1 to confirm the orientations of stations in the onshore array and identified 3 misoriented sensors, demonstrating that orientation determination is a useful quality control measure for any onshore or offshore array.

Method 2 resembles that of Method 1 except that ambient-noise derived Rayleigh waves are substituted for their teleseismically-derived counterparts. For a given station, daily CCFs are calculated in the time domain between the vertical and two horizontal components of the LBS of interest and the vertical components of all surrounding onshore stations (Fig.

2.9a). Given the large number of nearby high-quality onshore stations, we did not calculate CCFs for LBS-to-LBS station pairs. Our ability to depend on onshore-to-offshore station pairs is unique to this experiment as standard OBS deployments must rely solely on offshore-to-offshore station pairs when using this orientation method. The large number of available station pairs led to excellent azimuthal coverage (Fig. 2.9b).

2.5 Results and Discussion

Figure 2.10 shows our preferred structural phase-velocity maps at periods of 9, 12, 18.5, 25, 40, and 60 s. Using a ray-theoretical approximation, we estimate that these maps satisfy approximately 80% of the variance observed in the ambient-noise phase velocities, and 60% of the variance in the individual ASWMS phase delays, compared to a regional 1-D starting model from the nearby Rukwa rift (*Kim et al.*, 2010). To guide our interpretation, we estimated fundamental-mode shear-velocity sensitivity using the normal mode summation code Mineos (*Masters et al.*, 2014) for the periods of interest. The kernels are based on the Rukwa Rift model from *Kim et al.* (2010) with an adjusted crustal thickness of 34 km. This thickness is chosen to represent the thinner rift-central crustal thickness determined from SEGMeNT receiver functions by *Borrego et al.* (2015), which average 38 $\pm$ 4 km. We find that all period bands are sensitive to the presence of a sedimentary layer at the top of the crust. Ambient-noise observations have high sensitivity down to $\sim$35 km depth and teleseismic observations down to >150 km (Fig. 2.11). We tested the influence of a water layer on the sensitivity kernels and find that its presence slightly reduces overall sensitivities in the sediments and upper crust but does not change the overall distribution of sensitivity.

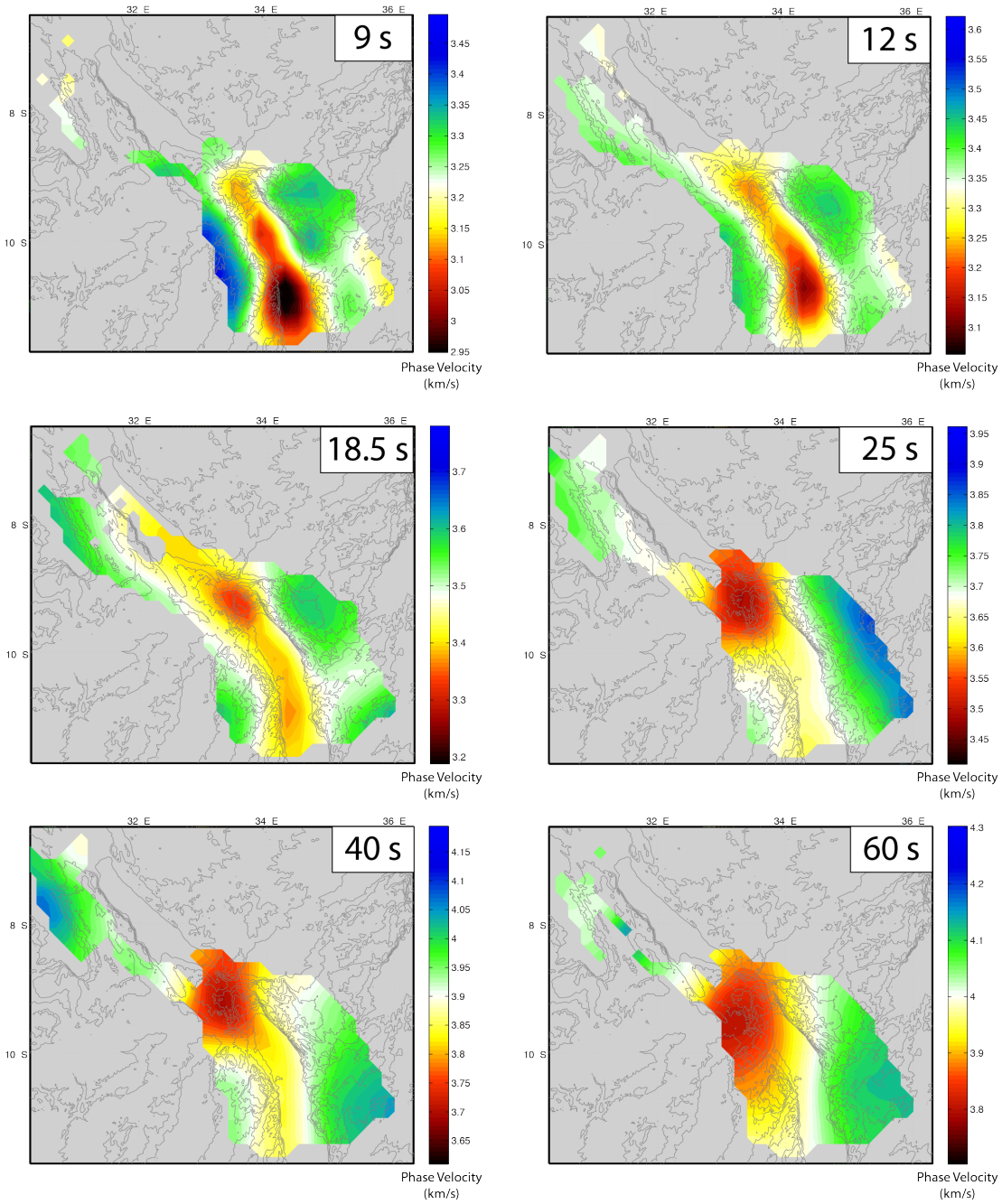

Figure 2.10: Maps of phase velocity for ambient noise (9, 12, and 18.5 s) and teleseismic (25, 40, and 60 s) Rayleigh waves. The period of the phase velocity measurement is labeled in the top right corner of each map.

2.5.1 The North and Central Basins of Lake Malawi: Localization of sedimentation and extensional processes

At short periods, the strongest feature in our phase velocity maps is the low-velocity

area that follows the trend of the basins of Lake Malawi, oriented roughly N-S within the Central Basin and then rotating to NW-SE in the North Basin (Fig. 2.10). These low velocities are apparent at long periods (up to 40 s) but are strongest at periods <20 s, where Rayleigh-wave sensitivity is wholly within the sediments and crust. At the shortest periods, low velocities are seen in both the North and Central basins of Lake Malawi, but are 2-3% slower in the Central Basin. We relate the low velocities at periods <20 s to the presence of a thick sedimentary package within Lake Malawi resulting from growth of border faults and related rift-floor subsidence, consistent with results of legacy and new reflection images, and possibly from the presence of older pre-rift strata.

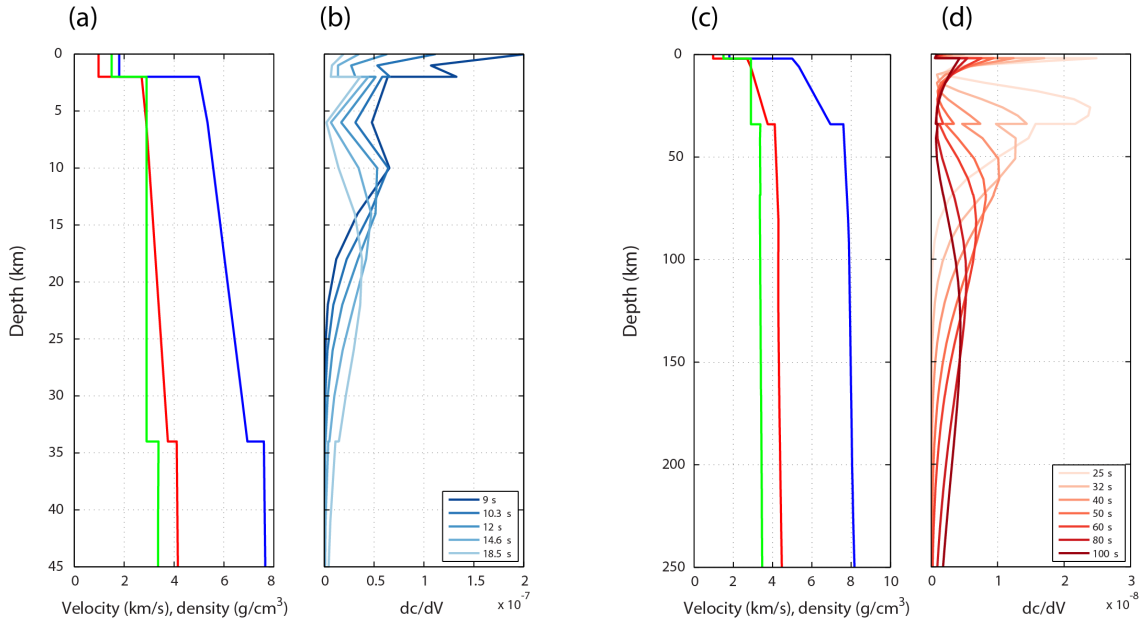

Figure 2.11: Comparison of phase-velocity sensitivity kernels for the Earth model based off of the study by *Kim et al.* (2010). (a) and (c) show P-wave velocity in blue, density in green, and S-wave velocity in red. (b) Sensitivity for the ambient noise period band down to a depth of 45 km. (d) Sensitivity for the teleseismic period band down to a depth of 250 km. Note that the x-axes changes scale between (a),(b) and (c),(d). Sensitivity kernels were calculated using the normal mode program Mineos (*Masters et al.*, 2014)

Extension along border faults in strong lithosphere here results in flank uplift paired with deep, narrow, asymmetric rift basins (e.g., *Ebinger et al.*, 1991; *Morley*, 1988). *Ebinger et al.* (1993b) simulated the basin and flank morphology and free-air gravity anomaly pat-

terns across the North Basin with 4-6 km of low-density sedimentary strata. Additionally, predictive models of airborne gravity and magnetic data in the onshore region of the North Basin indicate sediments are 4-4.5 km thick (*Macgregor*, 2015).

Fewer estimates of sedimentary thickness exist for the Central Basin compared to the North Basin (*Scholz*, 1989). However, given that the Central Basin exhibits the greatest water depths within Lake Malawi and is the terminus for two major rivers, the S. Rukuru and Ruhuhu, the Neogene-recent sediment package here is likely to be as thick or thicker than that in the North Basin. If the 3% reduction in velocity in the Central Basin relative to the North Basin is due to syn-rift sediment, then this would require an increase in the thickness of basin sediments, and thus could imply an increase in total extension, from north to south. Alternatively, the Central Basin is also thought to contain several kilometers of Karoo super-group sediments (*Ebinger et al.*, 1987; *Mortimer et al.*, 2016b), which are exposed onshore in the Ruhuhu basin (*Kreuser et al.*, 1990) and could contribute significantly to the strong short-period velocity anomaly. Several lines of evidence point to the presence of Karoo sediments in the Central Basin including a transition in the character of seismic reflectors between the North and Central basins (*Ebinger et al.*, 1987) and the location/orientation of horsts within the Central Basin which are thought to be controlled by pre-existing structures associated with Karoo rifting (*Mortimer et al.*, 2016b). Additionally, preliminary observations from the SEGMeNT active-source refraction study report a significant increase in the crossover distance between sedimentary and crustal refractions in the Central Basin (*Accardo et al.*, 2016), and preliminary P-wave velocity models contain a several-km-thick layer with P-wave velocities between 3-5 km/s, which may be consistent with older, more indurated Karoo sediments (*Shillington et al.*, 2015). We suggest that the low-velocity anomaly within the Central Basin represents an increased sediment package resulting from both greater sediment deposition related to Neogene-recent rifting (*Mortimer et al.*, 2016b) as well as the presence of several kilometers of Karoo-age sediment.

Further support for the contribution of Karoo sediments to the low velocities in the

Central Basin is provided by the observation of a low-velocity region extending from the eastern margin of the Central Basin onshore, where it directly underlies the Ruhuhu basin. This anomaly is subtler than those associated with the RVP and lake basins relative to the plateaus, but is a persistent feature at periods less than 25 s, and we interpret it as arising from Karoo sedimentary facies.

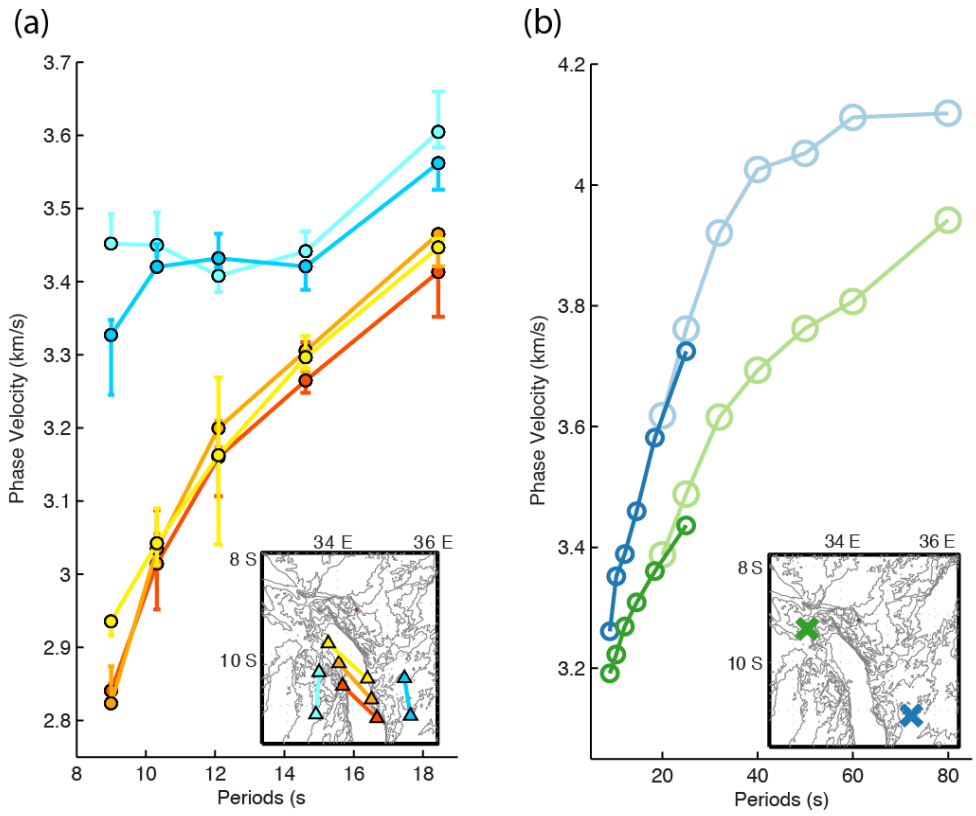

Figure 2.12: Comparison of individual ambient-noise station-pair dispersion curves (a) and inverted phase velocity curves from ambient-noise and teleseismic datasets (b). (a) Estimated dispersion curves determined from individual station pairs. Locations of station pairs are shown in the inset map with same color as the dispersion curves. Warmer colors represent station pairs associated with paths crossing the Central Basin of Lake Malawi while cooler colors represent station pairs associated with paths on the western and eastern plateaus. (b) Comparison of estimated phase velocities from teleseismic (lighter colors) and ambient noise (darker colors) at two locations.

Our phase velocity maps show that the low velocities beneath Lake Malawi extend to longer periods where the primary sensitivity is well below the depth of the sedimentary basin, in particular relative to the eastern margin of the rift, where high velocities persist at all frequencies (Fig. 2.12b). While these slow velocities likely are partly controlled by the

sedimentary structure, the fact that they roughly follow the trend of the primary rift basin but are broader than the short-period basin features suggests velocity reduction in the middle to lower crust. Fig. 2.12(a) compares dispersion curves estimated from station-pairs with paths crossing the Central Basin and paths wholly within the western and eastern plateaus. The difference in seismic velocities between the rift axis and the surrounding plateaus is $\sim$2 % at 18.5 s and decreases with increasing period until ultimately at 50 s, the anomaly is subsumed into the broad region of low velocities within the western half of the study region (Fig. 2.10).

A reduction in velocities beneath the rift at periods sensitive to the crust and uppermost mantle could be explained by localized fracturing and deformation associated with extension *Carlson and Gangi* (1985) or elevated temperatures. These observations are counter to what is observed in magmatic rifts, where lower crustal velocities are higher beneath the rift than outside it owing to extensive magmatic intrusion to the lower and middle crust (e.g., *Birt et al.*, 1997; *Hamblock et al.*, 2007) or significant crustal thinning, where slow crustal material is replaced by denser, faster velocity upper mantle material. A reduction in velocities at longer periods would be expected if lithospheric thinning has occurred such that higher velocity lithospheric mantle is replaced by slower, hotter asthenospheric mantle that may contain a small melt fraction. In detail this low velocity anomaly is shifted slightly westward from the true center of Lake Malawi, persisting farther west beneath the Nyika plateau as compared to the abrupt transition to fast velocities at the junction beneath the eastern boundary of the lake and the eastern plateau. The asymmetry in crustal velocities may relate to the presence of heterogeneous preexisting crustal terrains, asymmetric rifting processes, or some combination of the two. The competing effects of variations in crustal thickness and crustal and upper mantle velocity structure can be difficult to distinguish using phase velocity maps derived from surface waves, which are defined by integrative depth sensitivity. Future analyses that utilize independent constraints on basin and crustal architecture will clarify the nature of crustal and lithosphere extension.

2.5.2 The Rungwe Volcanic Province: The localization of magmatism at depth

One of the most striking features in the phase velocity maps in Fig. 2.10 is the prominent low velocity region imaged beneath the RVP. We find that the anomaly has the strongest amplitude within an intermediate period band (∼25-60 s) and becomes more diffuse and shifts westwards at longer periods. Phase velocities for this low-velocity region are ∼5% lower than the surrounding western and eastern plateaus at intermediate and long periods. At periods between 25-50 s the anomaly appears roughly circular, with the lowest velocities confined to a region with a radius of ∼70 km. The ray coverage provided by the TANGA stations allows clear imaging of the north/northwest edge of the feature, suggesting that it does not extend beyond the narrow Songwe basin into the Rukwa rift segment. The anomaly decreases in size and amplitude within the ambient-noise period band.

Our phase velocity images place the strongest anomaly at periods that suggest a lower-lithosphere or asthenospheric origin for the RVP low-velocity feature. The localization of this large-magnitude, low-velocity anomaly beneath the RVP matches lower-resolution observations of low-velocity regions associated with the RVP (*O'Donnell et al.*, 2016) and other volcanic provinces along the Western Branch (*Adams et al.*, 2012; *O'Donnell et al.*, 2013). Although Western-rift eruptive centers commonly coincide with intrabasinal accommodation zones, our new results and earlier models suggest that the localization of magma is caused by processes at depth (*Ruppel*, 1995; *Corti et al.*, 2002; *Corti*, 2004). The ca. 20 My time span of magmatism and regional elevation of magmatic provinces suggests they are temporally persistent, and could have played a role in strain localization. Localized melting may be expected to occur beneath the Rungwe region due to a variety of mechanisms including thermal or compositional anomalies in the upper mantle, thinning of the lithosphere from Neogene-recent rifting, pre-thinning of the lithosphere prior to present rifting, or a combination of the above.

Ebinger and Sleep (1998) model the flow of upwelling mantle plume beneath variable thickness lithosphere, and predict enhanced melting beneath the margins of the deeply

rooted Tanzania and Congo cratons. Regions of pre-existing weakness and/or thin lithosphere are proposed to control lateral transport of hot plume material and where it ponds and escapes to the surface as a volcanic center, as seen along the Western Branch (e.g., *Nyblade et al.*, 2000). Studies of shear-wave splitting further promote the idea of broad-scale along-axis mantle flow beneath the EARS *Bagley and Nyblade* (2013); *Tepp* (2016), although pre-existing lithospheric fabrics may also play a role (*Walker et al.*, 2004). Our observations of highly focused low velocities beneath the long-lived RVP and absence of similarly low velocities beneath the rift basins to the north and the south suggest that along-axis flow may not be as significant in this part of the EAR (Fig. 2.10). Decreased velocities are present beneath the axis of the Malawi Rift at the same periods where the RVP anomaly appears strongest but these velocities are appreciably higher relative to the surrounding plateau than those observed beneath the RVP ($\sim$2.5 % and $\sim$5 %, respectively).

At the longest periods, the slow velocities associated with the RVP show a broadening and westward expansion at depth compared with the focusing of low velocities beneath Rungwe volcanoes at shorter periods (Figs 2.10, 2.12). A similar broadening and westward shift in the location of the RVP anomaly is observed in the Rayleigh-wave phase velocity maps of both *Adams et al.* (2012) and *O'Donnell et al.* (2013). The observation of low velocities at depth outside the rift valley and volcanic province is qualitatively similar to observations from the Main Ethiopian Rift (MER), where low velocities extend west beneath the Ethiopian Plateau at depths >75 km (*Bastow et al.*, 2008; *Gallacher et al.*, 2016). However, the absolute phase velocities are substantially lower (>5%) within the MER (*Gallacher et al.*, 2016) at all periods compared to those in the Malawi Rift. We suggest the westward broadening of the observed anomaly at lower-lithospheric depths may represent a broad region of lithospheric thinning associated with extension and/or a broad region of relatively warm asthenosphere underlying the rift and the western plateau.

2.6 Conclusions

This study presents the first locally constrained tomographic phase-velocity maps of the weakly extended Malawi Rift and surrounding region. We have successfully corrected six LBS for long-period infragravity waves and robustly determined their orientations. This effort represents some of the first observations of seismometer derived noise levels in a freshwater rather than oceanic environment. Our resulting phase velocity maps present two views of the rift system. At the shortest periods and hence shallowest depths, low velocities are bounded to the North and Central basins as a result of thick sedimentary packages. Low velocities beneath the lake basins extend to 40 s where sensitivities are within the lower crust and potentially uppermost lithospheric mantle suggesting a localization of extensional processes. At the longest periods our phase-velocity images reveal a ubiquitous low-velocity region associated with the RVP and the co-located accommodation zone. Our data provide excellent ray coverage such that we can constrain the RVP anomaly and show that similar-magnitude low-velocity regions do not extend north into the Rukwa Rift or south along the Malawi Rift. Estimates of phase-velocity sensitivity place these low velocities within the lithospheric mantle and potentially uppermost asthenosphere, suggesting that mantle processes may control the association of volcanic centers and the localization of magmatism.

Acknowledgements

The authors gratefully acknowledge all of those involved in the acquisition of the SEGMeNT and TANGA datasets, including technicians and engineers from PASSCAL program of the Incorporated Research Institutions in Seismology (IRIS) and the OBS program at Scripps Institution of Oceanography, and the crews of the *F/V* Ndunduma and *M/V* Chilembwe. We thank the communities in our study area and national and regional governmental entities for their support, without which our project would not have been possible. Seismic instrumentation was obtained from IRIS-PASSCAL, and the Ocean Bottom Seismology Instrumentation Program (OBSIP). Data is archived at the IRIS Data Management Center,

and was downloaded using the Standing Order for Data (SOD) software package out of the University of South Carolina. We thank Ge Jin, Yang Zha, PeiYing Lin, and Helen Janiszewski for sharing computer programs used in this study and Cornelia Class and Gary Mesko for useful discussions. This research was supported by NSF grant EAR-1110921, the NSF Graduate Research Fellowship Program, NERC grant NE/K500926/1, and NERC grant NE/L013932/1. Seismic equipment from SEIS-UK is funded by NERC under agreement R8/H10/64 and funding was provided by Beach Petroleum.

3 The Growth and Interaction of Large Border Faults in the Malawi Rift revealed by 3D Seismic Refraction Imaging

Co-authors: D. J. Shillington, J. B. Gaherty, C. A. Scholz, C. J. Ebinger, A. A. Nyblade, P. R. N. Chindandali, G. Kamihanda, T. McCartney, D. Wood, R. Wambura Ferdinand

A slightly modified version of this chapter has been submitted to the *Journal of Geophysical Research* and is presently under review.

Abstract: We present new constraints on rift basin structure in the weakly extended northern Malawi Rift from a 3-D compressional velocity (Vp) model to investigate border-fault geometry, accommodation-zone structure, and the role of preexisting structures underpinning this rift system. The velocity model uses observations from the first wide-angle refraction study conducted using lake-bottom seismometers in one of the great lakes of East Africa. The northern Malawi Rift is flanked by basin-bounding border faults and crosses several significant remnant structures, making it an ideal location to investigate the development of normal faults and their associated basins. The 3-D velocity model reveals up to ∼5 km of synrift sediments, which smoothly transition from eastward thickening against the Livingstone Border Fault in the North Basin to westward thickening against the Usisya Border Fault in the Central Basin. Greater than 4 km of sediment are imaged within the accommodation zone pointing to the early development of the boder faults. We use new

constraints on synrift sediment thickness to construct displacement profiles for both faults. Both faults accommodate large throws (>7 km) but the Livingstone Fault is ∼30 km longer. The dimensions of these faults place them near their maximum size predicted from models of fault growth. The presence of an intermediate velocity unit with velocities of 3.75-4.5 km/s is interpreted to represent prior rifting (Permo-Triassic and/or Cretaceous) sedimentary deposits beneath Lake Malawi. These thick (up to 4.6 km) packages of preexisting sedimentary strata improve our understanding of the Tanganyika-Rukwa-Malawi rift system and the role of earlier stretching phases on synrift basin development.

3.1 Introduction

A long-standing debate surrounds the development and abandonment of basin-bounding border faults like those characteristic of the Western Rift of the East African Rift System (EARS). Border faults along the Western Rift formed within cold, strong lithosphere and have achieved fault lengths of over 100 km, making them some of the largest normal faults in the world (*Ebinger et al.*, 1999). Normal-fault populations appear to exhibit characteristic relationships between fault length, fault displacement, seismogenic-layer thickness, and surface processes (e.g., *Cowie and Scholz*, 1992; *Dawers and Anders*, 1995; *Olive et al.*, 2014; *Buck*, 1993), which have direct implications for the initiation and evolution of rift systems as well as present-day seismic hazards. Competing models for fault growth predict different relationships between these parameters, whereby the isolated-fault model (e.g., *Dawers et al.*, 1993; *Dawers and Anders*, 1995; *Cartwright et al.*, 1995) suggests that displacement should scale linearly with length, and the constant-length model (*Morley*, 2002; *Walsh et al.*, 2002; *Nicol et al.*, 2005; *Curry et al.*, 2016) suggests that fault length is established early, such that the ratio of displacement to length can vary (for a review see *Jackson et al.*, 2017). Although several studies evaluate border and intrabasinal fault dimensions along the Western Rift (e.g., *Jackson and Blenkinsop*, 1993a, 1997; *Morley et al.*, 1992), our understanding of these fault systems and their implications for controls on fault development have been

hampered by limited constraints on total fault throw.

Models for normal fault behavior have direct implications for the evolution of rift basins and the lifespan of these large border faults. Significant extensional strain is accommodated within the brittle crust as offset along basin-bounding border faults. Border fault dimensions are primarily controlled by the elastic thickness, or integrated strength envelope, of the continental lithosphere (e.g., *Hayward and Ebinger*, 1996; *Jackson and Blenkinsop*, 1997). As rifting progresses, strain is observed to migrate inwards onto intrabasinal structures as has been shown in many locations including in Greece (*Goldsworthy and Jackson*, 2001) and the Main Ethiopian Rift (*Ebinger and Casey*, 2001). Modeling studies have proposed different theoretical limitations on border fault offset before faults become mechanically unfavorable and may be abandoned in favor of new faults (e.g., *Scholz and Contreras*, 1998; *Olive et al.*, 2014), yet few data points exist to test these models at the scale of the faults studied here.

Extensive debate also surrounds the role of inherited structures in the rifting process. At the largest scale, East African rift systems and volcanic provinces develop in thinner, and mechanically weaker, Proterozoic orogenic belts that circumvent the Tanzanian craton (e.g., *McConnell*, 1972; *Mulibo and Nyblade*, 2013; *Koptev et al.*, 2015), similar to the development of other rifts (Baikal Rift) (e.g., *Delvaux et al.*, 1995). At the basin scale, studies suggest that preexisting structures may influence border fault growth and segmentation (e.g., *Versfelt and Rosendahl*, 1989; *Morley*, 2010; *Fagereng*, 2013). The segmented border fault zones of the Western Rift are linked by relay ramps and transfer faults in accommodation zones where border faults commonly have opposing senses of asymmetry. The geometry of relay ramps and transfer faults may be influenced by preexisting structure, particularly where older sedimentary basins bounded by steep faults intersect the Miocene-Recent rift structures, as in the central Malawi rift (*Versfelt and Rosendahl*, 1989; *McCartney and Scholz*, 2016). The structural grain of basement fabrics has also been hypothesized to influence the growth of the largest border faults along the Western Rift (e.g., *Ring*, 1994; *Ebinger et al.*, 1999; *Kinabo et al.*, 2008; *Morley*, 2010; *Fagereng*, 2013), whereby these faults may establish their

great lengths by taking advantage of optimally oriented inherited shear zones and structural foliations. However, complexities exist as faults within the Western Rift are also seen to cross-cut basement fabrics and inherited structures (e.g., *Ebinger et al.*, 1999). Evaluating the control of preexisting structures is crucial to deciphering how extension is accommodated on the scale of individual faults, rift basins, and entire rift systems. Masking these controls are present-day rift processes like breaking of new faults, flank uplift and erosion, basin formation, and the emplacement of melt products. This paper presents results from the first seismic refraction survey using lake-bottom seismometers undertaken in an East African rift lake. We conduct 3-D first-arrival time tomography to constrain basin structure within the weakly extended Malawi Rift. Our investigation provides new insight into border-fault geometry, accommodation-zone structure, and the role of preexisting structures underpinning this rift system.

3.2 Geologic Background

3.2.1 The East African Rift System

The EARS extends over 3,000 km from the Main Ethiopian Rift and Afar Depression in the north to a series of rift basins in Mozambique in the south, and to Botswana in the southwest (e.g., *Chorowicz*, 2005; *Ebinger and Scholz*, 2012). Studies of GPS data indicate relatively slow opening rates of ∼1-6 mm yr^{-1} along the EARS (*Saria et al.*, 2014; *Stamps et al.*, 2014). The EARS developed within old, cold, thick lithosphere characterized by large values of effective elastic thickness (T_e) and lithospheric strength (e.g., *Ebinger et al.*, 1999; *Pérez-Gussinyé et al.*, 2009; *Stamps et al.*, 2014). The EARS bifurcates around the Archean Tanzanian Craton into the Western and Eastern Rifts, with both rifts developing within Proterozoic orogenic belts (for a review see *Fritz et al.*, 2013). The alignment of rift basins and Proterozoic mobile belts suggests the large-scale control of preexisting lithospheric structures on rift evolution (e.g., *Nyblade and Brazier*, 2002; *Corti et al.*, 2007). At smaller scales, the relationship between rifting and preexisting lithospheric heterogeneities can be

more complex. The EARS developed within terranes that host major shear zones and remnant extensional/orogenic structures with variable orientations with respect to present day extension (e.g., *Catuneanu et al.*, 2005; *Fritz et al.*, 2013), and debate continues concerning how these structures may influence basin development and fault growth (e.g., *Daly et al.*, 1989; *Smith and Mosley*, 1993; *Kinabo et al.*, 2008; *Ebinger et al.*, 1997; *Fagereng*, 2013).

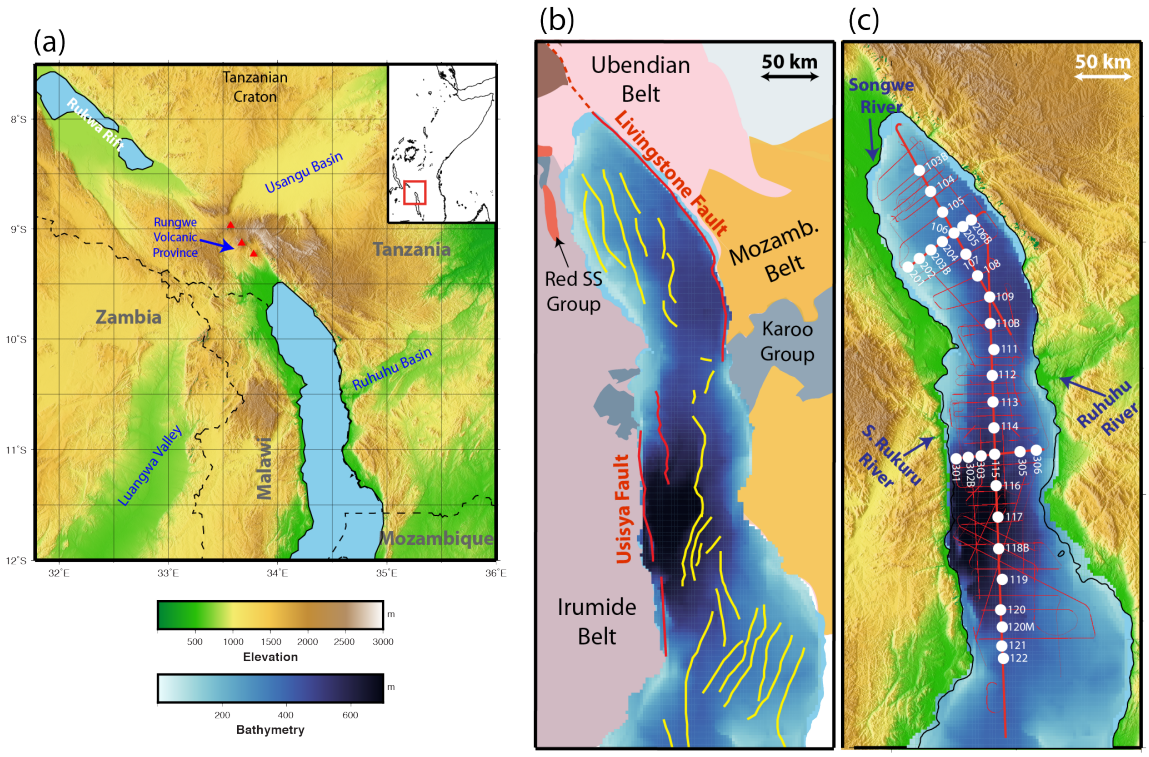

Figure 3.1: (a) Overview figure of the study region with locations of interest labeled. Red triangles indicate Quaternary-Recent volcanoes. The location of the study area is shown within East Africa in the inset. (b) Simplified onshore geology of the northern Malawi Rift. The Irumide, Ubendian, and Mozambique Proterozoic mobile belts are shown as well as Karoo Group (Carboniferous-Permian) and Cretaceous Red Sandstone Group sediments. Geologic units were mapped following *Bennett* (1989), *Delvaux* (2001), *Pinna et al.* (2004), *Roberts et al.* (2010), and *Fritz et al.* (2013). Intrabasin faults (yellow) and the border faults (red) are shown from *Mortimer et al.* (2007), *Lyons et al.* (2011), and *McCartney and Scholz* (2016). (c) Map detailing the SEGMeNT active-source experiment. Red lines indicate the lines were reflection/refraction data were acquired. LBS locations are shown by the white circles and instrument names are labeled. Blue arrows indicate where rivers enter Lake Malawi. Bathymetry of Lake Malawi is shown in both (b) and (c).

The Western Rift is characterized by a series of >100-km-long, asymmetric basins flanked by broad uplifts, occasionally with alternating polarity (e.g., *Rosendahl et al.*, 1992). Esti-

mates of crustal stretching from balanced cross-sections of rift profiles, forward models of basin and flank morphology, and seismic imaging indicate $\sim$ 20% crustal thinning, or about 10 km of opening in sectors of the Western Rift (*Morley*, 1988; *Ebinger et al.*, 1991; *Wölbern et al.*, 2010). These weakly extended rift basins are commonly filled by narrow and deep freshwater lakes (e.g., *Soreghan et al.*, 1999). While magmatism is widespread in rift sectors east of the Tanzania craton, the Western Rift is relatively magma-poor, with volcanism limited to isolated, volumetrically small volcanic centers (*Furman*, 2007).

Few data points exist to date the onset of rifting in the deep Western rift lakes. Dated volcanic rocks and extrapolations of present-day sedimentation rates suggest rifting initiated by $\sim$12 Ma (for a review see *Ebinger and Scholz*, 2012). However, dating of airfall deposits in the Rukwa Rift (Fig. 3.1a) suggest that magmatism started as early as 26 Ma (*Roberts et al.*, 2012), which could indicate that extension in the Western Rift may have evolved concomitantly with other parts of the EARS.

3.2.2 Lake Malawi and the Malawi Rift

The Malawi Rift in the southern EARS is a seismically active, magma-poor, weakly extended continental rift. Lake Malawi (Nyasa) extends for $\sim$550 km along the axis of the Malawi Rift, straddling the borders of Malawi, Tanzania, and Mozambique. Like other African rift lakes, Lake Malawi is narrow (25 - 80 km wide) and deep (maximum water depth is $\sim$ 700 m) (Fig. 3.1). Border-fault-bounded half grabens partition Lake Malawi into three basins (North, Central, and South) linked via accommodation zones whose geometries were poorly constrained by earlier seismic reflection surveys (e.g., *Scholz*, 1989).

These basins developed within Proterozoic orogenic belts: the eastern boundary of Lake Malawi abuts the contact between the Irumide Belt to the west, and the Mozambique and Ubendian/Usagaran belts to the north and east, respectively (e.g., *Fritz et al.*, 2013; *Hanson*, 2003)(Fig. 3.1b). The Malawi Rift is crosscut by two large-scale Permo-Triassic (Karoo) basins: the Ruhuhu Basin, which intersects the rift at the accommodation zone between the North and Central basins (*Ebinger et al.*, 1987; *Versfelt and Rosendahl*, 1989) (Fig. 3.1a),

and the Maniamba Trough, which intersects the rift to the east between the Central and Southern basins (*Catuneanu et al.*, 2005). The northern end of the rift hosts the Rungwe Volcanic Province (RVP), a localized center of alkaline volcanism that initiated by ca. 17 Ma (*Rasskazov et al.*, 2003; *Mesko et al.*, 2014) and remains active today (*Ebinger et al.*, 1989, 1993b; *Fontijn et al.*, 2010a). Karoo-age and Cretaceous Red Sandstone sediments associated with prior rifting episodes outcrop along the western edge of the RVP continuing towards the Rukwa Rift (e.g., *Jacobs et al.*, 1990; *Roberts et al.*, 2010). Modern extension rates constrained by sparse GPS data and rigid plate models suggest a plate-opening velocity of ca. 2 mm/yr (*Saria et al.*, 2014).

3.2.3 The North and Central Basins of Lake Malawi

For this study, we focus on the North and Central basins of Lake Malawi. The North Basin represents a type example of a half-graben structure, with seismic reflection images revealing sediments thickening eastwards towards the west-dipping border fault (Livingstone Fault) (e.g., *Scholz*, 1989; *Mortimer et al.*, 2007). The Livingstone Fault extends for more than 120 km along the eastern lakeshore of the North Basin (*Wheeler and Karson*, 1989), with the fault trace terminating in the south near the Ruhuhu Basin. A significant portion (∼30 km) of the Livingstone Fault continues onshore, north of Lake Malawi (*Ebinger et al.*, 1993b; *Wheeler and Rosendahl*, 1994)(Fig. 3.1a). The strike of the Livingstone Fault, NNW-SSE, is oblique with respect to the inferred direction of extension (E-W) compared to the other two basins of Lake Malawi. In detail, the trace of the Livingstone Fault contains two small (<5 km) steps that divide it into three ∼30- to 40-km-long segments (*Mortimer et al.*, 2007). The hanging wall is cut by synthetic intrabasinal faults both beneath the lake and onshore to the north (i.e., Mbaka Fault), some with significant offset (*Specht and Rosendahl*, 1989; *Wheeler and Rosendahl*, 1994; *Mortimer et al.*, 2007; *Ebinger et al.*, 1993b).

Despite previous studies, much uncertainty remains concerning the amount and distribution of sediment within the North Basin. Previous seismic reflection imaging (hereafter termed legacy) included Project PROBE, which collected data over the entire lake in the

1980's (e.g., *Scholz*, 1989), and high-resolution single channel programs focused on delta structures in both basins in 1992 and 1995 (*Scholz*, 1995a). While these data provided important constraints on shallow sedimentary structure and faulting, depth penetration was limited by small source volumes and did not clearly identify basement reflections (e.g., *Flannery and Rosendahl*, 1990; *Mortimer et al.*, 2007). Models of gravity data constrained by seismic reflection data estimate 4-5 km of sediment in the North Basin (*Ebinger et al.*, 1991, 1993b).

The Central Basin is bound on the west by the ∼140-km-long Usisya border fault, an east dipping array of faults (Fig. 3.1b). The uplifted footwall exposes Mesoproterozoic Irumide Belt (*Fritz et al.*, 2009) (Fig. 3.1b). The Usisya border fault comprises three fault segments, each 40-60 km long, which are offset by ∼10 km with respect to each other (e.g., *Ebinger et al.*, 1987; *Scholz*, 1989; *Soreghan et al.*, 1999; *Contreras et al.*, 2000). These offsets are more significant than the steps that separate the segments of the Livingstone Fault. Prior studies have identified a significant relay-ramp structure that connects the north and central segments (e.g., *Scholz*, 1989; *Ebinger et al.*, 1987), but available data does not identify a similar structure between the central and southern segments. Like the North Basin, the Central Basin represents a single half-graben basin but exhibits more complex intrabasinal faulting. Previous reflection seismic studies have imaged the structurally complex, north-northwest dipping Lipichilli Fault Zone that extends for ∼28 km across the southern edge of the basin (*Scholz*, 1989; *McCartney and Scholz*, 2016). Previous studies using PROBE seismic data could not confidently identify crystalline basement in many areas. Where it could be identified, estimates of sediment thickness rely on assumed relationships between two-way-travel time (TWTT) and depth (e.g., *Contreras et al.*, 2000; *Wheeler and Karson*, 1989). The deepest bathymetry within the Central Basin is found within a region bounded to the west by the central segment of the Usisya border fault and the east by an intrabasinal high (Fig. 3.1b). Some studies suggest that a second border fault bounds the eastern side of the southern Central Basin, termed the Mbamba Fault (e.g., *Flannery and Rosendahl*,

1990; *Lao-Davila et al.*, 2015; *Mortimer et al.*, 2016b). However, *McCartney and Scholz* (2016) suggest this feature is not a rift border fault based on the absence of clear patterns of eastward thickening sediment expected for hanging wall subsidence.

The character of the accommodation zone between the North and Central basins and how it transfers strain between the Livingstone and Usisya faults remains enigmatic (*Flannery and Rosendahl*, 1990). One PROBE seismic reflection line images a possible structural high embedded within an area of overall low relief (*Specht and Rosendahl*, 1989). The Ruhuhu Basin is a Late Carboniferous Karoo rift basin associated with early Gondwana breakup (e.g., *Catuneanu et al.*, 2005; *Wopfner*, 2002, 1994) and intersects the rift at the accommodation zone. The Ruhuhu Basin has been proposed to influence the location and structure of the accommodation zone (e.g., *Versfelt and Rosendahl*, 1989), but the specifics of that interaction are yet to be understood (*Flannery and Rosendahl*, 1990).

3.3 Data and Methods

3.3.1 SEGMeNT 3-D refraction experiment

An active-source seismic experiment was conducted in the North and Central basins of Lake Malawi in the spring of 2015 as a part of the multidisciplinary Study of Extension and maGmatism in Malawi and Tanzania (SEGMeNT) project (*Shillington et al.*, 2016). This experiment is the first of its kind to be conducted within one of the great rift lakes of East Africa. Thirty-two lake-bottom seismometers (LBS) were deployed in February 2015 by the F/V *Ndunduma*. The LBS array comprised 26 Scripps Institute of Oceanography (SIO) four-component (3-axis geophone and hydrophone) short-period instruments and six SIO four-component (3-axis seismometer and differential-pressure gauge) broadband instruments. The instruments recorded data at 100 Hz (broadband) and 200 Hz (short-period). The 26 short period instruments were recovered in April 2015 by the F/V *Ndunduma*, and the six broadband instruments were recovered in November 2015 by the M/V *Chilembwe*, and thus all instruments recorded the entire active-source seismic program. Instruments were

deployed in 200-650 m of water and along 3 main transects (see Fig. 3.1c) with a spacing of ∼7 to 15 km.

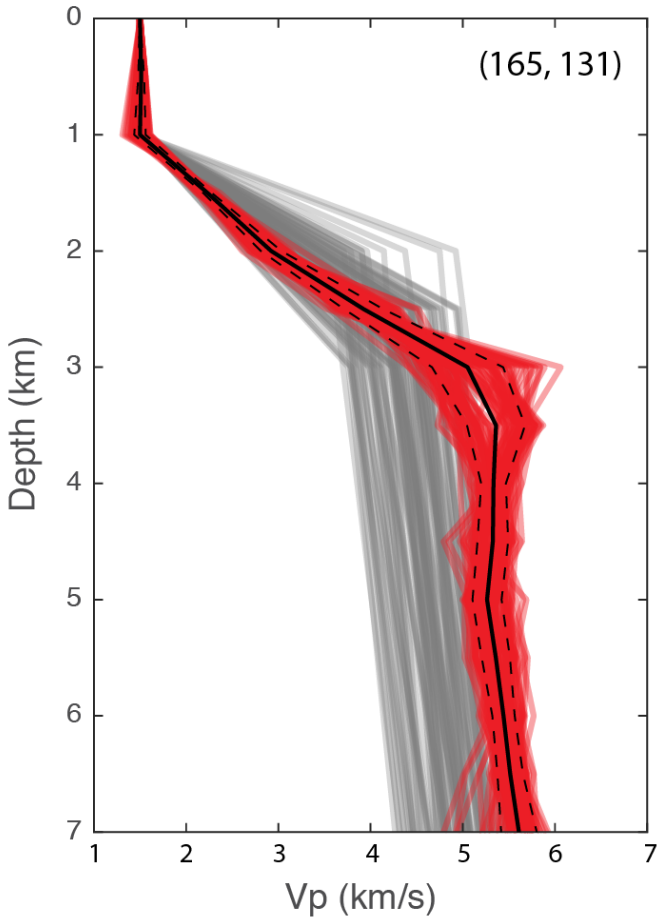

Figure 3.2: Comparison of all 1-D Vp profiles for a given location from the initial models (grey lines) and the final models (red lines). 105 total models are shown. The black solid line indicates the average of all final velocity models and the black dashed lines indicate one standard deviation around the mean velocity. The location where these profiles were taken is given in the top right hand corner of the figure in the local coordinate system used in this study (see Section 3.3.2 for information on the local coordinate system).

During a 29-day cruise aboard the M/V *Katundu* in March 2015, seismic reflection data were acquired, and seismic sources were generated for the wide-angle reflection/refraction study. The primary acoustic source for the refraction work consisted of six air guns from the Geological Survey of Greenland and Denmark and Aarhus University with a combined shot volume of 2580 inch^3 firing at a pressure of 180 bar. Shot spacing for the refraction

work was 250 m to mitigate previous shot noise. In total, we acquired >1,500 km of data at this large shot volume including the primary profile lines, additional refraction lines, turns between reflection lines, and during streamer and ship maintenance. The LBS also recorded ∼2,000 km of smaller volume reflection (CMP) shots consisting of 2-6 guns with combined shot volumes of 500-1580 inch^3 at pressures of ∼120 bar. Shot spacing during the reflection acquisition varied between 12-50 m. Whereas the larger volume shots were recorded on LBS to offsets >230 km, the smaller volume shots were generally limited to offsets of ∼ 25 km due to interference from previous shot noise.

3.3.2 Data processing and phase interpretation

Processing of LBS data was conducted using the Seismic Unix software package (http://www.cwp.mines.edu/cwpcodes/) and involved the following steps: 1) minimum-phase bandpass filter with corners at 2, 4, 15, and 20 Hz; 2) reduction velocity of 6 km/s; 3) trace balancing; 4) offset-variable gain to all traces. On five of the 32 LBS, we utilized the hydrophone channel rather than the vertical-component geophone due to significantly higher signal to noise ratio. Instruments were not relocated because water depths are relatively shallow (<700 m), and relocation tests on instruments did not yield significantly different positions. The times of direct arrivals on near-offset traces indicate that the instrument deployment positions were consistent with the data.

First arrivals were picked on all instruments to offsets of 50 km (Table 3.1); arrivals are visible to offsets >220 km but are not utilized in the present study. The uncertainty of the travel-time pick is assigned via visual inspection. Uncertainties range from 25 - 200 ms with a median uncertainty of ∼ 100 ms. The limited number of picks that were associated with the largest uncertainties were assigned to picks at far offsets on the reflection lines (∼25 m shot spacing) where previous shot noise was significant. We initially picked all available data, which led to picks at variable shot intervals from the reflection and refraction work. To ensure that picks from lines with shorter shot intervals did not dominate the inversion, we decimated our initial picks such that picks had a minimum spacing of 150 m along all

Table 3.1: Table of instrument names, locations, total number of picks, chi-squared, and RMS values associated with the final velocity model.

LBS	**Lon**	**Lat**	**Water Depth (m)**	**# Picks**	**Chi Squared**	**RMS (s)**
122	34.448	-11.648	458	765	0.6453	0.0717
121	34.441	-11.598	450	931	1.9746	0.1259
120M	34.443	-11.523	475	1058	0.7513	0.0814
120	34.437	-11.456	518	1576	0.6642	0.0911
119	34.444	-11.336	560	1615	0.9067	0.1134
118B	34.43	-11.214	605	2628	1.0306	0.1156
117	34.427	-11.089	683	911	0.8836	0.0682
116	34.419	-10.965	679	1600	0.7271	0.0758
301	34.259	-10.859	500	1598	1.7035	0.1372
302B	34.308	-10.853	512	2110	1.8653	0.1188
303	34.359	-10.847	584	2048	0.4889	0.0794
115	34.414	-10.841	563	2051	1.1493	0.0923
305	34.523	-10.829	490	849	0.8001	0.0995
306	34.579	-10.825	397	1120	3.6149	0.1903
114	34.41	-10.737	514	1718	0.6533	0.0869
113	34.407	-10.633	472	1892	0.5995	0.0716
112	34.403	-10.529	454	998	1.3684	0.1226
111	34.41	-10.426	458	1332	1.1896	0.0993
110B	34.396	-10.322	485	1595	0.3902	0.075
109	34.393	-10.218	492	1578	0.7875	0.1077
108	34.345	-10.134	466	1402	1.0803	0.1103
201	34.066	-10.098	132	571	0.3309	0.0626
202	34.111	-10.065	212	1293	0.6341	0.0877
203B	34.158	-10.031	312	1135	1.6518	0.1372
107	34.298	-10.048	450	1561	0.8802	0.0876
204	34.204	-9.997	386	1556	0.9535	0.0975
106	34.25	-9.963	375	1476	0.4034	0.0668
205	34.286	-9.939	400	970	0.621	0.0765
206B	34.32	-9.912	402	1449	0.8549	0.0954
105	34.205	-9.881	331	1271	0.7602	0.0824
104	34.157	-9.799	321	1545	1.0694	0.0934
103B	34.112	-9.716	265	974	1.8801	0.113

profiles. This down-sampling process reduced the number of observations from 101,496 to 45,208 (Table 3.1). We made all picks within the UTM coordinate system, and then applied a linear operator to convert to a local coordinate system for the remainder of this study. The origin of the local coordinate system is -12.03 N, 33 E. We set the Z=0 km in the local coordinate system to correspond to the elevation of the surface of Lake Malawi, which is at 454 m.

We took several steps to ensure high-quality, accurate picks. In 2-D refraction work, reciprocity checks are commonly used to ensure consistent phase identification (e.g., *Zelt*, 1999). While this approach is applicable to our three 2-D refraction lines, the 3-D experiment geometry precludes reciprocity checks for most picks. To ensure consistent phase identification, we checked that picks at line intersections were consistent for a given station. Additionally, after picking all data, we visually inspected maps of travel time picks for each individual instrument in unreduced time to ensure that there were no abrupt lateral variations in travel time and thus the same first-arriving phase was consistently picked.

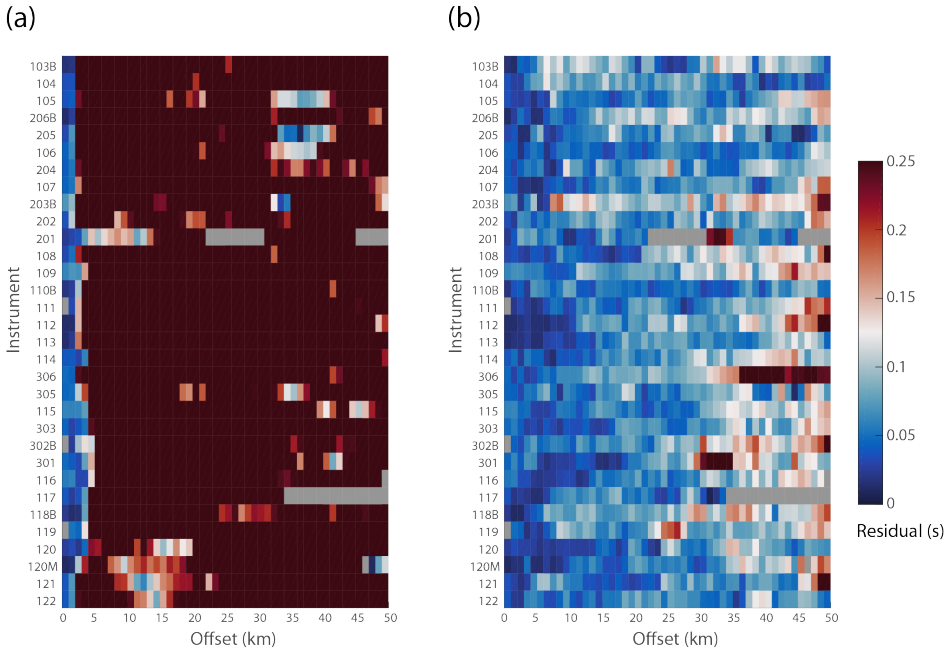

Figure 3.3: Comparison of misfit to an example initial model (a) and the final average model (b). The initial model shown in (a) achieved a chi-squared of 1.19 after 5 iterations. Misfit is shown for each instrument (y-axis) against the offset of the airgun shot. An obvious improvement in misfit occurs for offsets >5 km between the initial model and the final model.

3.3.3 Monte Carlo First Arrival Inversion Methodology

To obtain a 3-D model of P-wave velocity structure based on travel-time picks, we implement a Monte Carlo methodology using the iterative first-arrival tomographic inversion code FAST (First Arrival Seismic Tomography)(*Zelt and Barton*, 1998). A Monte Carlo approach to refraction imaging involves adding random noise to travel-time picks and performing numerous inversions with randomized initial models (e.g., *Korenaga et al.*, 2000; *Watremez et al.*, 2015; *Delescluse et al.*, 2015). This approach allows us to estimate model uncertainty.

3.3.3.1 Construction of Initial Models and Perturbed Travel Times

We constructed 200 unique 3-D starting models. Each initial model is parameterized with three layers where Layer 1 represents the water layer of Lake Malawi, which was estimated by fitting a surface to the estimated lake bottom in depth from >10,000 km of existing reflection lines (Figs. 3.1b, 3.1c) (*Lyons et al.*, 2011). Layers 2 and 3 represent a pseudo sedimentary layer and a crustal layer, respectively. All models extend from the lake surface to a depth of 15 km. To construct the 200 starting models, we randomly perturb three defining parameters of the velocity model: 1) Velocity at the base of Layer 2; 2) velocity at the base of Layer 3, and 3) the ratio between the thickness of Layer 1 (held constant) and the thickness of Layer 2. Parameters are varied between 30-50% (Fig. 3.2). For each initial model, we constructed a modified dataset of travel time picks defined as the original travel time picks with added random Gaussian noise, where the standard deviation of the

Figure 3.4 *(following page)*: Examples of seismic receiver gathers (top) and predicted ray paths (bottom) for shots along the primary 2-D along-strike transect within the 3-D survey (for location of the profile see Figure 3.1c). The top plots show the record sections with observed picks in blue and predicted picks in red. The height of the observed pick indicates the observational error for each observation. Bottom plots show the predicted rays paths (red) for the shown picks against contours of the final velocity model (black lines). Instrument names are given in the top left of each record section and can be located within the study region by referencing Figure 3.1c.

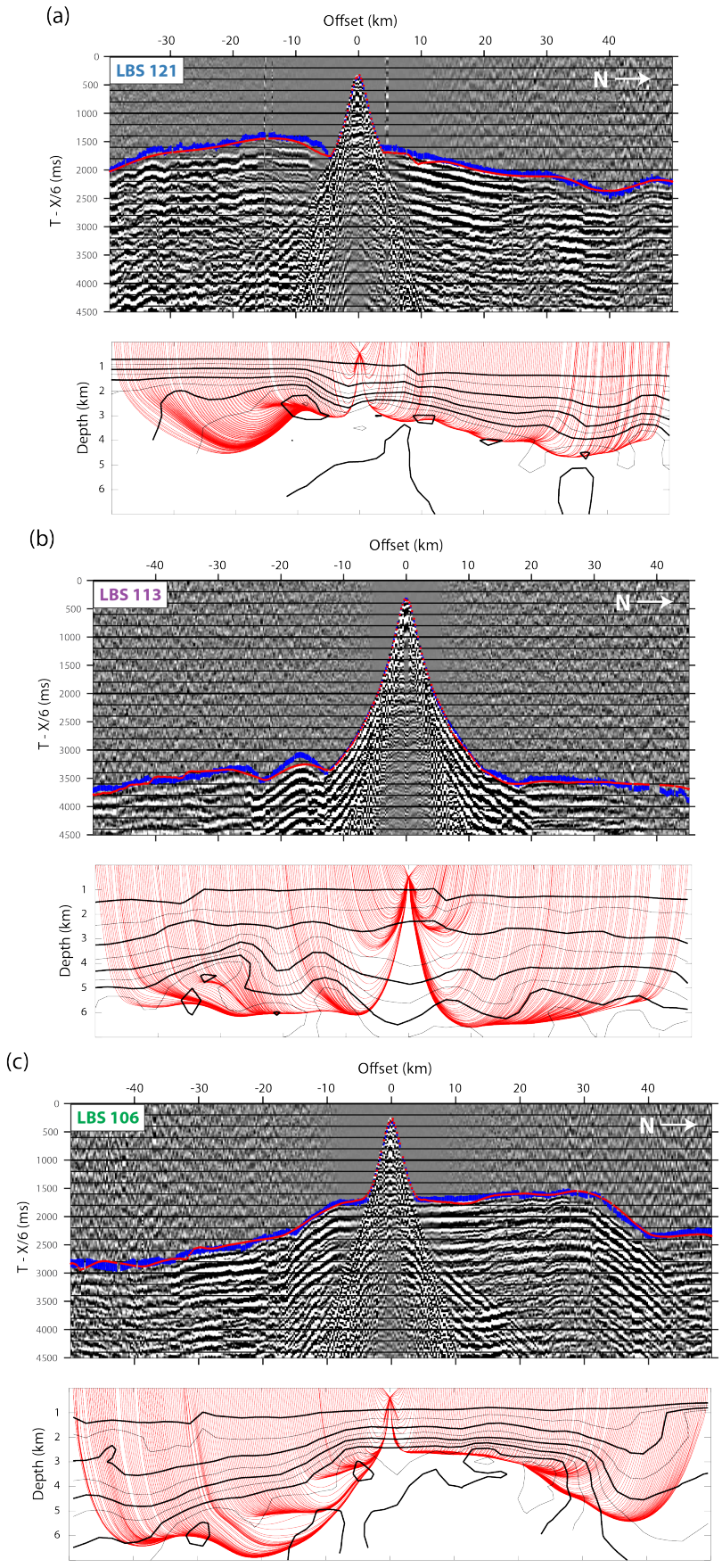
(a)
Offset (km)
-30 -20 -10 0 10 20 30 40
LBS 121
N
T - X/6 (ms)
0 500 1000 1500 2000 2500 3000 3500 4000 4500
Depth (km)
1 2 3 4 5 6
(b)
Offset (km)
-40 -30 -20 -10 0 10 20 30 40
LBS 113
N
T - X/6 (ms)
0 500 1000 1500 2000 2500 3000 3500 4000 4500
Depth (km)
1 2 3 4 5 6
(c)
Offset (km)
-40 -30 -20 -10 0 10 20 30 40
LBS 106
N
T - X/6 (ms)
0 500 1000 1500 2000 2500 3000 3500 4000 4500
Depth (km)
1 2 3 4 5 6

distribution is equal to the estimated pick uncertainty.

3.3.3.2 Travel Time Tomography with FAST

The FAST tomographic code (*Zelt and Barton*, 1998) aims to find the model with the least amount of structure that fits the data within their uncertainties. This is a linearized inversion where the velocity model and raypaths are updated after each iteration until the normalized misfit (χ^2) equals one or data misfits stop improving. χ^2 is defined as

$$\chi^2 = \frac{1}{N} \sum \frac{(t_{obs} - t_{pre})^2}{\sigma_{obs}^2} \tag{3.1}$$

where t_{obs} represents the observed arrival times, t_{pre} represents the calculated arrival times, N represents the total number of picks, and σ_{obs} represents the estimated uncertainty of the pick.

The forward step of FAST utilizes the 3-D finite difference eikonal solver of *Vidale* (1990) on a 0.5-km grid. For the inverse step, cell sizes are made larger (3 x 3 x 0.5 km in the x, y, and z direction, respectively) as larger cells have increased control on model parameters. Model updates during the inversion are calculated via a least-squares conjugate gradient method. The trade-off parameter, λ, which controls the regularization between data misfit and model smoothness, is systematically reduced with each iteration. This process stabilizes the inversion by first constraining long-wavelength structure before allowing finer structure in later iterations. We apply constraints on vertical and horizontal smoothness to ensure realistic earth structure. Smoothing increases with depth in the model, with the lower 7.5

Figure 3.5 *(following page)*: Examples of seismic record sections recorded along turns and lines of non-2-D geometry. The x-axis is in terms of shot number and thus scales with the length of a given refraction line. The orientation of the line is shown by labels in the top right/left corners of each record. Observed picks are shown in blue where the height of the tick mark scales with observational error reported. Predicted picks are shown by the red points. To ensure ease of comparing the predicted/observed picks to the data only every 5th pick is marked. A map for instrument/line locations is shown in (a) where the color of the instrument matches the color of the line for which shots are shown. The background grey lines show the entire 3-D survey. Instrument numbers are labeled in the bottom left corner of each record section and the color of the label matches the associated symbols in (a).

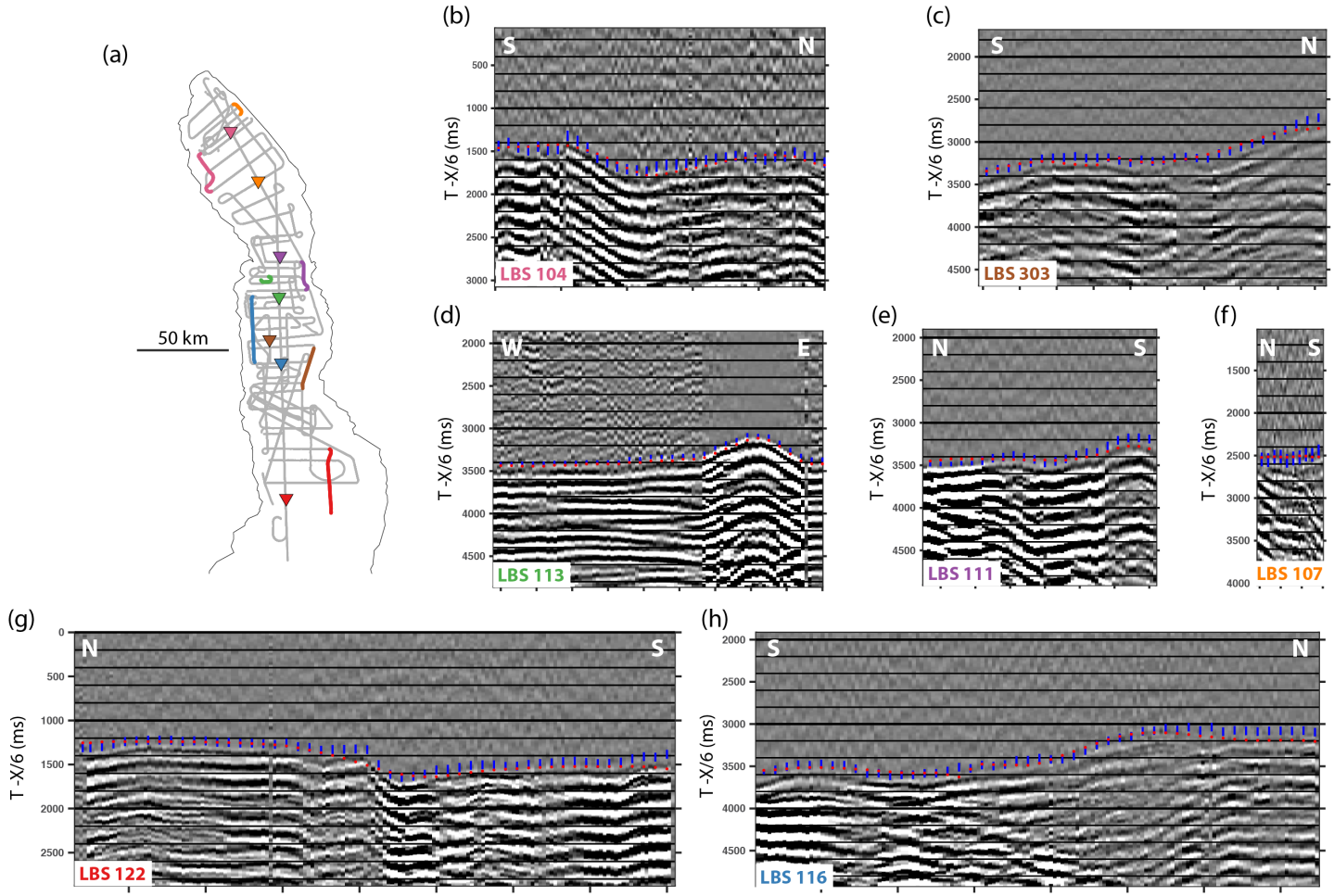
(a)
50 km
(b)
S
N
T -X/6 (ms)
LBS 104
(c)
S
N
T -X/6 (ms)
LBS 303
(d)
W
E
T -X/6 (ms)
LBS 113
(e)
N
S
T -X/6 (ms)
LBS 111
(f)
N
S
T -X/6 (ms)
LBS 107
(g)
N
S
T -X/6 (ms)
LBS 122
(h)
S
N
T -X/6 (ms)
LBS 116

km having a 50% larger smoothness weight. Typical inversions require 4-5 iterations before they are stopped either because χ^2 has reached 1 or the data misfit has stopped improving (Fig. 3.3). Of the 200 models, 198 models successfully converged. We present a single final model that is constructed by averaging all models with a χ^2 <1.25 (105 models), and we limit our discussion of results to this averaged model. To confirm the fit of this average model to the data, we trace rays through the model (Fig. 3.4) and calculate predicted travel times, χ^2 and RMS misfit (Figs. 3.4, 3.5). To quantify uncertainty, we calculate the standard deviation of the final velocity in each grid cell and then express it as a percent uncertainty of the final velocity.

3.4 Results

Our final 3-D model has a $\chi^2 = 1.08$, RMS = 102 ms, and traces 93.6% of all rays (Figs. 3.6, 3.7). Uncertainty estimates broadly mirror hit count and are lowest within the center of the model (<2%); particularly in the locations of slow velocities, interpreted as sedimentary basins. Uncertainties increase around the edges of the model and at greater depths. Larger uncertainties are also associated with parts of the model with large velocity gradients (i.e., the boundary between sediments and crystalline basement), which we attribute to the limited ability of the smooth first-arrival tomography method to recover sharp changes in velocity.

The 3-D velocity model represents the first 3-D tomographic model of basin-scale structure for the northern Malawi Rift and provides unprecedented access to deep basin structure relative to the collocated reflection experiment owing to short streamer lengths and the 2-

Figure 3.6 *(following page)*: Depth slices through the final model in terms of Vp (a,d,g), percent uncertainty (b,e,h), and hit count (c,f,i). Thick black lines indicate faults mapped in Mortimer et al. (2007), Lyons et al. (2011), and McCartney and Scholz (2016). The locations of the instruments are shown by the blue triangles in the right column. Color scales stay constant along the columns. Note that the hit count maps use a color scale with a maximum value of 20 rays to allow easier viewing of low-ray coverage areas.

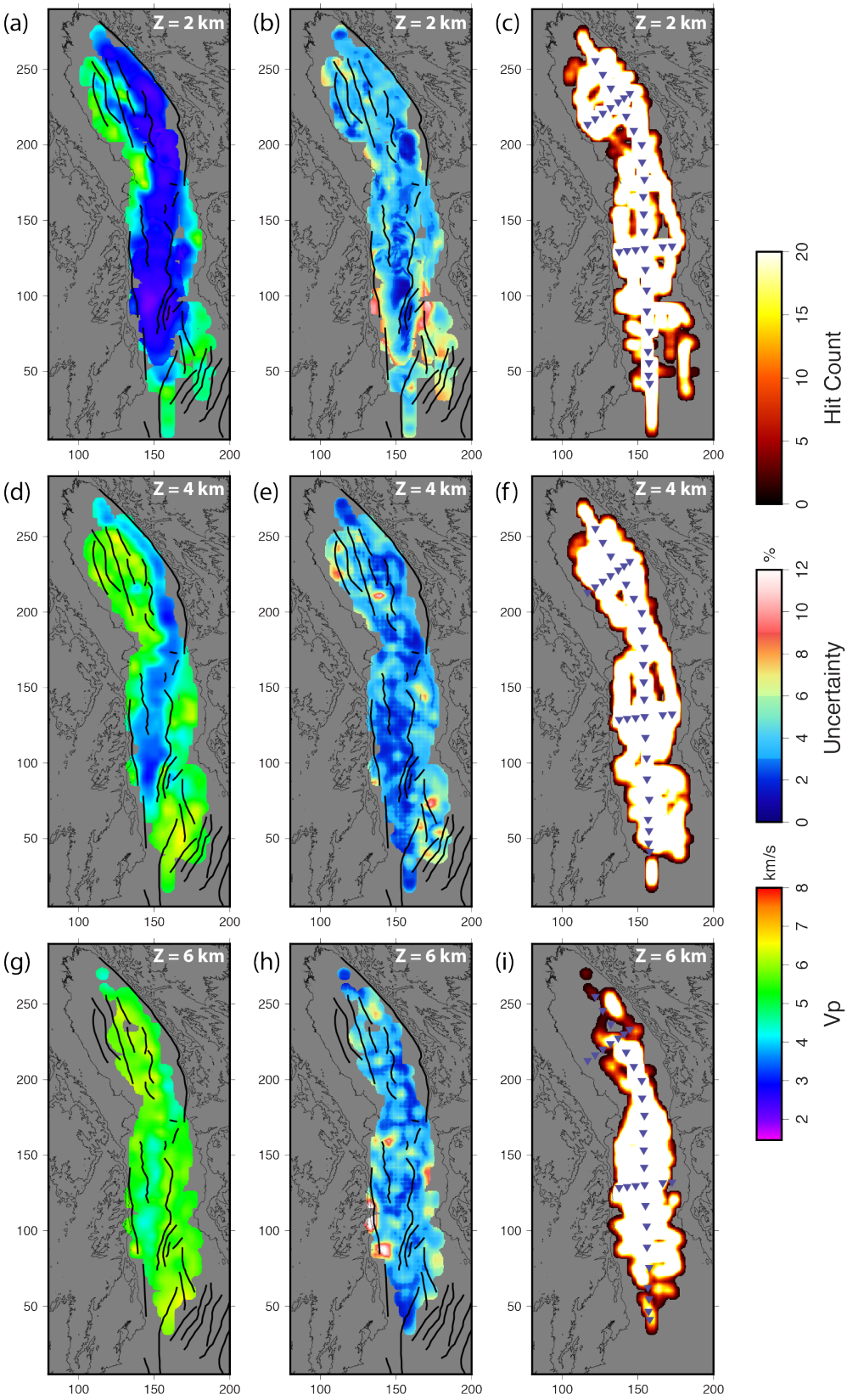
(a)
Z = 2 km
(b)
Z = 2 km
(c)
Z = 2 km
(d)
Z = 4 km
(e)
Z = 4 km
(f)
Z = 4 km
(g)
Z = 6 km
(h)
Z = 6 km
(i)
Z = 6 km
250
200
150
100
50
100
150
200
Hit Count
0
5
10
15
20
%
Uncertainty
0
2
4
6
8
10
12
km/s
Vp
2
3
4
5
6
7
8

D nature of that experiment. Our model reveals clear differences in the velocity structure between the North and Central basins (Fig. 3.6). In the North Basin, a shallow layer characterized by slow velocities (Vp <3.75 km/s) thickens to the east towards the Livingstone border fault (Figs. 3.6, 3.7b-d). The deepest occurrence of slow velocities is observed near the southern part of the Livingstone Fault (Fig. 3.7d); this region is also the location of the deepest bathymetry within the North Basin. Faster velocity ridges are observed along the center and western edge of the basin, both of which are oriented parallel to the strike of the basin. The central ridge separates the swath of low velocities against the border fault from a more limited region of slow velocities to its west (Figs. 3.6, 3.7c). The westernmost fast velocity ridge is clear only to depths of $\sim$ 3 km, below which much of the North Basin is characterized by velocities >6 km/s. In the northern part of the North Basin, a circular region (diameter $\sim$ 20 km) of slow velocities persists to depths >4 km. This feature is associated with abundant ray coverage (>50 rays), low uncertainty (Fig. 3.6), and clear changes in observed arrivals in LBS data (Fig. 3.4c), thus we consider it robust. South of Y=175, the package of slow velocity material shifts sinuously westwards until it abuts the northern segment of the Usisya Fault at Y=155. No high-velocity ridges or other structures are observed within the accommodation zone. Within this zone, slow velocities can be seen to thicken towards both the east and west sides of the basin (Fig. 3.7e).

The Central Basin is significantly more complex than the North Basin in both the types of structures present and the strike of the structures. Slow velocity zones thicken against each segment of the Usisya Fault. This slow velocity material is bounded on the east by a series of faults that define an intrabasinal high. Slow velocities persist to depths >5 km within the region bounded by the central segment and this intrabasinal high (between Y=80

Figure 3.7 *(following page)*: Cross-section slices through the final model in terms of velocity (top panels) and percent uncertainty (bottom panels). Locations of slices are shown on the map in (a) and are labeled on the individual cross-sections. All cross-sections are shown going from West on the left to East on the right. Color scales are constant amongst all cross-sections. The velocity cross-sections are contoured with thick black lines labeling every 1 km/s and thin black lines every 0.5 km/s.

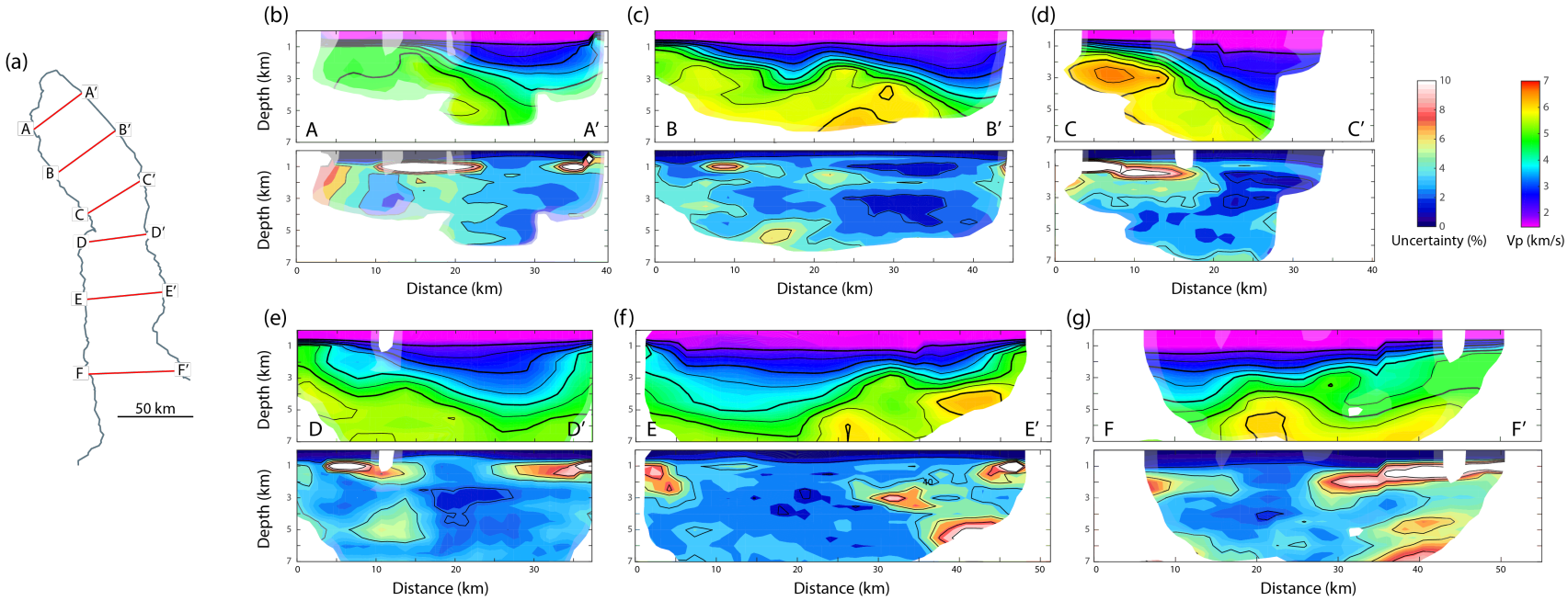
(a)
A′
A
B′
B
C′
C
D′
D
E′
E
F′
F
50 km
(b)
(c)
(d)
(e)
(f)
(g)
Depth (km)
Distance (km)
A
A′
B
B′
C
C′
D
D′
E
E′
F
F′
Uncertainty (%)
Vp (km/s)

and Y=120, Fig. 3.6), which corresponds to the deepest water in Lake Malawi (698 m). The Central Basin intrabasinal high is expressed in these profiles as a high-velocity structure (Vp >5.5 km/s) separating the region of low-velocity material against the border fault to the west and a shallower section of slow velocity material to the east. Structures attributed to the Lipichilli Fault Zone are most clearly seen in the cross-section profiles through the basin (Fig. 3.7f). South of the Lipichilli Fault Zone, slow velocities are nearly absent at depths >2 km, and instead velocities remain fast (Vp >5.5 km/s) throughout most of the profile. Between Y=130 and Y=175, cross-sections reveal a relatively thick (∼2 km) layer with velocities intermediate between those expected for synrift sediments and crystalline basement (∼ 3.75 - 4.5 km/s, Figs. 3.7e, f). This material is clearly distinct from other locations of slow velocities where the transition from slow (∼3 km/s) to fast (∼5 km/s) velocities occurs over very narrow depth ranges (i.e., ∼1 km, Figs. 3.7c, d).

3.5 Interpretation

3.5.1 Velocity Interpretation

To constrain the thickness of sedimentary sequences from our smooth 3-D tomographic model, which does not have interfaces, we approximate the sediment/basement boundary as a velocity contour (e.g., *Moeller et al.*, 2013). From both the LBS receiver gathers and the resulting velocity model, we identify three Earth layers based on variations in velocity and velocity gradient. We interpret a ubiquitous shallow layer, with velocities gradually increasing from 1.5 to ∼3.75 km/s, as a synrift sediment layer. These velocities are consistent with a normally compacting sedimentary section as is observed in ocean basins and other rift systems (e.g., *Hamilton*, 1976; *Moeller et al.*, 2013) and match patterns of sedimentation observed in SEGMeNT seismic reflection profiles (Fig. 3.8). Figure 3.9 shows a map of the depth to the base of this sedimentary sequence defined by the 3.75 km/s velocity contour.

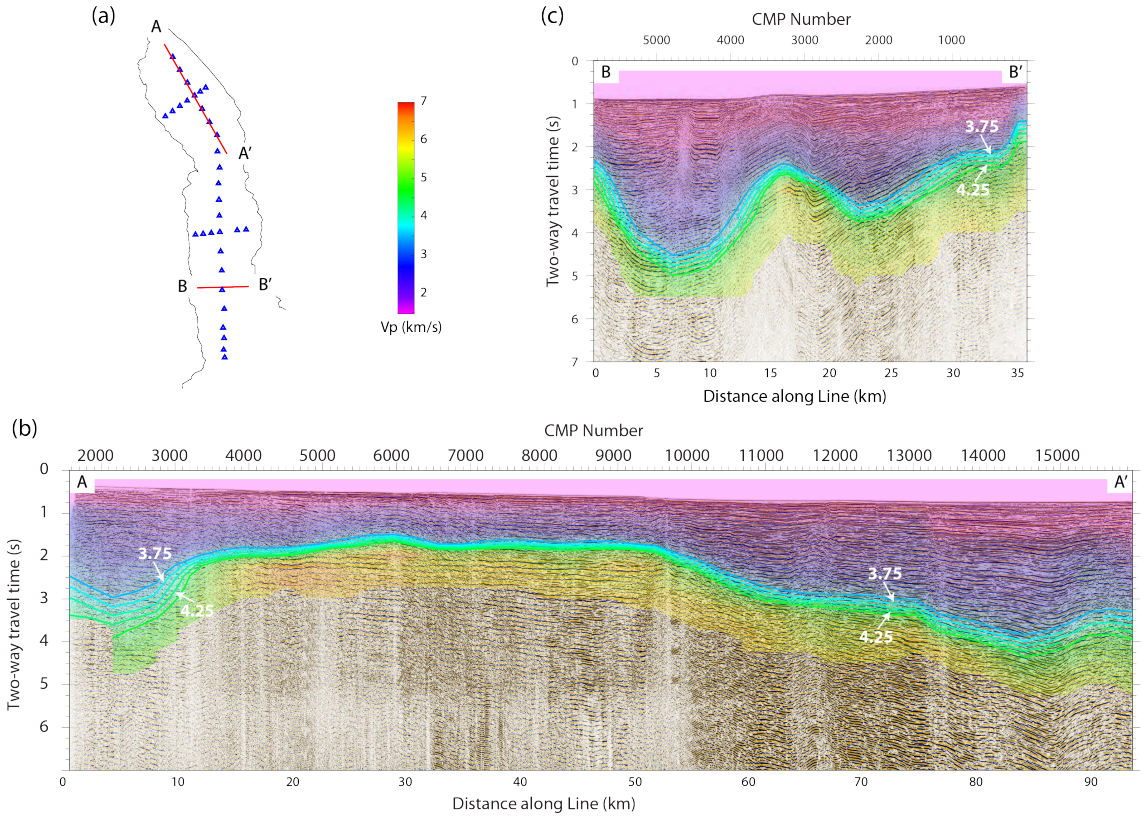

Figure 3.8: Comparison between time migration of SEGMeNT MCS reflection lines (background surface) and coincident 2-D profiles through the final velocity model (transparent color overlay) in TWTT. Five velocity contours are shown as thick colored lines at 0.25 km/s intervals between 3.5 and 4.5 km/s. Locations of the profiles are shown in the inset map (a). The velocity color scale and spatial scale is the same for both profiles. The velocity model is masked where there is no ray coverage. Acoustic basement in the reflection images is characterized by the low-frequency high amplitude arrival in both seismic lines.

In most of the study region, this sedimentary layer is directly underlain by a rapid increase to velocities of 5.5 - 6 km/s, consistent with upper crystalline crust (*Christensen and Mooney*, 1995). We choose a velocity contour of 4.5 km/s to approximate the top of crystalline basement, which lies within this high gradient zone. Our choice of 4.5 km/s for the top of the crust matches acoustic basement in SEGMeNT seismic reflection profiles in both the North and Central basins (Fig. 3.8).

In the northern Central Basin and northernmost North Basin, a 2- to 4-km-thick layer is observed between the slower velocity synrift sediments and the crystalline basement (Fig. 3.7e). This layer is characterized by intermediate velocities between the sediments and base-

ment (3.75 <Vp <4.5 km/s). First arriving refractions with apparent velocities of ∼4 km/s are clearly observed on receiver gathers from several LBS in the Central Basin (Fig. 3.4; 113, 114, 115, 116, 117, 301, 302B, 303) as well as instrument 103B in the northernmost North Basin. This interval has higher velocities and lower gradients than expected for compacting synrift sediments from the modern rift; accordingly, we interpret this intermediate velocity layer as sediment deposited during prior rifting episodes. This interpretation is supported by onshore outcrops of Karoo basins west and east of the accommodation zone and Karoo and Cretaceous-age basins north of the North Basin (Fig. 3.10), locations where reflection imaging shows weak or absent acoustic basement, and locations where the difference between the velocity characteristics of the synrift sediments and this sediment package are clear.

The continuation of sediments from earlier rifting episodes beneath both the North and Central basins of the Malawi Rift has been hypothesized previously. *Crossley* (1984) was one of the first to postulate that the Malawi Rift was underlain by preexisting sediment where it is crosscut by the Ruhuhu Basin and the Mwembeshi Shear Zone. Estimates of the thickness of this sedimentary package range from 1 km on the western shore in Malawi (*Kemp*, 1975) to ∼ 3 km in the Ruhuhu Basin (*Kreuser et al.*, 1990; *Wopfner*, 2002), suggesting that several kilometers of Karoo sequences may also be present beneath Lake Malawi. However, legacy reflection data provided limited velocity constraints, and if Karoo sequences were present beneath the modern rift fill, it would likely occur below acoustic basement (*Flannery and Rosendahl*, 1990; *Mortimer et al.*, 2016b).

Evidence for sediments deposited during prior rifting episodes is also documented north of Lake Malawi in the region between the Rukwa Rift and Lake Malawi. Karoo sediments and Cretaceous Red Sandstone Group sediments are widely distributed along the western side of the North Basin and RVP and continue northward into the Rukwa Rift (e.g., *Jacobs et al.*, 1990; *Roberts et al.*, 2010). These preexisting basins appear to strike subparallel to the trend of the North Basin, whereas the Ruhuhu Basin strikes nearly perpendicular to the trend of the Central Basin. Seismic reflection, borehole, and biostratigraphic data from

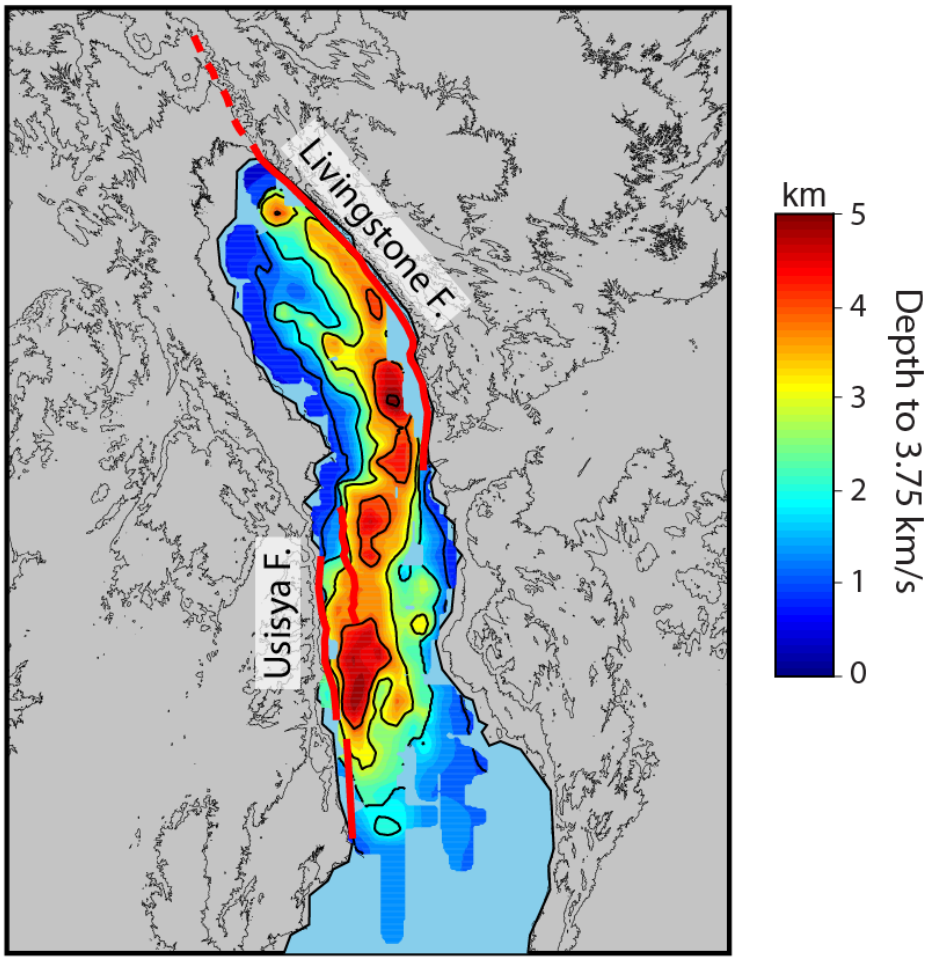

Figure 3.9: Depth to the base of synrift sediment defined by the 3.75 km/s velocity contour. Regions with no ray coverage are masked. Traces for the Livingstone and Usisya faults are shown by the thick red lines (*Mortimer et al.*, 2007; *Lyons et al.*, 2011; *McCartney and Scholz*, 2016). The onshore extent of the Livingstone Fault is approximated by the dashed red line.

the Rukwa Rift show that the Late-Pliocene-modern lake sediments are underlain by up to 10 km of Cretaceous to Paleogene Red Sandstone and Karoo sediments (*Kilembe and Rosendahl*, 1992; *Peirce and Lipkov*, 1988; *Wescott et al.*, 1991; *Roberts et al.*, 2004, 2010). Macrofauna in exposures of the Red Sandstone reveal a Cretaceous to Paleogene age for the Red Sandstones (*Roberts et al.*, 2010), which also crop out along the northwestern side of the North Basin. These basins do not extend south past the northwest shore of the North Basin.

Although previous studies have hypothesized the presence of sediment associated with older extensional basins beneath Lake Malawi, no direct observations were previously available and the single drill core in the Central Basin only reached a maximum depth of 380 m (*Scholz et al.*, 2011), well within the synrift sediment package. Figure 3.10 illustrates the thickness between the estimated base of synrift sediment and top of crystalline basement, which we interpret as sediment deposited during previous rifting episodes. This material has direct implications for the role of preexisting structures on rift evolution.

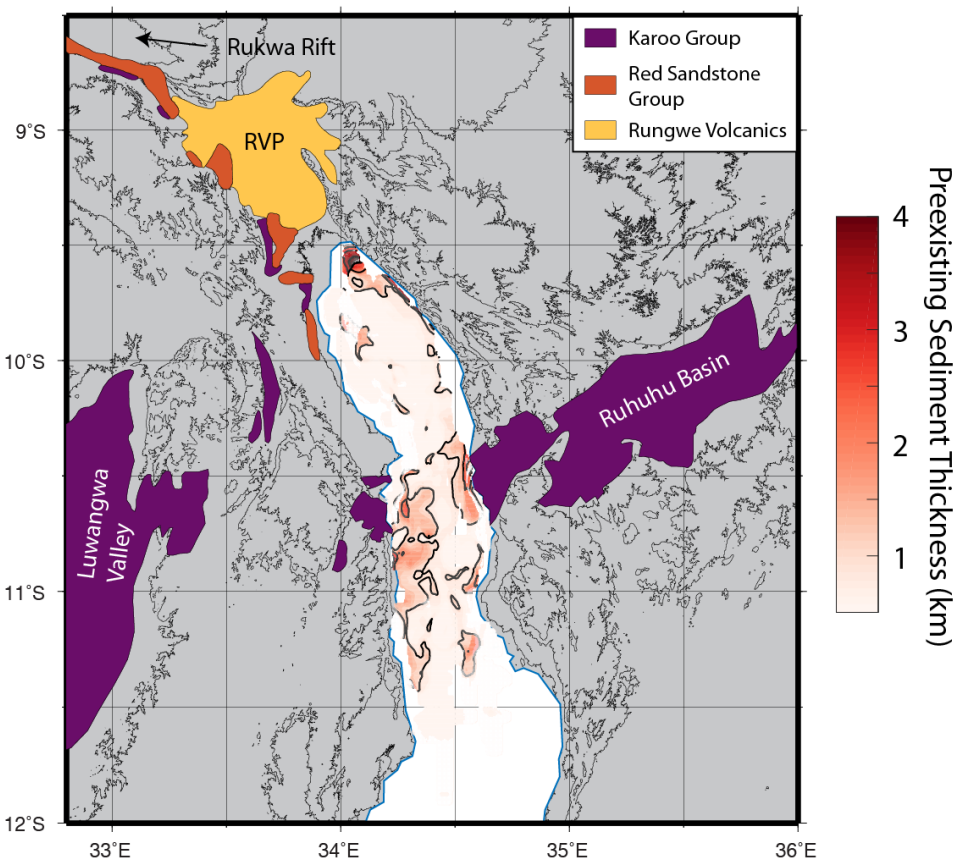

Figure 3.10: Map of thickness of sediments related to previous rifting episodes with simplified geologic map for comparison. Locations within the model with no ray coverage or velocity uncertainty >10% have been masked out. Geologic units were mapped following *Bennett* (1989), *Delvaux* (2001), *Pinna et al.* (2004), and *Roberts et al.* (2010). RVP; Rungwe Volcanic Province.

3.5.2 Estimating cumulative displacement profiles for the Livingstone and Usisya faults

Our 3-D velocity model provides unique constraints on 3-D patterns of synrift sediment thickness in a weakly extended rift. Together with constraints on footwall height from a 30-m digital elevation model from the Shuttle Radar Topography Mission (SRTM) (*Farr et al.*, 2007), these estimates of synrift sediment thickness can be used to constrain variations in the throw of the border faults bounding the North and Central basins.

Here we estimate cumulative vertical offset along the inferred lengths of the Livingstone and Usisya border faults. We calculate vertical offset along the border fault as the sum of the elevation of the footwall escarpment above lake level and the estimated depth to the base of synrift sediment below lake level. As this study is only concerned with cumulative vertical offset, we measure both footwall elevation and depth to the base of synrift sediment with respect to an arbitrary reference elevation - modern lake level. For more detailed analysis of the magnitude of footwall uplift compared to hanging wall downdrop, a calculation of a long-wavelength reference elevation would be needed. We do not calculate vertical offset for the onshore portion of the Livingstone Fault north of the lake due to a lack of sediment thickness constraints. To estimate footwall elevation, we extract profiles of elevation orthogonal to the strike of the border fault (the structural dip direction) from the SRTM (*Farr et al.*, 2007) following the procedure in *Ellis and Barnes* (2015). The maximum elevation for each dip profile is identified and then combined with all other measurements to create a strike profile along the border fault. We then adopt an iterative procedure to down-weight anomalously low elevations due to erosional features, such as river valleys (see Appendix B for details). Such erosional features suggest a reduction in the present-day elevation of the footwall, and thus our estimates of footwall height represent a minimum. To estimate depth to the base of synrift sediment, we use the continuation of the same profiles (orthogonal to the strike of the border fault) into the lake and identify the maximum depth of the 3.75 km/s velocity contour, interpreted as the base of synrift sediments. Locations with no ray coverage are

excluded. Total vertical offset is then estimated as the sum of the elevation of the footwall escarpment and the depth to the base of synrift sediment beneath the lake, with maximum values of 6.3 ± 0.5 km and 6.4 ± 0.4 km on the Usisya and Livingstone faults, respectively. By assuming a dipping fault, we estimate fault throw from the vertical offset measurements. Previous reflection studies that were limited to the top few kilometers of the basins predict dip angles of 60°-70°for the Livingstone Fault (*Wheeler and Rosendahl*, 1994), and onshore measurements of fault dips are 60°-75°(*Ebinger*, 1989a). Additionally, focal mechanisms from the Malawi Rift indicate that fault dips of ∼60°continue to lower crustal depths in some parts of the Malawi Rift (*Jackson and Blenkinsop*, 1993a; *Ekström et al.*, 2012). Given fault dips between 75°and 60°, the fault throw would be between 7.3 and 8.9 km for the Usisya Fault and 7.4 and 9.0 km for the Livingstone Fault. Hereafter, we assume a dip of 75°, which gives a more conservative estimate for fault throw compared to estimates using shallower dip angles.

Figure 3.11 shows estimated displacement profiles for the North and Central basins. The Livingstone Fault measures ∼140 km long with an additional ∼ 30 km continuing onshore north of Lake Malawi and into the RVP, for a total length of 170 km. The Usisya border fault system measures ∼140 km. Our estimated fault throw of 7.3 km for the Usisya Fault is higher than that reported by *Contreras et al.* (2000) (6.4 km) based on legacy seismic reflection data, likely owing to their use of TWTT as a proxy for sediment thickness, as well as the assumption that footwall uplift is approximately equal to hanging wall downdrop.

3.6 Discussion

3.6.1 Border fault overlap, accommodation zone structure and implications for fault growth models

Our 3-D velocity model and estimated displacement profiles for the two faults provides insight into how border faults interact and partition strain at accommodation zones. Additionally, our imaging shows no indication for thickening of sediments against the proposed Mbamba Fault (Figure 3.9), indicating that the southeastern edge of the Central Basin

likely is not bounded by a border fault as proposed by *McCartney et al.* (2016). Our estimates of synrift sediment distribution suggest the presence of an accommodation zone with a 4.3-km-thick sediment package, which smoothly shifts from an eastward thickening section within the North Basin to a westward thickening section in the Central Basin (Figs. 3.9, 3.11). Footwall elevation on either side of the accommodation zone is limited. Cross-sections across the accommodation zone reveal a symmetric basin, suggesting that the border faults overlap and both influence this region (Fig. 3.6a, d). Estimating the length of overlap is not straightforward from the subaerial fault traces alone, given that the northern segment of the Usisya Fault is mostly submerged. We consider the length of overlap as the length of the region between the two basins where sediments thicken both to the west and the east in our velocity model (i.e., Fig. 3.7e), estimated at $\sim$ 20 km.

Our observations are broadly consistent with imaging of the accommodation zone by Project PROBE (*Scholz*, 1989), which show it to be a broad low-relief feature (*Specht and Rosendahl*, 1989) similar to accommodation zones observed in other parts of the Western Rift (*Rosendahl*, 1987). A small topographic high is also interpreted within this broad low relief zone (*Specht and Rosendahl*, 1989; *Flannery and Rosendahl*, 1990), which *Flannery and Rosendahl* (1990) attributed in part to the intersection with the Ruhuhu Basin. We do not observe any positive relief feature within this zone in our velocity model, but it may be too small to resolve with our study.

To explore the impact of fault overlap on basin development, we examine fault displacement profiles where the faults likely overlap (Fig. 3.11). Summed offsets along both faults remain nearly constant at $\sim$4.5 km at the cross-over between the two faults. Indeed, the combined profile of total fault offset for the Usisya and Livingstone faults resembles a flattened bell-shaped curve expected for a single fault or an array of faults and observed in other rifts (e.g., *Nixon et al.*, 2016). The only clear indications of the separations between the two faults are in the topographic traces where both the Usisya and Livingstone faults reach topographic lows at their intersection (Fig. 3.11).

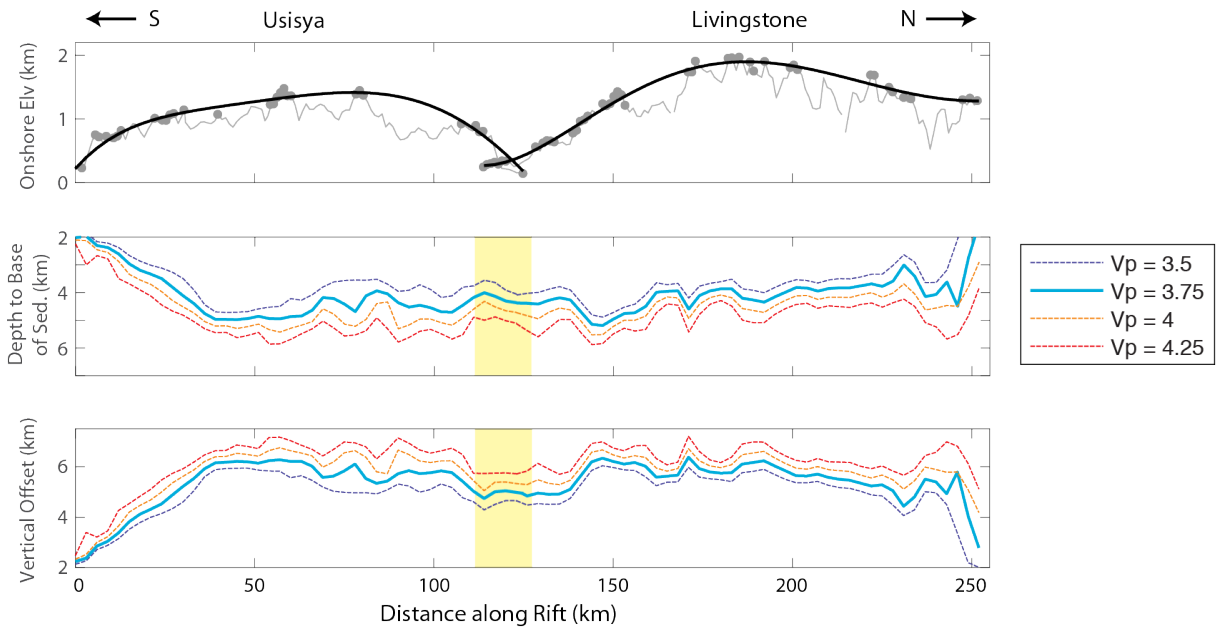

Figure 3.11: Profiles of elevation, depth to base of synrift sediments, and vertical offset for the Usisya (left, east dipping) and Livingstone (right, west dipping) faults plotted together. Profiles of elevation (top row) are taken along the footwall escarpment. The full elevation profile is shown as the thin grey line, the locations where elevation was taken for the final elevation profile is shown by the grey dots, and the final elevation profile is shown by the black line. Profiles of the depth to the base of synrift sediment (middle row) are shown for a range of velocities whereby the velocity defines the base of the sediment column. Profiles of total vertical offset (elevation above lake level + depth to the base of synrift sediment) are shown for the same range of velocity contours in the bottom row. Our preferred model is shown as the thick blue contour. The yellow rectangle shows the approximate region of fault overlap within the accommodation zone.

Using analogue clay models, *Paul and Mitra* (2013) tested the influence of fault overlap and separation on accommodation zone structure, and found that low-relief accommodation zones (e.g., *Rosendahl*, 1987) are nearly ubiquitous in systems with basin bounding faults that dip toward each other. Many authors have suggested that in regions of fault tip overlap accommodation zones tend to be narrow and strike nearly parallel to the trend of the basins (e.g., *Morley et al.*, 1990; *Faulds and Varga*, 1998; *Paul and Mitra*, 2013). Where no overlap exists, accommodation zones are wide and strike parallel to the extension direction. Our imaging shows that the accommodation zone strikes nearly parallel to the trend of the basins and is ∼20 km wide (Fig. 3.6d), consistent with predictions, and yielding a broad

depositional apron between the two depocenters (e.g., *Scholz*, 1995b). We conclude that significant fault-tip overlap exists at the accommodation zone between the Livingstone and Usisya faults and the combined motion on these faults results in deep, continuous sediment infill between the two basins.

In the region of fault-tip overlap, our profiles of displacement show a thick sedimentary section (∼4.3 km) and relatively large vertical throw (∼4.5 km). We hypothesize that the southern end of the Livingstone Fault and northern end of the Usisya Fault must have been active in the region from a very early stage to generate this much vertical offset at their intersection. Using reflection imaging, *Morley* (1999) showed that many basins within the EARS achieved their fault length early leading to nearly stationary locations of fault tips for most of the lifespan of the basins. Within the Central Basin, *McCartney and Scholz* (2016) similarly found that intrabasinal faults established their length rapidly through the linkage of fault segments. These observations match predictions from the constant-length model, whereby fault length is established rapidly and varies little afterward, allowing displacement to accrue through time (e.g., *Morley*, 2002; *Walsh et al.*, 2002; *Nicol et al.*, 2005; *Curry et al.*, 2016). Note that the thermochronological study of the Livingstone Fault by *Mortimer et al.* (2016a) found that segments may not have linked until very recently (∼ 1.6 Ma), and the stratigraphic analysis of *Contreras et al.* (2000) on the Usisya Fault argued for alternating periods of increasing fault length and/or fault displacement. We suggest the observation of significant displacement across the overlapping fault tips of the Livingstone and Usisya faults signifies the early establishment of their respective fault lengths.

3.6.2 Variations in intrabasin structure and the role of preexisting features

Nearly every aspect of the rifting process is thought to be influenced by preexisting structures, from rift initiation through to plate rupture. However, obtaining direct constraints on the relationship between remnant structures and rift evolution is challenging as extensional processes often overprint remnant structures. Our 3-D velocity model of the Malawi Rift provides unique constraints on several influential preexisting features beneath this early

stage rift. As introduced in Section 3.5.1, Late Paleozoic Karoo-age and Cretaceous basins are observed onshore, and our velocity model reveals associated thick packages of preexisting sediment in both the North and Central basins (Fig. 3.10).

Within the Central Basin, these units sit between the Ruhuhu Basin to the east and the Usisya Fault to the west, with an average thickness of ∼1.5 - 2.5 km covering an area of $\sim$ 250 km^2. Reflection imaging shows clear acoustic basement reflectors over most of the Central Basin (*McCartney et al.*, 2016)(Fig. 3.8c) except in regions where the interpreted preexisting sediment is present (*Specht and Rosendahl*, 1989; *Scholz*, 1989). Onshore of the Central Basin, estimates of the thickness of Karoo-age sediments are 1-3 km (*Kemp*, 1975; *Kreuser et al.*, 1990; *Wopfner*, 2002) and are limited to the Ruhuhu Basin east of the lake and small, isolated outcrops opposite of the Ruhuhu Basin on the west side of the lake. We thus suggest that the package of preexisting sediment imaged in the Central Basin is likely the continuation of the Karoo-age Ruhuhu Basin offshore beneath Lake Malawi. The trend of the Ruhuhu Basin is oriented ∼45°to the strike of the Central Basin and Usisya border fault, and is primarily located within the accommodation zone and the northern Central Basin.

Within the North Basin, estimated preexisting sediments are much thicker (up to 4.6 km) and localized within the northernmost part of the basin. Seismic reflection data and LBS receiver gathers show that the southern edge of this North Basin feature is sharp. The base of this sedimentary package is obvious in reflection imaging as a low frequency reflector at $\sim$ 4 s TWTT that abruptly shallows to ∼2 s TWTT (Fig. 3.8b). Up to 10 kilometers of Cretaceous Red Sandstone and Karoo-age sediment are documented in the Rukwa Rift (*Kilembe and Rosendahl*, 1992; *Peirce and Lipkov*, 1988; *Wescott et al.*, 1991; *Roberts et al.*, 2004, 2010), and these rocks outcrop along the northwestern edge of the North Basin (Fig. 3.10); accordingly, we suggest that the preexisting material in the northernmost North Basin represents one or both of these sedimentary packages.

Preexisting structures appear to influence the development of intrabasin and basin struc-

ture in both the North and Central basins (*Mortimer et al.*, 2007, 2016b; *Wheeler and Karson*, 1989; *Morley*, 2010) and the accommodation zone between them. We highlight the correlation between the relatively simple intrabasinal faulting of the North Basin and the limited extent of prior rifting-related material there ($\sim$ 5% of the basin) compared to the complex faulting within the Central Basin and the broad extent of prior rifting-related material there ($\sim$25% of the basin). *Mortimer et al.* (2016b) attributed the increased complexity of structure within the Central Basin to the presence of Karoo-age preexisting structures that cross-cut the basin. However, *McCartney and Scholz* (2016) instead suggest that complex intrabasinal faulting may have been primarily influenced by the underlying Proterozoic basement fabric, similar to what has been observed in other rifts (*Nixon et al.*, 2016). The variation in intrabasinal complexity between the Central and North basins likely results from a combination of factors, including the presence of inherited Karoo-age to Cretaceous structures as mapped in this study.

Our observations of preexisting sediment in the northernmost part of the North Basin expand on evidence for prior rifting-related sediments onshore (e.g., *Jacobs et al.*, 1990; *Roberts et al.*, 2010), and are consistent with predictions from balanced stratigraphic cross-sections (*Ebinger et al.*, 1989). We suggest that this preexisting material represent the remnants of larger extensional basins that continue from the Rukwa Rift into the northern North Basin. These prior rifting-related packages of sediment mapped by this study is further evidence of a long-lived corridor of extension along the Tanganyika-Rukwa-Malawi segment of the EARS (*Delvaux*, 2001, 1991) active over multiple rift phases since the Late Paleozoic.

3.6.3 Implications for normal fault growth

Our estimates of fault throw across the two border faults bounding the northern Malawi Rift are used together with fault lengths to evaluate influences on the growth of large normal faults. The dimensions of the Usisya and Livingstone faults illustrate the dominant control of elastic thickness, the integrated mechanical strength of the lithosphere, on fault

growth as shown by many previous studies (e.g., *Ebinger et al.*, 1991); long faults form in regions of large T_e. Large faults such as those observed along the Western Rift, are thought to form through the growth and linkage of smaller fault segments (e.g., *Cartwright et al.*, 1995; *Dawers and Anders*, 1995), which results in a displacement profile in the shape of a flattened bell curve where displacement increases from zero at the fault tips to a central maximum. Both displacement profiles for the Livingstone and Usisya faults broadly resemble this model, exhibiting maximum estimated throws at their centers and decreasing throws towards their tips. We expect that both the Usisya and Livingstone faults have grown by similar mechanisms (i.e., constant length vs. isolated fault), consistent with studies of border fault systems elsewhere along the Western Rift (*Morley*, 1999). Further, the Livingstone and Usisya faults are both likely mature and at similar stages in their evolution, consistent with our observations of significant displacement on both faults (discussed further in Section 3.6.2). While both faults contain discrete segments, these segments are now thought to be presently linked in agreement with models of fault growth via segment linkage, though the timing of the linkage is debated (*Contreras et al.*, 2000; *Mortimer et al.*, 2016a). Although the Usisya and Livingstone faults have similar overall dimensions, in detail they differ. Both faults have the same estimated displacement ($\sim$7.3 km), but the Livingstone Fault is 30 km longer (170 km versus 140 km).

A characteristic parameter invoked in the discussion of fault dimension is the ratio between fault displacement and fault length. As introduced above, different models of fault growth (constant length vs. isolated fault) predict different relationships between displacement and length where the constant length model suggests an increase in the displacement-length ratio during a fault's life while the isolated fault model predicts approximately a constant ratio at all times. We've shown in Section 3.6.1 that the constant length model is likely appropriate for the Livingstone and Usisya faults given the implication for the early establishment of their lengths. Comparisons with the small number of available constraints on displacement for other large faults in strong lithosphere indicate that the fault throws

and displacement-length ratios estimated by this study are similar to or greater than those of other large normal faults. The displacement-length ratios for both faults (0.04 and 0.05) are slightly above the observed global mean of $\sim$ 0.03 (*Kim and Sanderson*, 2005). For comparison, other faults in the Western Rift with fault throw constraints (the Kivu-Rusizi Rift and Bunia Fault in the Albertine Rift) have lengths of $\sim$100 km and 75 km and fault throws of 2-5 km and 5.3 km, respectively (*Ebinger*, 1989a; *Upcott et al.*, 1996). In the Baikal Rift, basin lengths are between 160-240 km, and synrift sediment deposits vary from 4 to 7.5 km (*Hutchinson et al.*, 1992). While fault displacement has been broadly observed to scale with fault length (e.g., *Dawers and Anders*, 1995; *Schlische et al.*, 1996), some faults reach large lengths with small throws. For example, the Kanda Fault in the Rukwa Rift is 160 km long and has a maximum fault scarp elevation of only $\sim$45 m (*Delvaux et al.*, 2012), and the Bilila-Mtakataka border fault in the southern Malawi Rift is $\sim$100 km long and has only $\sim$ 1 km of sedimentary strata (*Jackson and Blenkinsop*, 1997).

As discussed above, the significant length of both the Livingstone and Usisya faults indicates that T_e should be large in this region, consistent with observations of long fault traces and high T_e in other parts of the Western Rift (for a review see *Ebinger et al.*, 1999). *Pérez-Gussinyé et al.* (2009) use coherence between topography and Bouguer gravity to estimate T_e of $\sim$35-55 km in our region, with the lower values occurring around the RVP and the North Basin and higher values in the Central Basin. Forward models of 2-D profiles provide more detail on spatial variations than is possible with spectral averaging methods, and suggest that T_e is 36 km across the faulted North basin (*Ebinger et al.*, 1991). These estimates are consistent with a higher expected thermal gradient associated with the RVP, and the potential there for thinned lithosphere as has been suggested from upper mantle imaging studies (e.g., *O'Donnell et al.*, 2016; *Accardo et al.*, 2017). Broadly, the estimated variations in T_e within the Malawi Rift predict the opposite trend in border fault length to what we observe, whereby the Livingstone Fault should be shorter than the Usisya Fault (rather than $\sim$30 km longer) given the proximity of the RVP to the North Basin. This suggests that

additional mechanisms, such as the presence of volcanic loads, erosion and sedimentation, and preexisting features, also influence the lengths and displacements of the Livingstone and Usisya faults.

In addition to presenting a longer fault trace, the Livingstone Fault also exhibits a significantly higher footwall escarpment (∼1900 m) compared to the Usisya Fault (∼1500 m). This excess elevation may be related to the fault's proximity to the East African Plateau and/or the RVP, which itself has significant topography (see Fig. 3.1a). Removing the linear positive trend of the Livingstone Fault would make the elevations of Livingstone and Usisya faults nearly identical. The proximity of the RVP to the Livingstone Fault may have also influenced the growth of the fault. Volcanoes act as loads on the plate and can perturb the local stress field (e.g., *ten Brink*, 1991). In rift settings, modeling has shown that the presence of a volcanic load can increase the extensional stress, promoting fault growth locally (*van Wyk de Vries and Merle*, 1996). Volcanic loads have been shown to have influenced faults in several rifts within the EARS including the Asal Rift (e.g., *De Chabalier and Avouac*, 1994) and the Kivu Rift (*Wood et al.*, 2015). The presence of the long lived RVP (established ca 17 Ma; (*Rasskazov et al.*, 2003; *Mesko et al.*, 2014), is one mechanism that may have acted to perturb the stress field and promote the long fault trace of the Livingstone Fault.

Preexisting structures such as remnant faults, basement fabrics, and large-scale shear zones are thought to strongly influence fault behavior in a variety of ways as documented in many locations including the North Sea (e.g., *Bartholomew et al.*, 1993; *Whipp et al.*, 2014), the Red Sea (e.g., *Moustafa*, 2002), the Baikal Rift (*ten Brink and Taylor*, 2002), and several locations in the EARS (e.g., *Smith and Mosley*, 1993; *Ebinger et al.*, 1997; *Katumwehe et al.*, 2015; *Ring*, 1994). The Karoo-age Ruhuhu Basin represents a prominent preexisting structure that intersects the Malawi Rift at the juncture between the North and Central Basins (e.g., *Catuneanu et al.*, 2005), and associated faults are likely oriented nearly orthogonal to the strike of the Livingstone and Usisya faults. *Versfelt and Rosendahl* (1989) propose that the intersection of this structure may have influenced the change in polarity between the two

border faults. Additionally, given the nearly orthogonal strike of the Ruhuhu Basin, propagation of the border fault tips into the region may have been inhibited, ultimately limiting the northern extent of the Usisya Fault and/or the southern extent of the Livingstone Fault.

Several studies suggest that strongly foliated basement fabrics can locally re-orient the stress field (e.g., *Morley*, 2010; *Corti et al.*, 2013; *Reeve et al.*, 2015) and may allow the rapid establishment of long fault traces along these zones of weakness. In practice, this mechanism has been used to explain the development of long faults in several Western Rift systems like the nascent Okavango Rift (*Kinabo et al.*, 2008), the Rukwa Rift (*Theunissen et al.*, 1996; *Delvaux et al.*, 2012), and the southern Malawi Rift (*Jackson and Blenkinsop*, 1997; *Ebinger et al.*, 1999). However, the influence of inherited structures is dependent on their orientation with respect to the regional stress field (e.g., *Daly et al.*, 1989). For example, recent study of the 100-km long Bilila-Mtakataka Fault in southern Malawi finds that the fault may only exploit basement foliations locally where foliations are well oriented for reactivation (*Fagereng et al.*, 2017).

For the North Basin, many authors highlight the marked parallelism between the underlying Ubendian basement foliations and the trend of the Livingstone Fault and the basin as a whole (e.g., *Wheeler and Karson*, 1989; *Mortimer et al.*, 2007; *Ring*, 1994). *Wheeler and Karson* (1989) and *Ring* (1994) mapped previously active faults, synrift faults, and foliations to suggest that growth of the Livingstone Fault included reactivation of optimally oriented planes of weakness within the Proterozoic shear zone (present day opening is thought to be W-E; Saria et al., 2014). Foliations within the Ubendian Belt are steeply dipping and exhibit a pronounced preferential strike, dominantly NW-WNW (e.g., *Wheeler and Karson*, 1989; *Ring*, 1994; *Fritz et al.*, 2009). In contrast to the North Basin, the relationship between inherited faults/foliations and synrift structure in the Central Basin is less clear. The Central Basin is underlain by the Mozambique Belt, which is characterized by more moderately dipping foliations with no single preferred orientation (*Theunissen et al.*, 1996; *Fritz et al.*, 2009), and *Ring* (1994) finds that for most of the Usisya Fault the strike of the fault has

no relationship to the foliation of the basement fabric. This suggests that the Livingstone Fault may have propagated farther because it took advantage of basement structures that were optimally oriented with respect to the local stress field, as suggested by *Ebinger et al.* (1999). Note that the markedly different character of preexisting fabric between the two faults does not seem to have influenced fault displacement, given that they accommodate similar amounts of slip, as previously speculated by *Ring* (1994).

Localized sediment delivery in the Central Basin may have also facilitated displacement on the Usisya Fault. Modeling studies show that increased sediment delivery leads to prolonged growth on border faults (*Bialas and Buck*, 2009; *Corti et al.*, 2010, 2013). One marked difference between the North and Central basins is the mechanisms of sediment delivery. Two drainage systems terminate in the Central Basin (S. Rukuru, and the Ruhuhu) (e.g., *Johnson et al.*, 1995) and together have provided sustained, structurally controlled sediment delivery to the major depocenter of the Usisya Fault for much of its lifespan (*McCartney and Scholz*, 2016; *Soreghan et al.*, 1999). Mud diapirs are observed in reflection imaging within this depocenter (*Flannery and Rosendahl*, 1990) and are often interpreted as an indication of rapid sedimentation. In contrast, in the North Basin, the Livingstone Mountains generally deflect drainage away from the basin excepting a few small rivers that incise through the steep footwall scarp (Fig. 3.1). The Songwe-Kiwira system delivers sediment onto the axial margin of Lake Malawi from the north and progrades down axis (*Scholz*, 1995a) and additional sediment enters the North Basin from the Ruhuhu River in the south (*Lyons et al.*, 2011). The long-term, structurally controlled delivery of sediment to the major depocenter of the Usisya Fault represents one process that could promote displacement on the fault. The marked contrast in sediment delivery processes in these two basins provides an additional basin-scale mechanism which may influence the growth of these faults.

3.6.4 Implications for fault lifespan

Understanding the maximum size of the Livingstone and Usisya faults has important consequences for both the state of the rift system (i.e., whether strain has migrated inwards

to new faults) as well as present day seismic hazard for the region. Several factors may control the maximum length and/or displacement that a fault can achieve. Numerous studies have shown that continued motion on a normal fault is favored by the difficulty in breaking a new fault but resisted by the need to overcome flexural restoring forces and the weight of the accumulated topography (e.g., *Forsyth*, 1992; *Buck*, 1993). *Scholz and Contreras* (1998) proposed an empirically constrained model for estimating maximum fault length/displacement in the context of rift systems. Utilizing a constant displacement-length scaling of ∼0.03, and a modest value of T_e, this simple model predicts a maximum fault throw of ∼ 5km for the Usisya Fault. This value is comparable to but smaller than the throw we observe, suggesting that the fault may be nearing the end of its lifespan.

Olive et al. (2014) propose an alternative theoretically based model, which suggests that surface processes of footwall erosion and hanging wall deposition may increase the life of a fault and hence its maximum achievable throw. Normal fault systems with a high rate of footwall uplift relative to erosion rate predict fault abandonment after relatively small total displacement, while systems with higher erosion rates relative to uplift can produce much greater total throw. The latter produces systems with a very muted topographic change between the hanging and footwall, while the former retains a distinct topographic profile. For the Malawi Rift, the significant topographic profile suggests that erosion has been relatively slow compared to uplift rates, despite moderate present-day rainfall in the region (>1.5 m annually in some regions)(*Nicholson et al.*, 2013). With an estimated characteristic faulted layer thickness of ∼30 km (*Foster and Jackson*, 1998), *Olive et al.* (2014) predict fault abandonment after only a few kilometers of displacement for the no-erosion end member. Models with modest erosion such that significant relief is retained suggest maximum fault displacements of ∼ 5 km prior to abandonment, again below our estimates of present-day fault throw (*Olive et al.*, 2014). From both empirical (*Scholz and Contreras*, 1998) and theoretical (*Olive et al.*, 2014) perspectives, it is likely that both faults are very close to, if not at, their maximum throw.

Seismicity and detailed faulting studies will ultimately be essential to determine if activity continues on the border faults. Additionally, both models discussed here are 2-D and make several simplifying assumptions like homogeneous sedimentary infill of the hanging wall, no preexisting topography or inherited structures, and no large-scale loads (i.e., volcanic centers), all of which are factors that may act to influence fault lifespan in our study region. Nevertheless, our observations suggest that Livingstone and Usisya faults are likely near or at their maximum size suggesting that a migration of strain inwards onto presently active intrabasin structures may be imminent.

3.7 Conclusions

We use seismic refraction data acquired by LBS to create a 3-D P-wave velocity model of the northern basins of the Malawi Rift. This model provides new, unique constraints on basin and upper crustal structure in a weakly extended rift that can be used to understand normal-fault growth, the formation and evolution of accommodation zones, and the role of preexisting structures on rift development. We present new constraints on total offset on the Livingstone and Usisya faults and find that both faults have accumulated significant vertical offset ($\sim$6.3 km). We combine this with estimates of fault length to calculate displacement-length ratios for both faults which provide unique constraints for faults of such great length. We attribute the similar magnitude of fault displacement and $\sim$30 km variation in fault length between the two faults to the influence of preexisting structures, differences in sediment delivery to the basins, and the influence of the RVP as a volcanic load. The significant displacement accommodated on both faults indicates that the faults are likely near their maximum dimensions. This would suggest that an inward migration of strain away from the boarder faults may be imminent. Our velocity model shows that $\sim$4.3 km of sediment exists in the accommodation zone between these opposite-polarity border faults, which smoothly shifts from eastward-thickening sediments within the North Basin to the westward-thickening sedimentary section in the Central Basin. This observation matches predictions of analogue

models for overlapping border faults of opposite polarity. The significant thickness of sediment within the accommodation zones indicates that both faults likely reached their lengths early, consistent with the constant-length model of fault growth. Thick packages of preexisting sediment interpreted in both basins are thought to be associated with outcropping Late Paleozoic Karoo and Cretaceous basins onshore. These previously active extensional basins may have influenced the development of the complex structure of the two basins, with the limited extent of prior rifting-related sediment in the North Basin potentially facilitating development of comparatively simple intrabasinal faulting compared to the more complex Central Basin. Finally, we correlate the significant package of preexisting sediment at the northernmost end of the North Basin with Cretaceous and Karoo-age basins that continue NW to the Rukwa Rift system. This observation adds further evidence that the region between the Rukwa and Malawi Rifts has been a corridor of extension for a significant period of time.

Acknowledgements

The authors gratefully acknowledge all of those involved in the successful acquisition of this large and complex experiment. Acquisition of this dataset would not have been possible without the support from communities in our study area, national and regional governmental entities in Malawi and Tanzania, and administrative and technical support from institutes, companies and geological surveys in the United States, Malawi, Tanzania, Denmark, and Canada. We gratefully acknowledge the captains and crews of the Katundu, Ndunduma, and Chilembwe and the entire science party that helped to acquire this dataset. Instruments were provided by the Ocean Bottom Seismology Instrumentation Program (OBSIP) from the Scripps Institute of Oceanography (SIO). We particularly acknowledge Jeff Babcock, Ernest Aaron, Mark Gibaud, Martin Ripa and others at the SIO Institutional Instrument Contributor. We gratefully acknowledge Per Trinhammer from Aarhus University and Jack Schelling for their incredible help with seismic source operations. We also thank Jacob

Greenberg for his help with onboard ship operations. We thank Jean-Arthur Olive for useful discussions. Seismic data used in this study is available through the Incorporated Research Institutions for Seismology Data Management Center (http://ds.iris.edu/ds/nodes/dmc/) network code YQ. Data was processed using Seismic Unix maintained by John Stockwell (http://www.cwp.mines.edu/cwpcodes/) and picked using the OpendTect (https://www.opendtect.org/). This research was supported by National Science Foundation (NSF) grant EAR-1110921, Lamont-Doherty Earth Observatory and the NSF Graduate Student Research Fellowship Program.

4 | Crust and upper mantle shear velocity structure beneath the weakly-extended Malawi Rift with comparison to the mature Main Ethiopian Rift

Abstract To investigate the controls on continental rifting in the southernmost sector of the East Africa Rift System, we conduct shear velocity (Vs) imaging of the crust and uppermost mantle beneath the weakly-extended Northern Malawi Rift. We use previously obtained local-scale measurements of Rayleigh wave phase velocities between 9 and 100 s combined with recently acquired constraints on basin structure and crustal thickness to robustly invert for shear velocity from the surface to 135 km for the Malawi Rift. We compare our resulting 3-D model to a 3-D model of shear velocity obtained for the mature Main Ethiopian Rift and Afar Depression using commensurate datasets and identical methodologies. Comparing the Vs models for the two regions reveals markedly different seismic velocities particularly pronounced in the upper mantle (average velocities in the Malawi Rift are 9% faster than the Main Ethiopian Rift). Our resulting 3-D model of the Malawi Rift reveals a strong, localized low velocity anomaly associated with the Rungwe Volcanic Province within the crust and upper mantle, which can be explained with modestly elevated temperatures and without the presence of partial melt. Away from the RVP, velocities within the plateau regions are fast (>4.6 km/s) and representative of depleted lithospheric mantle to depths of 100 and >135 km to the west and east of the rift, respectively. Thinned lithosphere, represented by the absence of similarly high velocities, is centered directly beneath the footwall escarpments of the rift basins. The correlation between the localization of lithospheric thinning, the boundaries

between abutting Proterozoic mobile belts, and the positions of the basin-bounding border faults may point to the controlling role of preexisting large-scale structures in localizing strain and allowing extension to occur in the Malawi Rift.

4.1 Introduction

Significant debate surrounds the mechanisms controlling continental extension in the Western Rift of the East African Rift System (EARS) where lithosphere is thick and strong (*Ebinger et al.*, 1999; *Pérez-Gussinyé et al.*, 2009; *Stamps et al.*, 2014; *Weeraratne et al.*, 2003). Given these broad geophysical characteristics, it is difficult to explain rifting given the modest magnitude of available tectonic forces (i.e., slab pull and ridge push) (e.g., *Bott*, 1991; *Forsyth and Uyeda*, 1975). Models to explain early-stage rifting often invoke mechanisms of lithospheric strain localization and strength reduction via magmatic intrusions (*Buck*, 2004, 2006). Diverse geophysical studies of magma-rich rift systems have established a strong context for the influential role of melt products on the evolution of continental rifting (*Bastow and Keir*, 2011; *Buck*, 2006; *Corti et al.*, 2003; *Dugda et al.*, 2005; *Ebinger and Casey*, 2001; *Kendall et al.*, 2005; *Armitage et al.*, 2015). From these studies, significant agreement has been established in pointing to magma-assisted rifting along the Eastern Rift of the EARS. However, equal understanding of the controlling mechanisms in magma-poor rift systems has yet to be found. Studies of the Western Rift have consistently shown that standard estimates of lithospheric strength suggest the lithosphere should be too strong to rupture by tectonic forces alone in the absence of secondary weakening mechanisms (e.g., *O'Donnell et al.*, 2016; *Stamps et al.*, 2014). On the other hand, interpretations of seismic tomography, receiver functions, and azimuthal anisotropy increasingly point to the possibility of passive, amagmatic rifting (e.g., *O'Donnell et al.*, 2016; *Reed et al.*, 2016; *Yu et al.*, 2015). This paradox is not limited to the Western Rift as many ancient and active rift systems display evidence of volumetrically limited magmatic activity, for example the Newfoundland-Iberia rifted margins (e.g., *Van Avendonk et al.*, 2009; *Whitmarsh et al.*, 2000) and the central

basins of the Baikal Rift (e.g., *Rasskazov*, 1994).

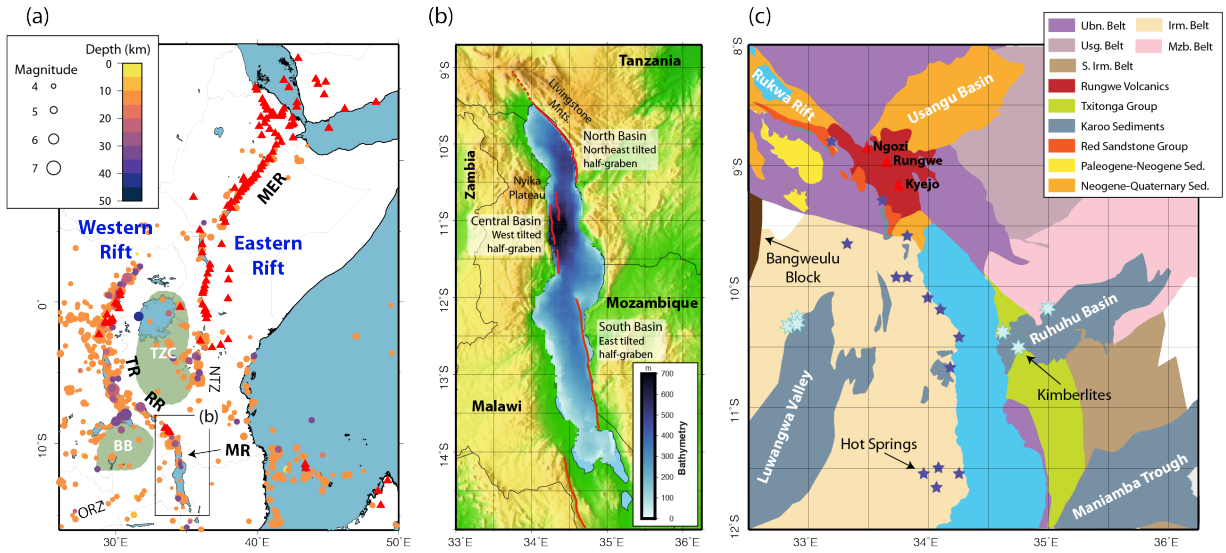

Figure 4.1: (a) Distribution of seismicity (Mw >2.5 since 1970 from the ISC catalog) and Quaternary-recent volcanoes (*Venzke et al.*, 2002) along the East African Rift System; TZC: Tanzanian Craton, BB: Bangweulu Block, MR: Malawi Rift, RR: Rukwa Rift, TR: Tanganyika Rift, NTZ: Northern Tanzania Divergence Zone, ORZ: Okavango Rift Zone, MER: Main Ethiopian Rift. The NTZ represents the southern continuation of the Eastern Rift and the ORZ represents northern continuation of the Southwestern Rift. (b) Topographic and bathymetric map of the Malawi Rift with locations of basin-bounding border faults shown in red. (c) Simplified geologic map of the North and Central basins of the Malawi Rift highlighting the intersecting Proterozoic mobile belts; Ubn: Ubendian, Usg. Usagaran, Irm. Irumide, S. Irm. Southern Irumide, Mzb: Mozambique. Geologic units are mapped after *Bennett* (1989), *Delvaux* (2001), *Pinna et al.* (2004), *Roberts et al.* (2010), *Fritz et al.* (2013), and *Hauzenberger et al.* (2014).

Recent alternative models to explain extension of strong lithosphere focus on the influential effects of processes that localize strain within the lithosphere (e.g., *Regenauer-Lieb et al.*, 2008; *Rosenbaum et al.*, 2010). Mechanisms for strain localization in the lithospheric mantle like shear heating and dynamic grain size reduction have been shown to be particularly effective in colder mantle settings (*Précigout and Gueydan*, 2009; *Regenauer-Lieb et al.*, 2008), like that increasingly suggested for the Western Rift (e.g., *O'Donnell et al.*, 2016; *Reed et al.*, 2016). Strain localization is also proposed to occur as a result of large-scale changes in rheology (i.e., variations in lithospheric thickness)(e.g., *Corti and Manetti*, 2006) or the presence of preexisting weaknesses like tectonic sutures (e.g., *Corti et al.*, 2011). These sug-

gested mechanisms have important implications for the evolution of both crust and mantle lithospheric thinning especially in systems where weakening of the lithosphere by magmatic processes may not be viable.

While magmatism is limited along most of the length of the Western Rift, magmatism does occur in four isolated volcanic centers along the Western Rift system. Local- to regional-scale tomographic imaging has shown that the four volcanic centers are underlain by low velocity zones limited to the lithosphere and shallow asthenosphere (*O'Donnell et al.*, 2013; *Accardo et al.*, 2017; *Jakovlev et al.*, 2013). Several mechanisms exist to explain the source of these volcanic centers. Many authors highlight the correlation between volcanic center locations, locations of large-scale accommodation zones between adjacent rift segments, and boundaries between abutting Archean cratons (e.g., *Ebinger and Sleep*, 1998; *King and Ritsema*, 2000; *Koptev et al.*, 2015). Large gradients in the topography of the lithosphere-asthenosphere boundary (LAB) can play a controlling role in guiding mantle flow in regions where significant changes in lithospheric thickness occur like passive margins (e.g., *King and Anderson*, 1995; *Shillington et al.*, 2009; *Ramsay and Pysklywec*, 2011) and the boundaries of cratons (e.g., *Koptev et al.*, 2015; *van Wijk et al.*, 2008). In the case of East Africa, several authors invoke the influence of either a solitary mantle plume (e.g., *Ebinger and Sleep*, 1998) or multiple mantle plumes (e.g., *Chang and Van der Lee*, 2011) in providing forces to guide mantle flow along these gradients in LAB topography. In these models, locations of thinner lithosphere allow decompression melting of the asthenosphere leading to the development of the volcanic centers.

The presence of a mantle plume beneath the Western Rift has long been debated (e.g., *Hansen et al.*, 2012), with seismic tomography imaging consistently showing a lack of large-scale slow velocities in the upper mantle like those observed beneath the Eastern Rift (e.g., *Adams et al.*, 2012; *Ritsema and van Heijst*, 2000). However, recent studies have found elevated $^{3}He/^{4}He$ pointing to a plume source in lavas and hot springs associated with the Rungwe Volcanic Province (RVP) (*Barry et al.*, 2013; *Hilton et al.*, 2011; *Wanless et al.*,

2016), the southernmost location of volcanism for the entire rift system. Intriguingly, in this area, regional body wave imaging suggests the African Superplume (e.g., *Nyblade et al.*, 2000) is restricted to the lower mantle (*Grijalva*, 2017) in agreement with observations of an unperturbed mantle transition zone from receiver function imaging (*Reed et al.*, 2016). Deeper imaging along the Western Rift will provide important insight into the state of the upper mantle beneath these isolated volcanic centers and magma-poor rift segments and, critically, what the origin and role of magmatic products are within these systems.

In this work, we first present shear velocity imaging of the upper mantle beneath the Malawi Rift, a characteristic Western Rift system, to elucidate the nature of upper mantle velocity structure. We compare these results to shear velocity images (constructed using identical analysis methods) of the mature, magma-rich Main Ethiopian Rift (MER) and Afar Depression to investigate the consequences of variations in mechanisms of continental rifting on seismic observables. Combined, this work presents a unique opportunity to examine controls on continental rifting in two classic end-member systems.

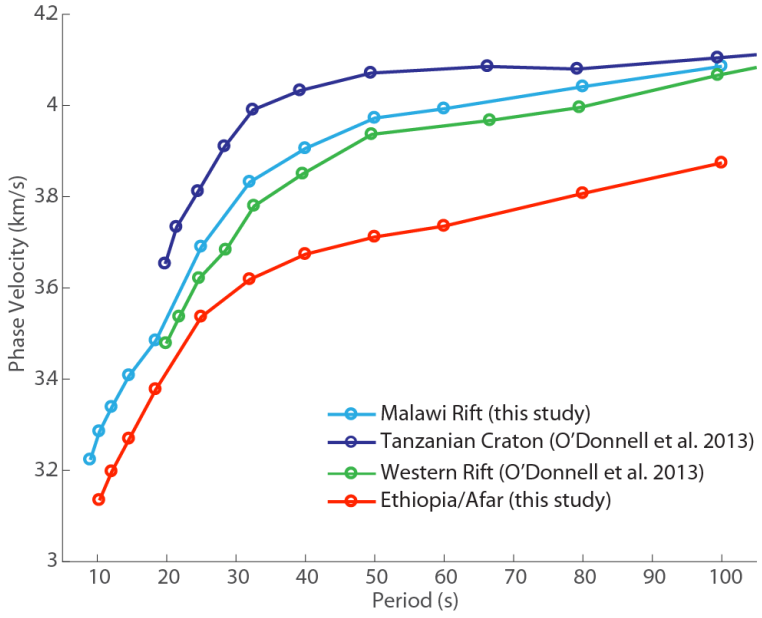

Figure 4.2: Comparison of average dispersion curves from this study (Malawi Rift - blue; Ethiopia/Afar - red) and averages from comparable locations from *O'Donnell et al.* (2013).

4.2 Tectonic Setting

We focus here on two rift systems of the Western and Eastern Rifts of the Cenozoic EARS; the Malawi Rift and the MER and Afar Depression, respectively. The Archean Tanzanian Craton (TZC) forms the core of the tectonic framework of East Africa and demarcates the Western Rift to the west and south and the Eastern Rift to the north and east (Fig. 4.1a) (e.g., *Chorowicz*, 2005). Differences in the distribution of seismicity and volcanism between the two rifts (Fig. 4.1a) are thought to represent fundamental differences in how extension is accommodated (e.g., *Craig et al.*, 2011; *O'Donnell et al.*, 2016), at least at shallow levels (*Keir et al.*, 2009). Debate continues concerning the southern extent of the Eastern Rift as well as the localization of a third major EARS rift, the Southwestern Rift (for a review see *Chorowicz*, 2005). The Malawi Rift is thought to sit at the juncture between the Western Rift and the southern Eastern Rift as well as between the Western Rift and the northern Southwestern Rift. This intersection is evidenced by diffuse seismicity trending to the northeast and into the Eastern Rift and to the southwest into the Southwestern Rift (e.g., *Craig et al.*, 2011; *Mulibo and Nyblade*, 2016; *Le Gall et al.*, 2008; *Modisi et al.*, 2000).

4.2.1 The Malawi Rift

The Malawi Rift is an ∼800-km-long rift that represents the southernmost segment of the Western Rift. The Malawi Rift sits at the juncture of major boundaries between adjacent Proterozoic mobile belts, cratonic blocks (TZC, Bangweulu Block, Niassa Craton) (e.g., *Begg et al.*, 2009; *Fritz et al.*, 2009; *Sarafian et al.*, 2018), and separate rift branches of the EARS. Common to other Western Rift systems, the Malawi Rift is characterized by strong lithosphere with active and deep crustal seismicity (*Craig et al.*, 2011; *Ebinger*, 1989b; *Fagereng*, 2013; *Jackson and Blenkinsop*, 1993b), limited surface volcanism (*Furman*, 2007), and asymmetric border-fault-bounded half grabens with polarities that vary along the rift (*Scholz*, 1989). Lake Malawi (Nyasa) covers approximately 550 km of the rift axis, and is a

type example of a narrow and deep East African rift lake.

At shallow depths, the Malawi Rift is expressed as a series of three >100 km long basins (North, Central, and South) that are bounded by border faults and linked by low relief accommodation zones (*Scholz*, 1989). Modest extension is thought to have occurred in this system with crustal stretching estimates from flexural models of basin and flank morphology and fault reconstructions suggesting <20% (*Ebinger et al.*, 1987) and estimates from sparse GPS data indicating plate-opening velocity of ca. 2 mm/yr (*Saria et al.*, 2014). Significant packages of sediment occur within both the North and Central basins (at least 5 km of Neogene-recent sediment; Chapter 3) associated with significant offset of the basin-bounding border faults. Border faults are long but poorly developed in the southern segment of the Malawi Rift potentially related to the presence of significantly thicker lithosphere and/or diminishing magnitudes of extension (*Lao-Davila et al.*, 2015; *Reed et al.*, 2016).

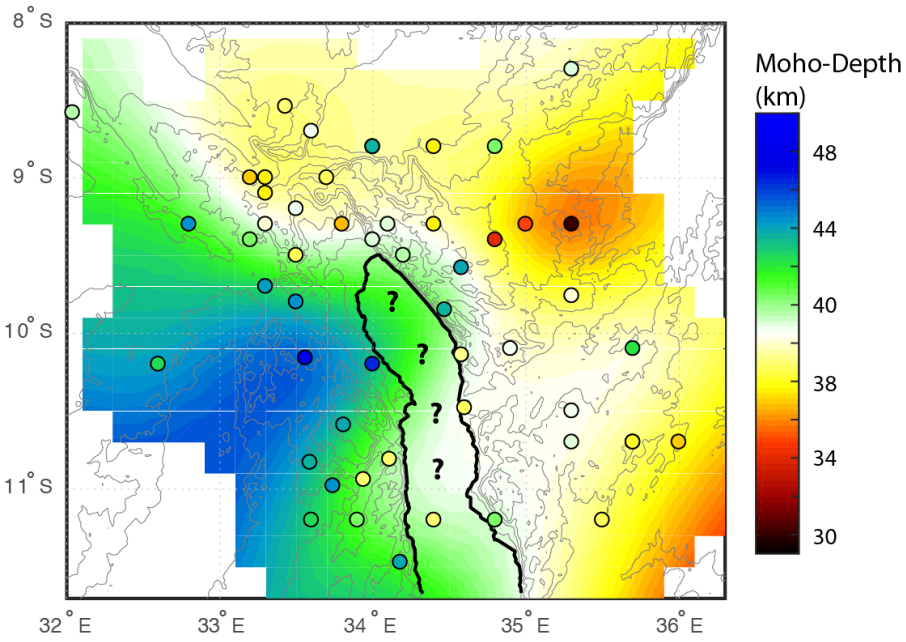

Figure 4.3: Map of crustal thickness beneath the Malawi Rift from *Hodgson et al.* (2017), *Hopper et al.* (2017), *Borrego et al.* (2015). Background surface represents the fit to individual estimates of Moho-depth (circles). Question marks are placed beneath Lake Malawi owing to the lack of constraints there.

Figure 4.1c provides an overview of the onshore geology of the North and Central basins

of the Malawi Rift. These two basins developed within abutting Proterozoic mobile belts formed during major orogenies. The North Basin overlies the juncture between the Irumide Belt (∼1350-950 Ma) to the west and the Ubendian (∼ 2300-1800 Ma) and Mozambique belts (Pan African Orogeny, ∼900-450 Ma) to the east (e.g., *Begg et al.*, 2009; *Chorowicz*, 2005). The Irumide Belt continues south along the western lakeshore of the Central Basin. East of the Central Basin, a narrow zone of the Ubendian Belt outcrops, followed east of that by the Neoproterozoic Txitonga Group, and farther east by the Mesoproterozoic Southern Irumide Belt (e.g., *Fritz et al.*, 2013; *Hauzenberger et al.*, 2014). Poor exposures and difficult access to the region close to the Mozambique border have hampered complete understanding of basement geology until very recently (*Hauzenberger et al.*, 2014). Fault-bounded depressions to the west and east of the Central Basin striking approximately SW-NE (Luangwa Valley and Ruhuhu Basin, respectively) represent Karoo rift basins (e.g., *Catuneanu et al.*, 2005) formed in the Late Paleozoic associated with early Gondwana breakup (*Wopfner*, 1994, 2002) that appear to continue beneath the lake (Chapter 3, *Accardo et al.*, in review).

The RVP at the northern end of the Malawi Rift is one of four volcanic centers within the Western Rift of the EARS (*Furman*, 2007). The RVP sits at the juncture between the Archean TZC to the north and the Archean-Paleoproterozoic Bangwelu Block to the west (e.g., *De Waele et al.*, 2006). Regionally, the RVP also marks the location of the complex accommodation zone between the Malawi, Rukwa, and apparently inactive Usangu rifts. Three volcanoes occur within the RVP and have erupted in the past 10 Ka (*Ebinger et al.*, 1989; *Fontijn et al.*, 2010b,a, 2012). Active magma reservoirs are thought to be present beneath at least two of the volcanoes (*Fontijn et al.*, 2012). The relative timing of the onset of rifting within the Rukwa-Malawi rift zones is still debated due to the lack of deep drill data. Magmatism in the RVP may have commenced as early as 25 Ma (*Roberts et al.*, 2012). The onset of extension and faulting is not constrained, but some authors estimate 8.6 Ma along the northern basin bounding fault, which would be much later than the onset of magmatism (for a review see *Ebinger and Scholz*, 2012). Thermobarometry of mafic melts point to a

shallow depth of melting beneath the RVP (<110 km) and ambient to moderately elevated mantle potential temperatures (Tp ∼1275 - 1400°C)(*Mesko et al.*, in prep).

Recent results from SEGMeNT (Study of Extension and maGmatism in Malawi aNd Tanzania)(*Shillington et al.*, 2016) have provided high-resolution seismic constraints on basin- to mantle-scale structure and geochemistry (*Accardo et al.*, 2017; *Grijalva*, 2017; *Borrego et al.*, 2015; *Tepp*, 2016; *Mesko et al.*, in prep). Recent imaging studies refine previous regional-scale studies using surface and body waves that image a circular low-velocity region centered on the RVP within the uppermost mantle associated with complex mantle anisotropy (*Adams et al.*, 2012; *Grijalva*, 2017; *Mulibo and Nyblade*, 2013; *Tepp*, 2016; *O'Donnell et al.*, 2013). The shear-wave splitting study of *Tepp* (2016) observes a dominant NE-SW directed pattern of anisotropy throughout the study region except beneath the RVP where the observed anisotropy is reduced in magnitude and reported fast directions vary greatly. They suggest this pattern reflects anisotropy dominantly within the asthenosphere and increased complexity beneath the RVP reflects a perturbation in mantle flow related to dynamics beneath the volcanic center. *Borrego et al.* (2015) conducted receiver function analysis and found that Moho depth is relatively constant across the study region with no indication of a large-scale shallowing of the Moho surrounding Lake Malawi.

4.2.2 The Main Ethiopian Rift and Afar Depression

The MER and Afar Depression in the northernmost part of the EARS represent a type example of a mature, magma-rich rift (see Figure C.1). The present day Afar Depression marks the rift-rift-rift triple junction between the Red Sea, Gulf of Aden, and MER (e.g., *Stern*, 1994). Volcanism likely preceded extension in the area with a widespread volcanic activity occurring in southern Ethiopia and northern Kenya from 45-30 Ma (e.g., *Ebinger et al.*, 1993a; *George et al.*, 1998; *Furman et al.*, 2006). Extensive flood basalt volcanism commencing between 35-30 Ma (*Baker et al.*, 1996; *Furman et al.*, 2006) marked the impingement of the Afar plume head on the Arabian-Nubian shield (*Pik et al.*, 1999; *Kieffer*

et al., 2004). Rifting first began in the study region along the western Afar margin at ∼ 29-31 Ma (*Ayalew et al.*, 2006; *Wolfenden et al.*, 2005). Within the MER the earliest faulting episodes occurred in southwest Ethiopia by ∼ 18 Ma (*Ebinger et al.*, 2000) and in the central and northern MER by ∼ 11 Ma (*Wolfenden et al.*, 2004; *WoldeGabriel et al.*, 1999).

Table 4.1: Allowed perturbations to the starting models for the shear velocity inversion.

Parameter	**Allowed perturbation**
Sediment Velocity	±10%
Crustal Velocity	±10%
Mantle Velocity	±10%
Sediment Thickness	±1 km
Moho Depth	±5 km

Significant study of the MER and Afar Depression over the last 15 years reveal a broad low-velocity zone within the upper mantle that underlies the rift valley and much of the rift flanks, hypothesized to be a continuation of the African Superplume (*Bastow et al.*, 2008; *Benoit et al.*, 2006) though a connection to low upper mantle velocities beneath the Afar Depression is debated (*Hansen and Nyblade*, 2013). At shallower depths, rift structure is imaged to be asymmetric in the crust (e.g., *Maguire et al.*, 2006; *Stuart et al.*, 2006) and uppermost mantle with the Ethiopian plateau being characterized by highly electrically conductive, thickened crust compared to the rift valley floor and Somalian plateau (*Keranen et al.*, 2004; *Whaler and Hautot*, 2006). Several authors have pointed to role of a Proterozoic aged suture that parallels part of the rift axis in controlling the narrow expression of the rift at crustal depths (e.g., *Berhe*, 1990; *Keranen and Klemperer*, 2008; *Stern et al.*, 1990). Robust evidence exists for the presence of melt within the crust and upper mantle beneath both the MER and Afar Depression from active- and passive-source seismic studies (e.g., *Dugda et al.*, 2005; *Gallacher et al.*, 2016; *Rychert et al.*, 2012; *Stuart et al.*, 2006), petrogenic modeling (*Ferguson et al.*, 2013; *Rooney et al.*, 2011), and magnetotelluric studies

(*Whaler and Hautot*, 2006).

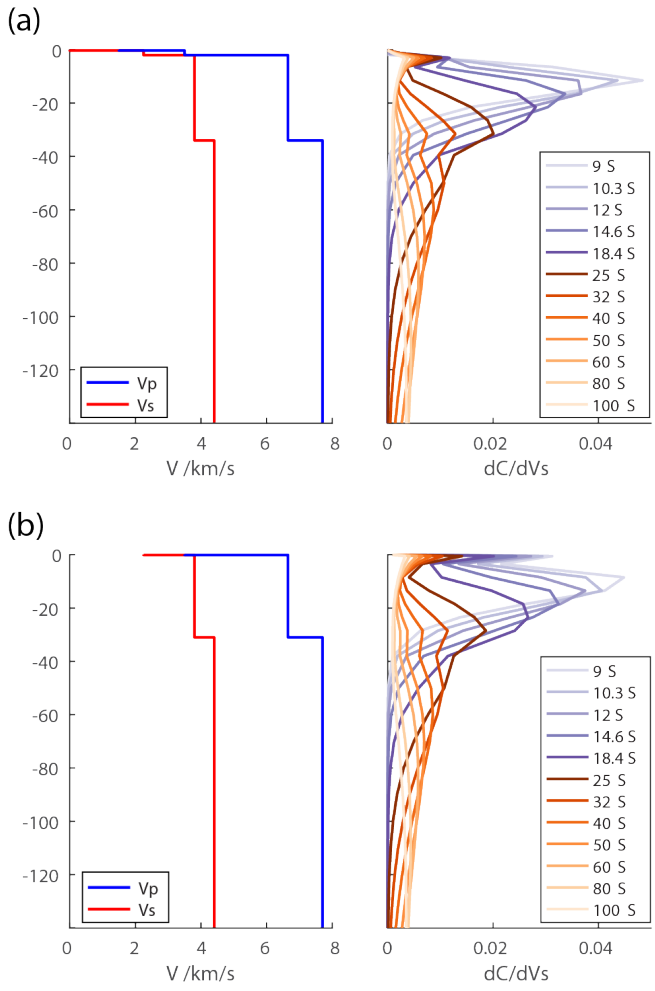

Figure 4.4: Sensitivity kernels of Rayleigh waves between 9 and 100 s for (a) models with a water layer and (b) models without a water layer.

4.3 Data and Methods

4.3.1 Rayleigh Wave Phase Velocities for Malawi Rift

We use the ambient-noise (9 - 20 s) and teleseismic (25 - 100 s) Rayleigh wave phase velocity dataset of *Accardo et al.* (2017). This dataset utilized both onshore and lake-bottom instruments from the SEGMeNT array, the TANGA array, and three Africa Array stations (a total of 72 intermediate and broadband stations). Average station spacing was ∼40 km for the SEGMeNT array and <20 km for the TANGA array (see Fig.1.1). Teleseismic Rayleigh

wave phase velocities were measured using the Automated Surface-Wave Measuring System of *Jin and Gaherty* (2015), which leverages the coherency in surface-wave trains recorded on nearby stations to robustly determine phase and amplitude information. Phase velocity from ambient-noise derived Rayleigh waves were determined using the frequency domain cross-spectrum method of *Menke and Jin* (2015). Resulting maps of phase velocity had a grid spacing of 0.2°(∼22 km). Overall, phase velocities are slightly above average compared to previous studies of the Western Rift but do not reach the fast phase velocities representative of the Archean TZC (Fig. 4.2). Preliminary analysis of anisotropy by *Accardo et al.* (2017) found that inclusion of azimuthal anisotropy had little influence on patterns of phase velocity for the region.

4.3.2 Shear Velocity Inversion for Malawi Rift

To invert for shear velocity, we follow the generalized procedure utilized in *Jin et al.* (2015). This procedure uses the surf96 program (*Herrmann*, 2013) to invert dispersion curves retrieved from maps of phase velocity at each grid point for models of 1-D shear velocity. This is a linearized least squares inversion method that implements differential damping to enforce smoothness by seeking to minimize the differences in model changes within each individual layer. To minimize biases resulting from choices in the starting model and allow direct access to estimates of model uncertainty, we invert a family of starting models for each grid point. Starting models consist of sediment, crust, and mantle layers that are each themselves composed of 1-, 6-, and 10-km-thick layers, respectively. We leverage *a priori* information on shallow structure (water depth in Lake Malawi and sediment and crustal thickness) from seismic reflection (*Lyons et al.*, 2011), wide-angle refraction (Chapter 3), and receiver function studies (*Hopper et al.*, 2017; *Borrego et al.*, 2015) to guide the construction of initial models for each location. Figure 4.3 shows a map of crustal thickness used for this study. We introduce Gaussian distributed perturbations to individual layer velocities and velocity boundaries (sediment/crust and crust/mantle boundaries) through a Monte Carlo approach to create 100 unique starting models. Unlike *Jin et al.* (2015), we

allow variations in individual layer velocities within the crust and mantle to provide a more

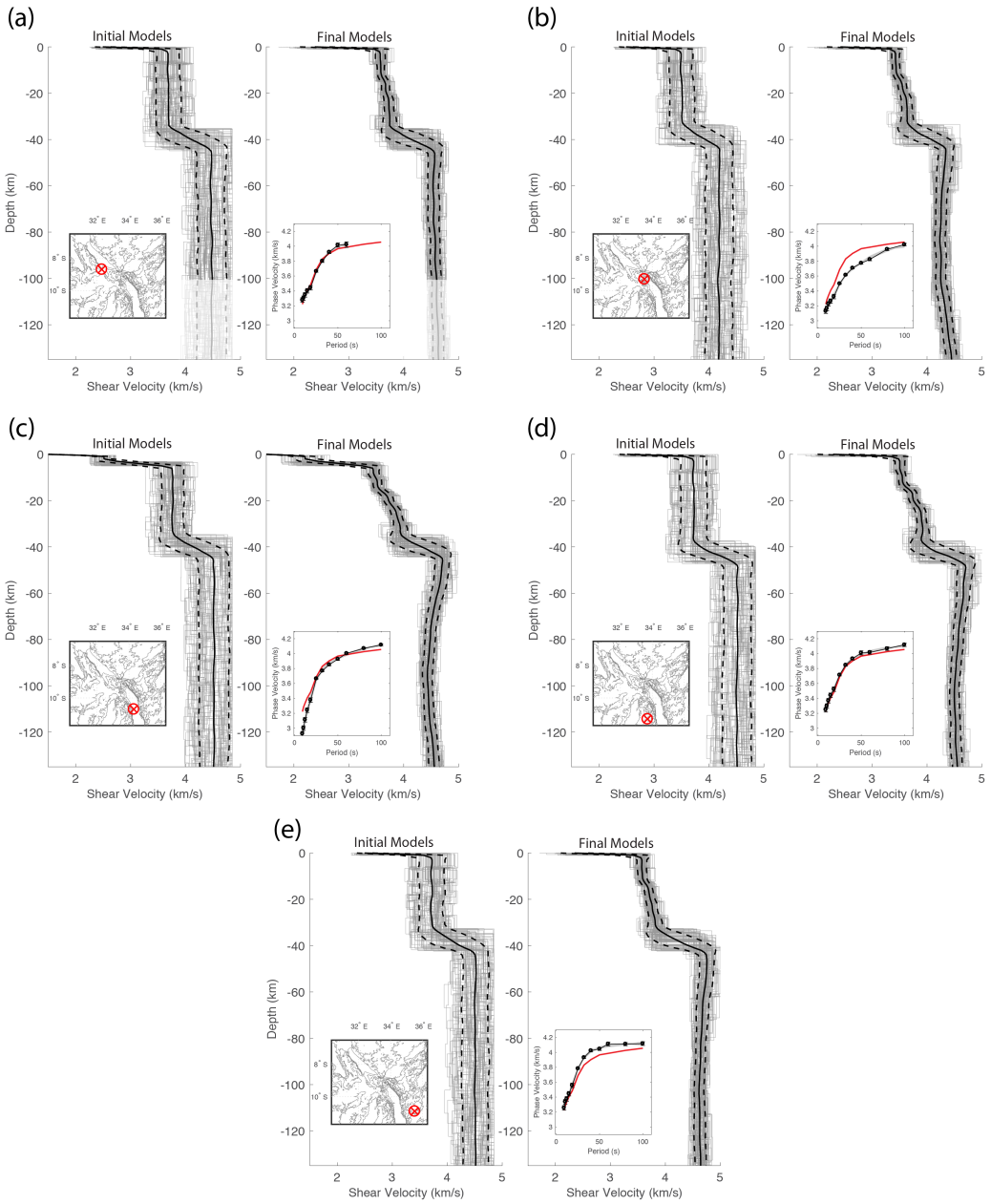

Figure 4.5: Examples of 1-D shear velocity inversions at several locations. The left panel of each subplot shows the suite of initial models with an inset plot showing the location of the profile within the study region. The right panel shows the suite of final models and the inset plot shows a comparison between the suite of predicted phase velocity dispersion curves (grey), observed phase velocities (black), and the mean dispersion curve for the study region (red). The average and standard deviations of the initial/final models are shown by the thick black lines. Note that locations NW of the RVP like in (a) only have phase velocity measurements out to 60 s.

varied family of starting models. Table 4.1 details the allowed perturbations to the parameters of interest. Models extend to 400 km depth but are constrained towards iasp91 below 225 km. We choose 225 km for this depth to minimize this influence on the depth range that we interpret (<135 km).

Figure 4.4 shows the predicted sensitivity kernels for phase velocities from 9-100 s with and without the influence of a lake layer. In the inversion step, physical dispersion is accounted for using a Q model that smoothly transitions from a low attenuation lithosphere (Q = 180) above 120 km depth to a moderately attenuating asthenosphere (Q=80). Ignoring for the effect of physical dispersion would result in shear velocities that are 0.7% slower than our model in asthenospheric regions. After inverting the family of starting models, we discard models with the largest misfits (>20% above the average misfit). The final model is then taken as the mean of the remaining models, and fits to the observed dispersion curves are estimated after forward modeling the final model. Figure 4.5 shows an example for several locations in our model, showing the suite of starting models and resulting models and forward modeled dispersion curves. We construct our final 3-D model by combining the 1-D shear velocity models from all grid points.

4.3.3 Analysis of the Main Ethiopian Rift and Afar Depression

Full details of the datasets and methods used to construct maps of phase velocity for the MER and Afar Depression are given in Appendix C and briefly reviewed here. Vertical component traces from 107 stations deployed within the MER and Afar Depression from both permanent (i.e., Global Seismographic Network) and temporary arrays were obtained to measure Rayleigh wave phase velocities between 9 and 100 s following the same procedure implemented in *Accardo et al.* (2017). Station spacing varied for the different temporary deployments but on average was ∼50 km. Maps of phase velocity for ambient noise and teleseismic Rayleigh waves were constructed using grid sizes of 0.25° and 0.5°, respectively.

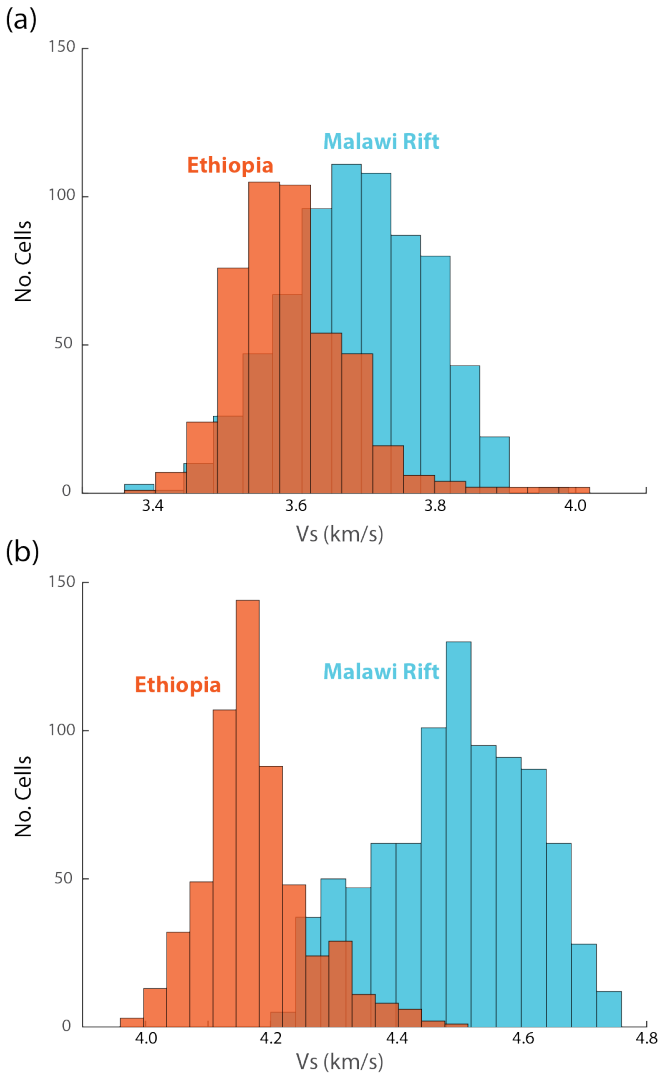

Figure 4.6: Comparison of crustal velocities (10-25 km; a) and mantle velocities (70-110 km; b) between the study region in Ethiopia (orange colors) and the Malawi Rift (blue colors).

The same inversion procedure for shear velocity detailed above was used to invert the maps of phase velocity from the Ethiopia study region. Prior information on sediment thickness and Moho-depth were obtained from active- and passive-source studies to constrain families of starting models for each grid point within the array (*Dugda et al.*, 2005; *Hammond et al.*, 2011; *Stuart et al.*, 2006; *Keranen and Horne*, 2014).

4.4 Results and Velocity Interpretation

Figure 4.6 shows a comparison of crust (10-25 km) and upper mantle (70-110 km) shear velocities beneath the MER and Afar Depression and the Malawi Rift. The Ethiopian study

region is consistently slower than the Malawi Rift; however, this difference is most pronounced in the upper mantle compared to the crust. In the upper mantle, nearly the entire Ethiopian study region is characterized by velocities <4.3 km/s. The markedly slow character of the Ethiopian upper mantle is interpreted to represent the large-scale thermo-chemical modification and thinning of the lithosphere there (e.g., *Dugda et al.*, 2007; *Gallacher et al.*, 2016). In contrast, the upper mantle beneath the Malawi Rift is >4.2 km/s.

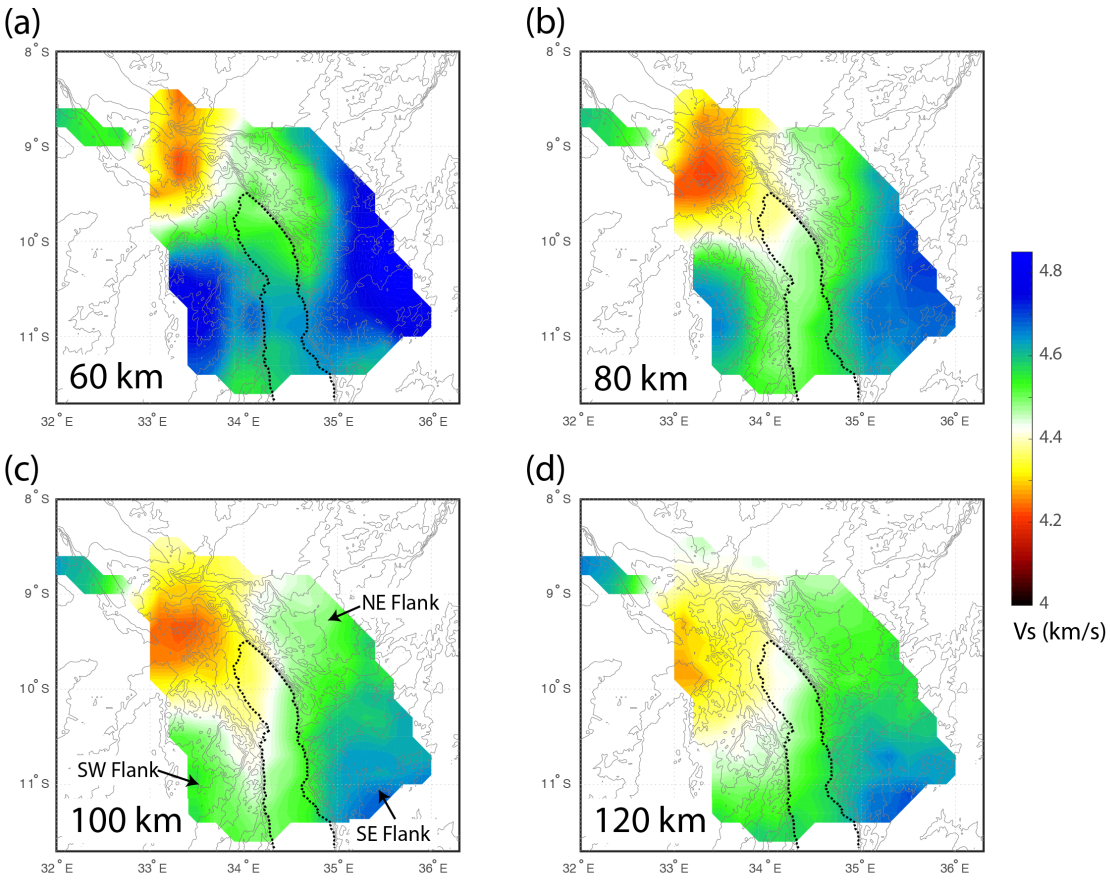

Figure 4.7: Final Vs model at depths between 60 - 120 km. Grey lines show topography and the dashed black line represents the shoreline of Lake Malawi.

Figures 4.7 and 4.8 show depth and cross-section slices through our final shear velocity model for the Malawi Rift. Because we use phase velocity measurements between 9 and 100 s, structures shallower than 10 km and deeper than 135 km are not well constrained. Additionally, we do not interpret variations in Moho depth beneath the lake owing to a present lack of constraints. Our final Vs model provides a 75% variance reduction to the fit

of the phase velocity observations compared to a mean Vs model for the region. We can assess model uncertainty from the estimated standard deviations resulting from the family of final models produced at each grid point. Standard deviations are low in the crust (<0.075 km/s) and higher in the mantle (<0.1 km/s). Standard deviations are highest in the depth ranges of the sediment-crust and crust-mantle interfaces likely owing to the limited ability of surface waves to constrain sharp jumps in velocity structure. Our results are largely consistent with the shear velocity model of *O'Donnell et al.* (2013), though the model presented here exhibits more lateral variation related to the increased resolution of this model. Below we discuss several of the primary observations resulting from our velocity model of the Malawi Rift.

4.4.1 Rungwe Volcanic Province

Low velocities are clearly observed beneath the RVP at crust and upper-mantle depths. Within the mantle, a minimum velocity of ∼4.25 km/s occurs in this anomaly at ∼ 80 km depth, though pronounced low velocities (<4.3 km/s) extend from the Moho to at least ∼ 135 km. Previous studies have imaged the velocity anomaly associated with the RVP from surface waves (*O'Donnell et al.*, 2013; *Adams et al.*, 2012) and body waves (*Grijalva*, 2017; *Mulibo and Nyblade*, 2013; *O'Donnell et al.*, 2016) extending to depths of ∼ 120 and >150 km, respectively. Our study images the largest velocity anomaly to be located at relatively shallow upper mantle depths (∼ 80 km) consistent with previous studies and velocities increase to ∼4.4 km/s by 135 km. Our model has limited constraint at 135 km but shows that the velocity anomaly associated with the RVP is reduced in magnitude but still slower than velocities associated with the surrounding lithospheric domains at these depths. This indicates that it likely extends deeper than what we can resolve. The edge of the RVP feature is shown to be extremely sharp in map view and does not continue northwest into the Rukwa Rift where we have phase velocity measurements to periods of 60 s. This result matches very well with the limited spatial extent of reduced anisotropy as mapped by the shear wave splitting study of *Tepp* (2016) (Fig. 4.9), which they associate with complex anisotropy beneath the RVP.

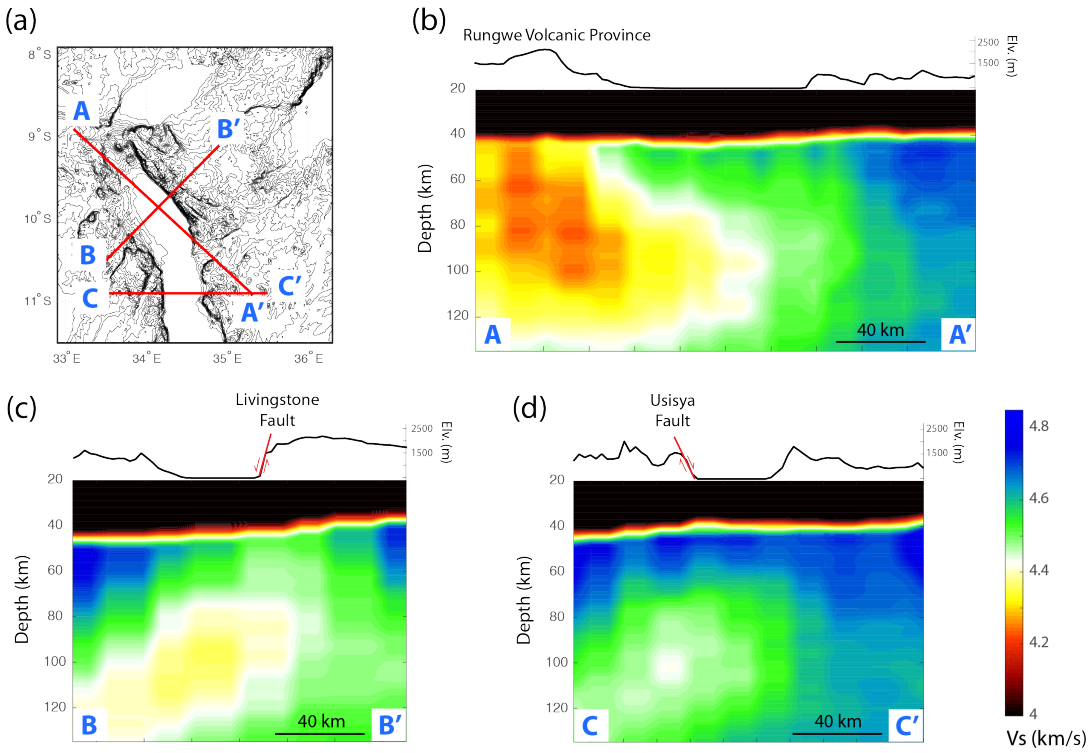

Figure 4.8: 2-D profiles through the final velocity model with topography shown on top. Locations of interest are labeled along with fault motions for the two border faults.

4.4.2 Western and Eastern Rift Flanks

We define the regions outside of Lake Malawi and the RVP as the southwestern flank, the southeastern flank, and the northeastern flank (Fig. 4.7c). Figure 4.10 shows a comparison of average 1-D velocity profiles from these three regions as well as the RVP. Both the southeastern and southwestern plateau regions are defined by relatively fast (Vs >4.6 km/s) from the Moho to depths of $\sim$ 100 km for the southwestern flank and >130 km for the southeastern flank. These relatively high velocities (>4.6 km/s) are most simply interpreted as indicative of mantle lithosphere. The mobile belts that underlie the study region (Irumide, Ubendian, and Southern Irumide) are all thought to be composed of reworked Archean crust (for a review see *Fritz et al.*, 2013) indicating that the lithosphere is likely depleted and hence seismically fast. *O'Donnell et al.* (2013) imaged similar fast velocity structures but at greater distances west and east of the Malawi Rift axis, likely stemming from the lower resolution of that study.

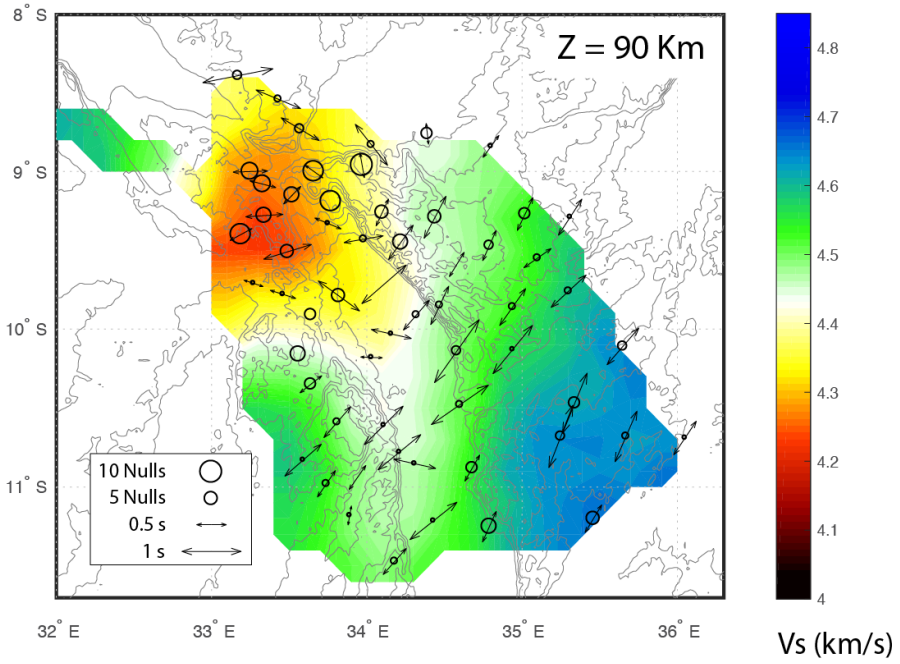

Figure 4.9: Comparison between velocity structure at 90 km from this study and the shear wave splitting results of Tepp (2016). The length of vectors indicate the splitting time and the direction of the vectors indicate the fast direction of anisotropy. Circles indicate locations where null observations of anisotropy were reported and the size of the circle represents the number of null observations.

Several methods exist to estimate the thickness of the seismically-defined mantle lithosphere from tomographic imaging (e.g., *Priestley and McKenzie*, 2006; *van der Lee*, 2002; *Weeraratne et al.*, 2003). Because velocities are high throughout our entire model away from the influence of the RVP, we adopt the method of defining a velocity contour for the base of the lithosphere. This approach best characterizes the structure of southwestern flank, which exhibits a high velocity layer characteristic of mantle lithosphere underlain by a low velocity layer characteristic of the transition to mantle asthenosphere. Following the results of *O'Donnell et al.* (2013), we define the transition between the mantle lithosphere and asthenosphere by the 4.5 km/s contour. Using this as a reference point, we find that the lithosphere beneath the southwestern plateau is ∼100 km thick and the lithosphere beneath the southeastern plateau must be at least 135 km and potentially thicker. This approach is consistent with estimates of lithospheric thickness defined by the depth to the largest

negative gradient (∼85 - 110 km). Testing shows that the depth to the 4.5 km/s velocity contour stays constant when applying perturbations to Moho depth. The observed asymmetry in lithospheric structure between the southern flanks is consistent with the shear velocity models of *O'Donnell et al.* (2013) and *Adams et al.* (2012), both of which exhibit a ∼2% velocity contrast between the southwestern and southeastern flanks to depths >122 km that we would interpret as the same variation in lithospheric thickness that we observe.

The northeastern flank is slower than either of the southern flanks particularly at shallow depths (50-80 km), where velocities are <4.5 km/s. The relatively slow velocities continue to depths of ∼110 km, where it has similar velocities to that of the southwestern plateau. Given that the anomaly is most pronounced at shallow depths, it may be an indication that the imposed Moho-depth is too shallow. However, applying a deeper Moho only slightly reduces the magnitude of this anomaly but does not remove it. A similar anomaly is imaged in the P-wave imaging of (*Grijalva*, 2017) and is also shown as a high conductivity feature in preliminary magnetotelluric imaging (*Bedrosian, personal communication*, 2017).

4.4.3 Malawi Rift Axis

We observe reduced velocities (∼4.45 km/s) beneath the rift axis and the footwall escarpments of both the North and Central basins. In the North Basin, the anomaly is clearly associated with a shallowing of the high velocities characteristic of lithosphere to the west from ∼90 km to <60 km directly beneath the footwall escarpment. In the Central Basin, the anomaly continues beneath the rift axis but extends west beneath the footwall escarpment (Fig. 4.8d). The anomaly in the Central Basin is also associated with a shallowing of the high velocities characteristic of lithosphere from ∼ 100 km beneath the southwestern flank to ∼75 km beneath the footwall escarpment. The anomaly is slowest beneath the axis of the North Basin (minimum Vs <4.4 km/s) and reduces in strength (increases in velocity) within the Central Basin. Similar patterns of reduced velocities are apparent in the body-wave images of *Grijalva* (2017) in which they see the strongest anomaly outside of the RVP centered beneath the lake and extending into the footwall of the North Basin and a more

modest reduction of velocities centered along the western lakeshore in the Central Basin.

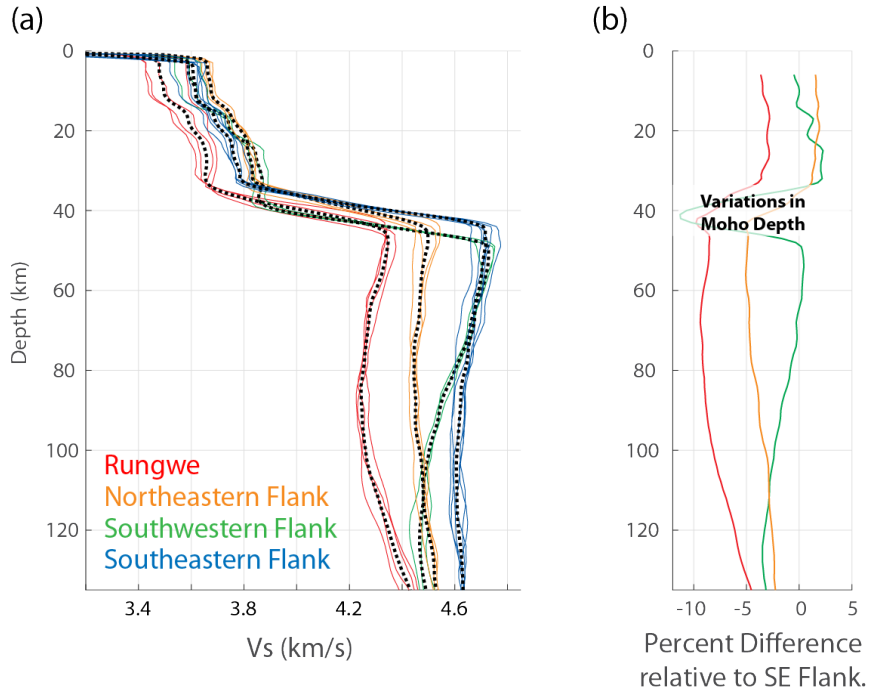

Figure 4.10: (a) Comparison of 1-D average Vs profiles from the four representative regions; Red: Rungwe Volcanic Province, Orange: northeastern flank, Green: southwestern flank, Blue: southeastern flank. The thin lines show 1-D profiles from individual grid points and the thick, dashed lines show the average 1-D profile for a given region. (b) Percent difference between the southwestern flank and the RVP (red), the southwestern flank and the southeastern flank (green), and the southwestern flank and the northeastern flank (orange).

4.4.4 The Main Ethiopian Rift and Afar Depression

In the MER and Afar Depression, we image patterns of shear velocity structure broadly in accord with a diverse range of seismic studies including body-wave imaging (*Bastow et al.*, 2008; *Benoit et al.*, 2006), surface wave studies (*Gallacher et al.*, 2016), regional joint inversion Rayleigh wave and receiver function studies (*Dugda et al.*, 2007; *Keranen et al.*, 2009), and global tomographic models (e.g., *Ritsema and van Heijst*, 2000). Depth slices through the final velocity model are shown in Figure C.9 and a complete description of the shear velocity model for the MER and Afar Depression are given in Appendix C.

4.5 Discussion

4.5.1 Implications for the nature and formation of Rungwe Volcanic Province

The most prominent feature in our velocity model is the low velocity anomaly in the upper mantle and crust associated with the RVP. As introduced in Section 4.2.1, the RVP represents a long-lived volcanic center (*Ebinger et al.*, 1989; *Mesko et al.*, in prep) situated at the intersection of the TZC and the Bangweulu Block. The high-resolution imaging produced by this study represents the first seismological evidence of perturbed crustal velocities associated with the volcanic center. We limit our discussion of this anomaly to average crustal shear velocities owing to strong damping choices placed on the inversion. Importantly, we believe this feature is robust given that errors are low at the period bands most sensitive to crustal structure. We test the influence of adding a thicker sediment layer to models within the RVP region owing to the presence of preserved Cretaceous to Late Paleozoic sedimentary basins outcropping along the western edge of the RVP (Fig. 4.1c) (e.g., *Roberts et al.*, 2010) and find that low crustal velocities are still required. An important question concerns whether this low velocity anomaly requires the presence of melt/fluids within the crust or if it can be explained by a purely thermal origin. Interpretation of crustal velocities in terms of temperature and partial melt is inherently more complex owing to greater heterogeneity in chemical composition compared to the mantle. The relationship between seismic velocity and composition is non-unique further complicating these efforts (*Christensen and Mooney*, 1995). With those complexities in mind, several lines of evidence suggest that some melts and other fluids exist within the crust beneath the RVP. Geophysical studies find high surface heat flow (*Branchu et al.*, 2005) and Bouguer gravity anomalies suggest the presence of low-density magmatic material within crust (*Ebinger et al.*, 1989). Constraints from receiver functions show localized regions of high Vp/Vs ratios (>1.87) in the crust (*Borrego et al.*, 2015), a result commonly interpreted as representing the presence of fluids within the crust (e.g., *Watanabe*, 1993). Geochemical analysis of hot/cold-springs associated with RVP

hydrothermal systems and RVP mafic lava flows indicate variable amounts of crustal contamination potentially controlled by proximity to volcanic edifices (*Crabtree and Chesworth*, 1992).

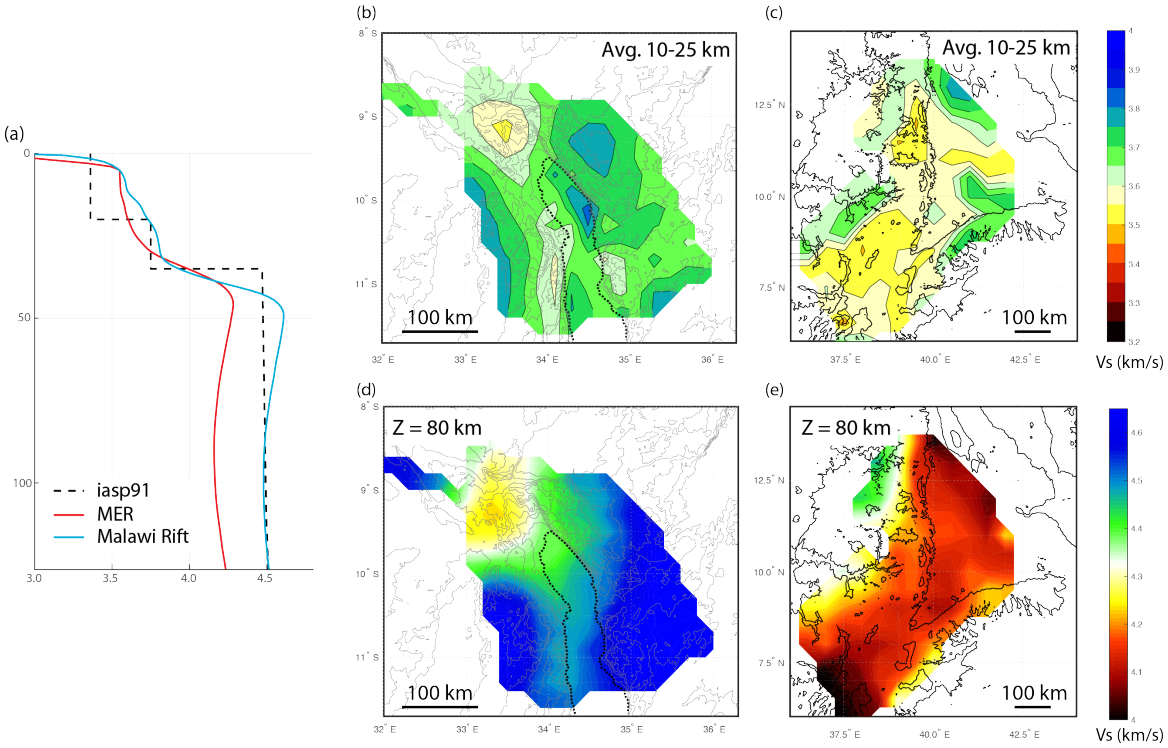

Figure 4.11: Comparison of the shear velocities between the Malawi Rift and the Ethiopian study region. (a) Comparison of average shear velocity profile between the two study regions with a comparison to iasp91, (b,c) comparison of average shear velocities within the crust (10-25 km), (d,e) comparison of shear velocities at 80 km. Maps of shear velocity are shown for the Malawi Rift on the left and the Ethiopian study region on the right. Note that the color scale changes between the top panels and the bottom panels.

When comparing a similar depth average through the crust between the MER and our study region, we find that the MER average crustal velocities are ∼4% slower than our study region overall (Fig. 4.11b,c) This broad-scale difference in average crustal velocities is most easily explained as related to the magma and fluid rich nature of the crust within the MER as is clearly evidenced by numerous active volcanic segments compared to the isolated nature of volcanism in the Malawi Rift (e.g., *Kim et al.*, 2012; *Korostelev et al.*, 2015). However, if we focus on the velocity anomaly associated the RVP, we find that velocities are comparable

to the velocity anomalies associated with volcanically active segments in the MER (∼3.55 km/s). Importantly, even these lowest velocities from both settings are still much faster than those associated with large-scale melt rich bodies (melt percentages >5% and Vs <3 km/s) (e.g., *Delph et al.*, 2017; *Flinders and Shen*, 2017) indicating that this anomaly is not representative of a large, melt rich body. To investigate the temperature anomaly required to explain RVP low velocities within the crust we estimate derivatives of shear velocity and temperature at crustal pressures and a range of compositions (basalt, granite, granulite, and dunite) using the algorithms of *Hacker and Abers* (2004). From this analysis we find that the velocity anomaly observed at the RVP would require a temperature increase of >250°C compared to the surrounding crust (Vs ∼ 3.7 km/s). Additionally, the temperature anomaly required is likely greater than that predicted from our observed velocities given that the presence of solidified mafic melts in the crust would increase seismic velocities rather than decrease seismic velocities. While more detailed and targeted tomographic studies of the crustal structure beneath the RVP are required to directly image any magmatic influence, we suggest the presence of a broad zone of low velocities within the crust is most simply explained by a large thermal anomaly and potentially the added influence of fluids (both magma and hydrothermal systems).

Within the mantle, low velocities (<4.3 km/s) extend to at least 100 km depth beneath the RVP and are the lowest velocities observed for the entire study region. The anomaly is 4 - 9% slower than velocities characterizing the surrounding rift flanks (Fig. 4.10b) indicating a significant perturbation to the system here. However, while the RVP anomaly represents the slowest velocities in the region, it is comparatively fast with respect to the lowest velocities observed in the Ethiopian upper mantle (∼ 4.1 km/s; Fig. 4.11d,e).

Upper mantle seismic velocities are primarily influenced by temperature, partial melt, grain size, and water content (e.g., *Cammarano et al.*, 2003; *Hammond and Humphreys*, 2000; *Karato*, 1993). Significant effort surrounds understanding complex relationships between grain size in the mantle and variations in characteristic parameters (i.e., shear modulus

and attenuation) and the state of the mantle (i.e., temperature and water content) (e.g., *Behn et al.*, 2009; *Faul and Jackson*, 2005). To constrain the thermo-chemical state of the RVP, we compare our measured absolute shear velocities to predictions of upper mantle temperatures and the possible presence of partial melt in the system. To estimate anharmonic and anelastic effects on seismic velocity, we use the extended Burgers model of olivine anelasticity calculated by *Jackson and Faul* (2010). The influence of partial melt on seismic velocity remains debated in the literature with derivatives of seismic velocity versus percent melt content greatly varying (e.g., *Hammond and Humphreys*, 2000; *Hier-Majumder and Courtier*, 2011). We implement the recent parameterization put forward by *Holtzman* (2016) for the anelastic influence of partial melt on shear velocity. This parameterization builds on theoretical and experimental studies, which find that small melt fractions can form connected networks along grain boundaries causing large reductions in shear viscosity. Figure 4.12 shows estimates of velocity versus temperature at a depth of 80 km where we see the slowest velocities within the RVP ($\sim$4.25 km/s). We compare the predictions for the RVP to those for the low velocity anomaly found within the central MER at 80 km depth ($\sim$4.1 km/s).

To first-order we find that we can explain the RVP velocities with a range of mantle temperatures (1250-1350 °C) and grain sizes (1 mm - 5 cm) without requiring the presence of partial melt. If melt is present in the system, it must be limited to very small isolated regions and/or extremely small melt fractions below our limit of resolution. Our interpretation of a purely thermal anomaly beneath the RVP is consistent with other shear velocity imaging studies from different regions where the presence of partial melt is typically invoked to explain seismic velocities <4.2 km/s at these depths (e.g., *Hansen et al.*, 2013; *Rau and Forsyth*, 2011). Further, both shear velocity models from this study for the MER as well as the shear velocity study by *Gallacher et al.* (2016) for the MER require only $\sim$0.6% melt to explain the lowest velocities anomalies in the upper mantle (Vs = 4.1 km/s), indicating that the comparatively fast velocities observed beneath the RVP (Vs = 4.25 km/s) reflect extremely minor, if any, concentrations of partial melt. Lastly, upwelling rates within the

RVP are thought to be the lowest for all the Western Rift volcanic centers based on magma production rates and source depths (*Furman*, 2007; *Mesko et al.*, in prep) indicating that little *in situ* melt may be present within the system at any one time.

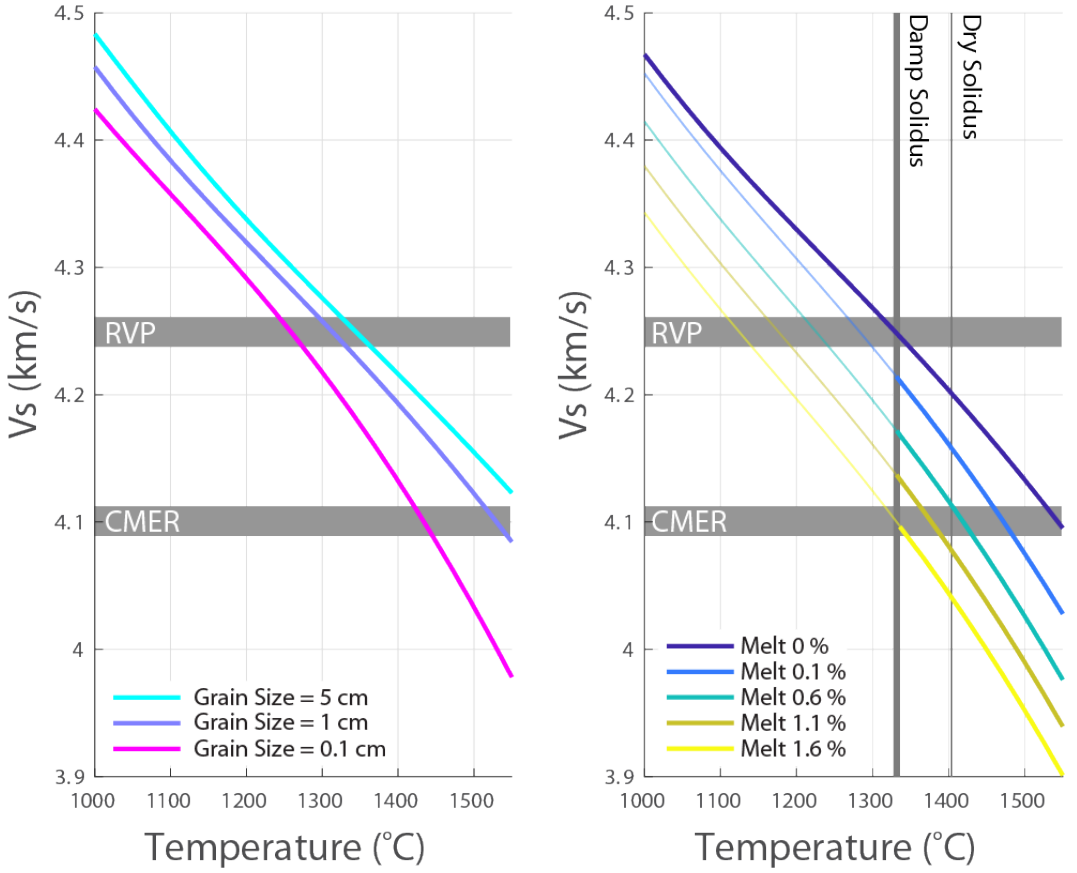

Figure 4.12: Comparisons of predicted shear velocity versus temperature at a depth of 80 km for melt-free olivine at a range of grain sizes using the parameterization of *Jackson and Faul* (2010) (a) and olivine characterized by 1 cm grain sizes and a range of partial melt contents using the parameterization of *Holtzman* (2016) (b). In (b) solidii are shown by the grey vertical lines where the thickest line indicates the solidus assuming 200 ppm H_2O, the medium thick line shows the solidus assuming 100 ppm H_2O, and the thinnest line shows the dry solidus calculated from *Katz et al.* (2003). The observed shear velocities from the RVP and the Central MER (CMER) are shown by the shaded regions.

At this depth range, the dry solidus occurs at temperatures of ∼1405 °C (*Katz et al.*, 2003) placing the RVP temperature anomaly estimated by this study at least 50°C below the dry solidus, consistent with a purely thermal interpretation. The presence of water or other volatiles would act to reduce the solidus, such that the mantle temperatures inferred

from seismic velocity would be closer to the solidus. The presence of volatiles in the East African mantle are thought to be primarily related to past large-scale orogenic events like the Pan-African Orogeny (∼650 Ma) (e.g., *Black and Liegeois*, 1993) and the presence of the seismically observed and geochemically inferred African Superplume (e.g., *Nyblade et al.*, 2000; *Halldorsson et al.*, 2014). Both fault systems and volcanos within the EARS are known to output large volumes of volatiles indicating that volatiles are prevalent at least in parts of the system (e.g., *Frezzotti et al.*, 2010; *Lee et al.*, 2016; *Parsons and Sclater*, 2007). In the RVP, geochemistry of primitive mafic lavas point to a CO_2 rich source (*Furman*, 1995) indicating that a volatile-influenced solidus is likely appropriate here.

The lack of high velocity lithosphere beneath the RVP, like those that characterize the southern flanks, is an indication of pervasive modification of the mantle lithosphere here. Pervasive modification of the lithosphere is consistent with the long-lived nature of the RVP which initiated by 18 Ma (*Rasskazov et al.*, 2003; *Mesko et al.*, 2014). To understand the influence of a heat source at the base of the mantle lithosphere beginning at 18 Ma we can estimate the length-scale of thermal diffusion during that time. We estimate the instantaneous heating of a semi-infinite half-space as

$$\frac{T - T_1}{T_0 - T_1} = erfc\frac{y}{2\sqrt{\kappa t}} \tag{4.1}$$

where y is depth, t is time, κ represents thermal diffusivity and is 32 km^2/m.y., T is the temperature profile, T_1 represents the original temperature, and T_0 represents the new temperature at t = 0 (*Turcotte and Schubert*, 2014). We rearrange this equation to calculate the distance a 250°anomaly would diffuse into the overlying lithosphere over the 18 Ma timescale. We chose 250° for the anomaly given the observation that the temperature anomaly associated with the Iceland hotspot is 200 - 300°(*White et al.*, 1995; *Garrett et al.*, 1996; *Wolfe et al.*, 1997). We find that it would diffuse into <10 km of the overlying lithosphere. This exercise assumes several simplifications including ignoring the temperature gradient within the lithosphere, the subsequent process of thinning the lithosphere, and variations in the

applied thermal anomaly through time. Nevertheless, this simple calculation shows that the reduction in velocities in the lithosphere beneath the RVP cannot simply be ascribed to heating up of the lithosphere by a thermal anomaly but must also represent additional perturbations to the lithosphere.

Numerous mechanisms have been proposed to explain the progressive breakdown of the lithosphere (for a review see *Lee et al.*, 2011), a consequence of which would be a reduction in seismic velocities. Convective removal (i.e., removal of lithosphere due to thermal or chemical buoyancy forces) can promote progressive erosion of the lithosphere and lead to small-scale drips or large-scale delamination of the lithosphere (e.g., *Dave and Li*, 2016; *Xu and Zhao*, 2009). Thermo-chemical modification of the lithosphere may occur via refertilization and subsequent weakening of the base of the lithosphere by infiltrating melts or fluids (*Bialas et al.*, 2010; *Schmeling and Wallner*, 2012; *Havlin et al.*, 2013). These two processes (convective and thermo-chemical) likely interact and result in feedbacks where erosion of the lithosphere by melt infiltration may enhance convective instabilities (e.g., *Fourel et al.*, 2013).

A long-standing question surrounds controls on the marked localization of the Western Rift volcanic centers like the RVP. Indeed, as this study has shown, the RVP anomaly is strongest at shallow upper mantle depths where the diameter of the anomaly is <150 km. The limited spatial extent of this anomaly points to first-order lithospheric controls, specifically, the influence of large variations in lithospheric thicknesses, which can guide mantle flow. Variations in lithospheric thickness have been invoked to explain the presence of intraplate volcanism like the RVP based on abutting Archean-age cratons and blocks in East Africa (e.g., *Ebinger and Sleep*, 1998; *King and Ritsema*, 2000). A range of seismic imaging studies have shown the TZC north of the Malawi Rift is at least 150 km thick (*Fishwick*, 2010; *Weeraratne et al.*, 2003) and potentially thicker (e.g., *Priestley and McKenzie*, 2006; *Wölbern et al.*, 2012). West of the RVP both seismic and recent magnetotelluric imaging have found the Archean-age Bangweulu Block to be even thicker, approaching 200 km

(*O'Donnell et al.*, 2013; *Sarafian et al.*, 2018). The deeply penetrating roots of these cratonic blocks are thought to deflect mantle flow resulting from either background mantle convection or from a rising plume head (e.g., *Koptev et al.*, 2015) and evidenced by large-scale shear wave splitting studies (e.g., *Bagley and Nyblade*, 2013; *Walker et al.*, 2004). *Ebinger and Sleep* (1998) hypothesize that in this context, locations of thinner lithosphere would represent stagnation points where mantle flow can ascend shallowly. A marked rotation in the direction of azimuthal anisotropy reported by *Tepp* (2016) at the junction between the Rukwa Rift (bounded to the northeast by the TZC) and the Malawi Rift further evidences a deflection of flow by the TZC and structurally controlled, complex flow at the RVP (Fig. 4.9). The presence of preexisting thin lithosphere beneath the RVP is also likely owing to the long history of extension along the corridor between the Rukwa and Malawi rifts dating back to the Late Paleozoic (e.g., *Delvaux*, 2001). This is also consistent with the thick package sediments thought to be related to earlier rift episodes observed in the northermost part of the North Basin and discussed in Chapter 3.

Alternative hypotheses to explain the presence of the RVP include the role of edge-driven convection and/or a large-scale connection to the deep seated African Superplume. *King and Ritsema* (2000) invoke the role of edge driven convection to explain intraplate volcanism in East Africa. Our imaging and regional body-wave tomography (*Grijalva*, 2017) suggest that this feature is <150 km in diameter at depths of 100 km, to first-order making it too localized to explain geodynamically by this process. Several authors have pointed to the role of the African Superplume in generating intraplate volcanism within the EARS (e.g., *Hansen et al.*, 2012; *Hilton et al.*, 2011). However, several lines of evidence suggest that a deep seated, hot, plume anomaly is not consistent with the origin of the RVP. The body wave imaging study of *Grijalva* (2017) imaged at least a 300-km separation between the RVP and the African Superplume, imaging of the mantle transition zone further south in the Malawi Rift reveals average transition zone thickness indicating the absence of a large-scale thermal anomaly (*Reed et al.*, 2016), and, lastly, the longer-period (>100 s) surface wave imaging of

O'Donnell et al. (2013) indicate that the RVP velocity anomaly is a relatively shallow upper mantle feature that likely does not extend far past the base of the surrounding lithosphere. Thermobarometry of mafic melts from the RVP suggests ambient to slightly elevated mantle potential temperatures (Tp $\sim$ 1275 - 1400°C)(*Mesko et al.*, in prep). Taken together this suggests that the long-lived nature of the RVP is likely not related to a large-scale thermal perturbation related to ascending hot plume material. The presence of metasomatic phases in RVP lavas like apatite and potentially phlogopite (*Furman*, 1995) point to the potentially influential role of compositional heterogeneities in controlling locations of intraplate volcanism. Based on our imaging, we suggest that the RVP most likely owes its origin to the presence of relatively thinner and volatile rich lithosphere that has allowed the structurally controlled ascent of the asthenosphere and melting of the mantle there.

4.5.2 Variations in lithospheric structure around the Malawi Rift

The lithospheric structure we image in this region can be categorized into three domains as introduced in Section 4.4.2, the southwestern, southeastern, and northeastern flanks (Fig. 4.7c, Fig. 4.10). Our imaging suggests large variations in lithospheric thickness, as well as marked differences in the velocity structure within the lithosphere. The southwestern flank is characterized by mantle lithosphere to $\sim$100 km while the southeastern flank is characterized by mantle lithosphere to depths >135.

Two straightforward explanations exist to explain the variation in lithospheric thickness between the southwestern and southeastern flanks: 1) preexisting thickness variations related to the geology of abutting mobile belts and/or 2) dynamic processes that have thinned the lithosphere within the southwestern flank compared to the southeastern flank related to present-day extension in the Malawi Rift and/or deformation associated with the southern continuation of the Southwestern Rift (e.g., *Modisi et al.*, 2000). Results from southern Malawi and Zambia point to preexisting variations in lithospheric thickness on the order of $\sim$50 km between the Irumide and Southern Irumide belts (*Sarafian et al.*, 2018). In

our region, we image a similar pattern whereby the southwestern flank, associated with the Irumide Belt, is at least 30 km thicker than the lithosphere associated with the Southern Irumide Belt beneath the southeastern flank. In detail, we find that the lithosphere associated with the Irumide Belt is ∼50 km thinner beneath our study region compared to that imaged for the Irumide Belt in southern Zambia by *Sarafian et al.* (2018). The reduction in lithospheric thickness along the Irumide Belt could be a preexisting feature or could be related to thermo-chemical erosion of the lithosphere related to the close proximity of the RVP. For the southeastern flank we can only constrain lithospheric thickness to the maximum depth of our model (135 km), but point out that the only location of kimberlites in the study region occur in the proximity of the southeastern flank (*Gobba*, 1989; *Key et al.*, 2007; *Stiefenhofer and Farrow*, 2004). While, the mechanism controlling their detailed distributions is still debated (e.g., *Bell et al.*, 2003), the presence of kimberlites is commonly considered an indication of thick lithosphere given the temperature-pressure requirements for their formation as well as their association with Archean cratons (e.g., *Artemieva and Mooney*, 2001; *Clifford*, 1966; *Boyd et al.*, 1985). From our imaging it is clear that significant variation in lithospheric thicknesses occur between the mobile belts that form the Malawi Rift with the juncture of that variation occurring beneath Lake Malawi.

While variations in lithospheric thickness can explain the velocity contrast between the southwestern and southeastern flanks at depth, a different explanation is required for the variation in average lithospheric velocity shallowly between the southern flanks and the northeastern flank. The northeastern flank is as much as 5% slower than the southern flanks to depths of ∼80 km (Fig. 4.10). As introduced in Section 4.4.2, the northeastern flank is anomalous compared to the rest of the study region in several ways including having the thinnest crust in the study region (<34 km, Fig. 4.3)(*Borrego et al.*, 2015), distributed high topography (>2200 m), and high conductivity as imaged by preliminary magnetotelluric imaging (*Bedrosian, personal communication*, 2017). Taken together these factors suggest thermo-chemical modification of the northeastern flank. The reason for this modification

could be due to its proximity to the RVP or related to its location within the region of diffuse deformation between the Eastern and Western Rifts (*Le Gall et al.*, 2008; *Mulibo and Nyblade*, 2016)

4.5.3 Low velocities within the upper mantle along the Malawi Rift

As introduced in Section 4.4.3, our shear velocity model reveals a region of reduced velocities (∼4.4 km/s) that are centered beneath the rift axis and beneath the respective footwalls of the North and Central basins (Fig. 4.8b,c). The anomaly is slowest in the North Basin and reduces in strength (increases in velocity in the Central Basin). To first order, we suggest this anomaly represents deformation and early-stage thinning of the mantle lithosphere as a result of present-day rifting processes.

The process of rifting a continent will ultimately manifest itself in thinning of the crust and mantle lithosphere. Along the magma-rich Eastern Rift, crust and mantle lithospheric thinning has been inferred in the Ethiopian Rift (e.g., *Dugda et al.*, 2007, 2005; *Gallacher et al.*, 2016; *Stuart et al.*, 2006) and the Kenya Rift (*Plasman et al.*, 2017; *Sippel et al.*, 2017). Fewer observations exist along the Western Rift where lithospheric blocks are thought to be thicker and stronger (e.g., *Ebinger et al.*, 1999; *Pérez-Gussinyé et al.*, 2009), though *Wölbern et al.* (2012) imaged lithospheric thinning adjacent to the TZC within the Albertine Rift from receiver functions. Thinning of the lithosphere is expected in the Malawi Rift given the >5 km of sediment deposited against the basin-bounding border faults in the North and Central basins (Chapter 3). However, receiver functions show an average Moho-depth of 39-41 km on either side of Lake Malawi (*Borrego et al.*, 2015; *Hopper et al.*, 2017). Assuming a Moho depth of 40 km along the rift axis, the accommodation of 5 km of sediment against the border faults equates to only a ∼12.5% thinning of the crust, below the expect 20% predicted (*Ebinger et al.*, 1987).

We suggest the positive correlation between the magnitude of the anomaly and the proximity of the RVP points to some influence from the thermo-chemical processes occurring there but cannot explain the continuation of the anomaly within the Central Basin. In com-

parison to the 4.6 km/s velocity of the mantle lithosphere beneath the southeastern flank, the anomaly represents as much as a ∼4% velocity reduction in the Central Basin. This reduction in upper mantle velocity beneath the North and Central basins is mostly simply explained by modification and thinning of the lithospheric mantle. If we assume that the unperturbed mantle lithosphere was ∼100 km thick originally, as is observed within the Irumide Belt, our observations suggest as much as a 25-km reduction in lithospheric thickness in the Central Basin. Using the same approach in the North Basin would suggest a reduction of more than 40 km in lithospheric thickness owing to the lack of a high velocity lithosphere (Vs >4.6 km/s) overlying the anomaly there. Alternatively, if we infer similar magnitudes of lithospheric thinning in the two basins, then the reduction in velocities in the North Basin observed at depths <75 km could be interpreted as the thermo-chemical alteration of intact lithosphere related to the North Basin's proximity to the RVP. While the average velocities and implied amount of lithospheric thinning are different, we image a similar anomaly in the MER where relatively fast velocities characteristic of lithosphere beneath the rift flanks (∼4.4 km/s) exist to depths of ∼75 km but are absent from the rift axis (Figure C.9).

The interpretation that greater extension of the mantle lithosphere has occurred in the North Basin compared to the Central Basin has an interesting consequence regarding how extension is accommodated in these two basins. At shallow depths both the North and Central basins are thought to have accommodated similar amounts of stretching as evidenced by the similar magnitude of offset accommodated on the basin-bounding border faults (Chapter 3). Additionally, available constraints on crustal structure indicate ∼12.5% crustal thinning beneath both basins. Taken together, this suggests a variation in the partitioning of extension in the crust and upper mantle between the two basins. One possible mechanism to explain this variation in how extension is accommodated at depth between the two basins may be the proximity of the North Basin to the RVP thermal anomaly. Numerical models of the rifting process have pointed to important feedbacks between conductive heating of the lithosphere, subsequent weakening and thinning of the lithosphere, and melt generation

and infiltration (*Schmeling and Wallner*, 2012; *Havlin et al.*, 2013). However, if the primary control on the magnitude of lithospheric thinning was simply the proximity to the RVP, then why is the region of thinnest mantle lithosphere in the North Basin localized beneath the footwall escarpment rather than more broadly distributed?

The localized nature of the thinned mantle lithosphere centered beneath the rift axis and footwall escarpments in both the North and Central basins points to the potential influential role of strain localizing processes within the lithospheric mantle, such as preexisting structures. The variation in lithospheric thickness that we image both beneath the rift flanks as well as along the axis of the rift bears marked similarity to the asymmetry that characterizes the Malawi Rift at shallow depths. The presence of such asymmetry within both the crust and upper mantle potentially points to a common control like the presence of large-scale preexisting structures. The notion that rifts localize at rheological boundaries is not new (e.g., *Corti et al.*, 2003; *Petit and Ebinger*, 2000; *Versfelt and Rosendahl*, 1989), and many studies have suggested that rift or passive margin asymmetry is related to variations in lithospheric rheology (e.g., *Corti*, 2012; *Brun*, 1999; *Buck*, 1991; *Dunbar and Sawyer*, 1989). At the largest scale, studies of the Western Rift almost ubiquitously highlight the influential role of the Archean TZC and encircling Proterozoic mobile belts in controlling the large-scale rift structure (e.g., *Corti et al.*, 2003; *Nyblade and Brazier*, 2002). More recently, a similar control by preexisting structures has been proposed for the Malawi Rift, which is situated south of the TZC (*Koptev et al.*, in press; *Reed et al.*, 2016; *Sarafian et al.*, 2018). On a more local scale, studies have pointed to the role of preexisting large-scale weaknesses like mechanical sutures in allowing extension to initiate (e.g., *Corti et al.*, 2011; *Rosenbaum et al.*, 2010). One or more tectonic sutures are thought to sit beneath Lake Malawi as evidenced by large structural shear zones that separate abutting mobile belts onshore (*Fritz et al.*, 2013; *Hauzenberger et al.*, 2014). No direct evidence exists to locate the suture between the adjoining mobile belts beneath Lake Malawi, though *McCartney and Scholz* (2016) hypothesized that complex fault structures in the Central Basin were influenced by pre-rift

foliations related to an offshore shear zone. However, the depth extent of such structures are poorly constrained and the mechanism to maintain these large-scale damage zones over relevant geologic timescales is unclear (e.g., *Bercovici and Ricard*, 2012). Our imaging cannot directly identify a major structure such as a suture that may have localized rifting, but the strong correlation in structural asymmetry within the mantle beneath the Malawi Rift suggests that preexisting structures may be influential in controlling rift architecture and the accommodation of extension within the mantle lithosphere.

In the above discussion, we've interpreted shallowing of the high-velocity lithosphere as representing pure mechanical stretching of the lithosphere which assumes that ascending asthenosphere infills where the lithosphere has thinned. However, the velocities that characterize the low velocity zones within the North and Central basin are fast compared to typical mantle asthenosphere (<4.4 km/s). An alternative interpretation for the low velocities beneath these two basins is that these anomalies represent mantle lithosphere undergoing the early stages of mechanical stretching. During the early-stage thinning of the mantle lithosphere several processes can perturb the observed seismic velocities including the development of regions of smaller grain size as a result of strain localization (e.g., *Kirby*, 1985), heating up of the lithosphere due to deformation induced shear heating (e.g., *Regenauer-Lieb and Yuen*, 1998), and heating up of the lithosphere from the ascending, hotter temperature asthenosphere. In addition to these rift related processes, additional influences like the presence of water and other volatiles may also responsible for part of the low velocity anomaly. In the now extinct Reelfoot Rift, *Chen et al.* (2016) invoke the role of water in explaining a moderate reduction in seismic velocities within the mantle along the rift axis as a result of both the rifting process as well the potential influence of a passing mantle plume. As discussed in Section 4.5.1, a volatile rich mantle is expected in the region of the Malawi Rift.

4.6 Conclusions

In this study, we present results from shear velocity imaging of the Malawi Rift with a comparison to the MER and Afar Depression. Velocities within the MER and Afar Depres-

sion are on average significantly slower than those imaged in the Malawi Rift at all depths though this difference is most pronounced within the upper mantle. The consistently faster velocities of the Malawi Rift indicate that likely very little to no partial melt exists within the system, consistent with the observation that the markedly lower velocities of the MER and Afar Depression require only small amounts of partial melt (<1%) to explain their magnitude. In the Malawi Rift, we image a prominent low velocity anomaly within the crust and upper mantle beneath the RVP. The observed velocities within the mantle (4.25 km/s) can be explained by ambient mantle temperatures. The limited spatial extent and presence of surrounding high velocity lithosphere suggest that variations in lithospheric thickness have led to the formation of a stagnation point in mantle flow beneath the RVP. Away from the RVP, we attribute variations in lithospheric structure to preexisting contrasts in lithospheric thickness and potentially enhanced by the thermo-chemical modification of the lithosphere in close proximity to the RVP. Low velocities (<4.45 km/s) are observed along the rift axis and beneath the footwall escarpments of both the North and Central basins. This modest low velocity anomaly is associated with thinning of the high velocity lithosphere consistent with predictions from ongoing extensional processes. Greater thinning and lower velocities are observed in the North Basin pointing to the potentially influential role of the RVP in enhancing thermo-chemical modification of the lithosphere there. Notably, this pattern of greater extension in the mantle lithosphere beneath the North Basin is not mimicked in the upper crust, where the basin-bounding border faults of both basins accommodate similar magnitudes of fault offset. The asymmetric pattern of mantle lithospheric thinning whereby the greatest deformation occurs beneath the footwall escarpments suggests that controls on rift architecture may come from large-scale variations in preexisting lithospheric structure. The comparison presented in this study shows that the state of the upper mantle beneath the Malawi Rift and the MER and Afar Depression are wholly different and suggests that the widespread magma-assisted accommodation of extension in the MER is likely not a viable mechanism to explain the present-day extension of the Malawi Rift.

Bibliography

Accardo, N., D. Shillington, C. Scholz, T. McCartney, C. Ebinger, J. Gaherty, A. Nyblade, A. Eatmon, P. Chindandali, G. Kamihanda, et al. (2016), Constraints on the 3d sediment and crustal architecture of the weakly extended malawi rift from the onshore/offshore wide-angle refraction experiment, in *AGU Fall Meeting Abstracts*.

Accardo, N. J., J. B. Gaherty, D. J. Shillington, C. J. Ebinger, A. A. Nyblade, G. J. Mbogoni, P. R. N. Chindandali, R. W. Ferdinand, G. D. Mulibo, G. Kamihanda, D. Keir, C. Scholz, K. Selway, J. P. O'Donnell, G. Tepp, R. Gallacher, K. Mtelela, J. Salima, and A. Mruma (2017), Surface wave imaging of the weakly extended Malawi Rift from ambient-noise and teleseismic Rayleigh waves from onshore and lake-bottom seismometers, *Geophysical Journal International*, *209*(3), 1892–1905.

Adams, A., A. Nyblade, and D. Weeraratne (2012), Upper mantle shear wave velocity structure beneath the East African plateau: evidence for a deep, plateauwide low velocity anomaly, *Geophysical Journal International*, *189*(1), 123–142.

Ahern, T., R. Benson, R. Casey, C. Trabant, and B. Weertman (2015), Improvements in Data Quality, Integration and Reliability: New Developments at the IRIS DMC, *Advances in Geosciences*, *40*, 31–35.

Armitage, J. J., D. J. Ferguson, S. Goes, J. O. S. Hammond, E. Calais, C. A. Rychert, and N. Harmon (2015), Upper mantle temperature and the onset of extension and break-up in Afar, Africa, *Earth and Planetary Science Letters*, *418*(C), 78–90.

Artemieva, I. M., and W. D. Mooney (2001), Thermal thickness and evolution of Precambrian lithosphere: A global study, *Journal of Geophysical Research*, *106*, 16,387–16,414.

Ayalew, D., C. Ebinger, E. Bourdon, E. Wolfenden, G. Yirgu, and N. Grassineau (2006), Temporal compositional variation of syn-rift rhyolites along the western margin of the southern Red Sea and northern Main Ethiopian Rift, *Geological Society, London, Special Publications*, *259*(1), 121–130.

Bagley, B., and A. A. Nyblade (2013), Seismic anisotropy in eastern Africa, mantle flow, and the African superplume, *Geophysical Research Letters*, *40*(8), 1500–1505.

Baker, J. A., M. F. Thirwall, and M. A. Menzies (1996), Sr-Nd-Pb isotopic and trace element evidence for crustal contamination of plume-derived flood basalts: Oligocene flood volcanism in western Yemen, *Geochemica et Cosmochimica Acta*, *60*, 2559–2581.

Barry, P. H., D. R. Hilton, T. P. Fischer, J. M. de Moor, F. Mangasini, and C. Ramirez (2013), Helium and carbon isotope systematics of cold "mazuku" CO2 vents and hydrothermal gases and fluids from Rungwe Volcanic Province, southern Tanzania, *Chemical Geology*, *339*(C), 141–156.

Bartholomew, I. D., J. M. Peters, and C. M. Powell (1993), Regional structural evolution of the North Sea: oblique slip and the reactivation of basement lineaments, in *Petroleum Geology of Northwest Europe Proceedings of the th Conference*, edited by J. R. Parker, pp. 1109–1122, Petroleum Geology '86 Ltd.

Bastow, I. D., and D. Keir (2011), The protracted development of the continent–ocean transition in Afar, *Nature Geoscience*, *4*(4), 248–250.

Bastow, I. D., A. A. Nyblade, G. W. Stuart, T. O. Rooney, and M. H. Benoit (2008), Upper mantle seismic structure beneath the Ethiopian hot spot: Rifting at the edge of the African low-velocity anomaly, *Geochemistry, Geophysics, Geosystems*, *9*(12).

Bastow, I. D., S. Pilidou, J.-M. Kendall, and G. W. Stuart (2010), Melt-induced seismic anisotropy and magma assisted rifting in Ethiopia: Evidence from surface waves, *Geochemistry, Geophysics, Geosystems*, *11*(6).

Bastow, I. D., D. Keir, and E. Daly (2011), The Ethiopia Afar Geoscientific Lithospheric Experi-

ment (EAGLE): Probing the transition from continental rifting to incipient seafloor spreading, in *Volcanism and Evolution of the African Lithosphere*, pp. 51–76, Geological Society of America.

Begg, G. C., W. L. Griffin, L. M. Natapov, S. Y. O'Reilly, S. P. Grand, C. J. O'Neill, J. M. A. Hronsky, Y. P. Djomani, C. J. Swain, T. Deen, and P. Bowden (2009), The lithospheric architecture of Africa: Seismic tomography, mantle petrology, and tectonic evolution, *Geosphere*, *5*(1), 23–50.

Behn, M. D., G. Hirth, and J. R. Elsenbeck II (2009), Implications of grain size evolution on the seismic structure of the oceanic upper mantle, *Earth and Planetary Science Letters*, *282*(1-4), 178–189.

Bell, D. R., M. D. Schmitz, and P. E. Janney (2003), Mesozoic thermal evolution of the southern African mantle lithosphere, *LITHOS*, *71*(2-4), 273–287.

Bennett, J. D. (1989), Review of Lower Karoo coal basins and coal resource development in parts of central and southern Africa with particular reference to northern Malawi, *Tech. Rep. WC/89/21*, British Geological Survey, Keyworth.

Benoit, M. H., A. A. Nyblade, T. J. Owens, and G. Stuart (2006), Mantle transition zone structure and upper mantle S velocity variations beneath Ethiopia: Evidence for a broad, deep-seated thermal anomaly, *Geochemistry, Geophysics, Geosystems*, *7*(11).

Bensen, G. D., M. H. Ritzwoller, M. P. Barmin, A. L. Levshin, F. Lin, M. P. Moschetti, N. M. Shapiro, and Y. Yang (2007), Processing seismic ambient noise data to obtain reliable broad-band surface wave dispersion measurements, *Geophysical Journal International*, *169*(3), 1239–1260.

Bercovici, D., and Y. Ricard (2012), Mechanisms for the generation of plate tectonics by two-phase grain-damage and pinning, *Physics of the Earth and Planetary Interiors*, *202-203*(C), 27–55.

Berhe, S. (1990), Ophiolites in Northeast and East Africa: implications for Proterozoic crustal growth, *Journal of the Geological Society of London*, *147*, 41–57.

Bialas, R. W., and W. R. Buck (2009), How sediment promotes narrow rifting: Application to the Gulf of California, *Tectonics*, *28*(4).

Bialas, R. W., W. R. Buck, and R. Qin (2010), How much magma is required to rift a continent?, *Earth and Planetary Science Letters*, *292*(1-2), 68–78.

Birt, C. S., P. K. H. Maguire, M. A. Khan, H. Thybo, G. R. Keller, and J. Patel (1997), The influence of pre-existing structures on the evolution of the southern Kenya Rift Valley evidence from seismic and gravity studies, *Tectonophysics*, *278*, 211–242.

Black, R., and J. P. Liegeois (1993), Cratons, mobile belts, alkaline rocks, and continental lithospheric mantle: the Pan-African testimony, *Journal of the Geological Society of London*, *150*, 89–98.

Borrego, D., M. Kachingwe, A. Nyblade, D. Shillington, J. Gaherty, C. Ebinger, N. Accardo, J. O'Donnell, G. Mbogoni, G. Mulibo, et al. (2015), Crustal structure in northern malawi and southern tanzania surrounding lake malawi and the rungwe volcanic province, in *AGU Fall Meeting Abstracts*.

Bott, M. H. P. (1991), Ridge push and associated plate interior stress in normal and hot spot regions, *Tectonophysics*, *200*(1-3), 17–32.

Boyd, F. R., J. J. Gurney, and S. H. Richardson (1985), Evidence for a 150-200-km thick Archaean lithosphere from diamond inclusion thermobarometery, *Nature*, *315*, 387–389.

Branchu, P., L. Bergonzini, D. Delvaux, M. De Batist, V. Golubev, M. Benedetti, and J. Klerkx (2005), Tectonic, climatic and hydrothermal control on sedimentation and water chemistry of northern Lake Malawi (Nyasa), Tanzania, *Journal of African Earth Sciences*, *43*(4), 433–446.

Brun, J.-P. (1999), Narrow Rifts Versus Wide Rifts: Inferences for the Mechanics of Rifting from Laboratory Experiments, *Philosophical Transactions of the Royal Society A: Mathematical, Physical and Engineering Sciences*, *357*, 695–712.

Buck, W. R. (1991), Modes of continental lithospheric extension, *Journal of Geophysical Research*, *96*, 20,161–20,178.

Buck, W. R. (1993), Effect of lithospheric thickness on the formation of high- and low-angle normal faults, *Geology*, *21*, 933–936.

Buck, W. R. (2004), Consequences of asthenospheric variability on continental rifting, in *Rheology and Deformation of the Lithosphere at Continental Margins*, edited by G. D. Karner, B. N. Taylor, W. Droscoll, and D. L. Kohlstedt, pp. 1–30, Columbia University Press, New York.

Buck, W. R. (2006), The role of magma in the development of the Afro-Arabian Rift System, in *The Afar Volcanic Province within the East African Rift System*, edited by G. Yirgu, C. J. Ebinger, and P. K. H. Maguire, pp. 43–54, Geological Society of London.

Cammarano, F., S. Goes, P. Vacher, and D. Giardini (2003), Inferring upper-mantle temperatures from seismic velocities, *Physics of the Earth and Planetary Interiors*, *138*(3-4), 197–222.

Carlson, R. L., and A. F. Gangi (1985), Effect of Cracks on the Pressure-Dependence of P-Wave Velocities in Crystalline Rocks, *Journal of Geophysical Research*, *90*(NB10), 8675–8684.

Cartwright, J. A., B. D. Trudgill, and C. S. Mansfield (1995), Fault growth by segment linkage: an explanation for scatter in maximum displacement and trace length data from the Canyonlands Grabens of SE Utah, *Journal of Structural Geology*, *17*(4), 1319–1326.

Catuneanu, O., H. Wopfner, P. G. Eriksson, B. Cairncross, B. S. Rubidge, R. M. H. Smith, and P. J. Hancox (2005), The Karoo basins of south-central Africa, *Journal of African Earth Sciences*, *43*(1-3), 211–253.

Chang, S.-J., and S. Van der Lee (2011), Mantle plumes and associated flow beneath Arabia and East Africa, *Earth and Planetary Science Letters*, *302*(3-4), 448–454.

Chen, C., H. Gilbert, C. Andronicos, M. W. Hamburger, T. Larson, S. Marshak, G. L. Pavlis, and X. Yang (2016), Shear velocity structure beneath the central United States: implications for the origin of the Illinois Basin and intraplate seismicity, *Geochemistry, Geophysics, Geosystems*, *17*(3), 1020–1041.

Chorowicz, J. (2005), The East African rift system, *Journal of African Earth Sciences*, *43*(1-3), 379–410.

Christensen, N. I., and W. D. Mooney (1995), Seismic velocity structure and composition of the continental crust: A global view, *Journal of Geophysical Research: Solid Earth*, *100*(B7), 9761–9788.

Clifford, T. N. (1966), Tectono-Metallogenic Units and Metallogenic Provinces of Africa, *Earth and Planetary Science Letters*, pp. 421–434.

Contreras, J., M. H. Anders, and C. H. Scholz (2000), Growth of a normal fault system: observations from the Lake Malawi basin of the east African rift, *Journal of Structural Geology*, *22*, 159–168.

Corti, G. (2004), Centrifuge modelling of the influence of crustal fabrics on the development of transfer zones: insights into the mechanics of continental rifting architecture, *Tectonophysics*, *384*(1-4), 191–208.

Corti, G. (2012), Evolution and characteristics of continental rifting: Analog modeling-inspired view and comparison with examples from the East African Rift System, *Tectonophysics*, *522-523*(C), 1–33.

Corti, G., and P. Manetti (2006), Asymmetric rifts due to asymmetric Mohos: An experimental approach, *Earth and Planetary Science Letters*, *245*(1-2), 315–329.

Corti, G., M. Bonini, F. Mazzarini, M. Boccaletti, F. Innocenti, P. Manetti, G. Mulugeta, and D. Sokoutis (2002), Magma-induced strain localization in centrifuge models of transfer zones, *Tectonophysics*, *348*(4), 205–218.

Corti, G., M. Bonini, S. Conticelli, F. Innocenti, P. Manetti, and D. Sokoutis (2003), Analogue modelling of continental extension: a review focused on the relations between the patterns of deformation and the presence of magma, *Earth-Science Reviews*, *63*(3-4), 169–247.

Corti, G., J. van Wijk, S. Cloetingh, and C. K. Morley (2007), Tectonic inheritance and continental rift architecture: Numerical and analogue models of the East African Rift system, *Tectonics*, *26*(6).

Corti, G., G. Ranalli, G. Mulugeta, A. Agostini, F. Sani, and A. Zugu (2010), Control of the rheological structure of the lithosphere on the inward migration of tectonic activity during continental rifting, *Tectonophysics*, *490*(3-4), 165–172.

Corti, G., E. Calignano, C. Petit, and F. Sani (2011), Controls of lithospheric structure and plate kinematics on rift architecture and evolution: An experimental modeling of the Baikal rift, *Tectonics*, *30*(3).

Corti, G., G. Ranalli, A. Agostini, and D. Sokoutis (2013), Inward migration of faulting during continental rifting: Effects of pre-existing lithospheric structure and extension rate, *Tectonophysics*, *594*(C), 137–148.

Cowie, P. A., and C. H. Scholz (1992), Displacement-length scaling relationship for faults: data synthesis and discussion, *Journal of Structural Geology*, *14*(10), 1149–1156.

Crabtree, D. C., and W. Chesworth (1992), Rift related magmatism and the petrogenesis of lavas from the Kiejo eruptive, Rungwe Volcanic Province, S.W. Tanzania, *Basement Tectonics*, *7*, 71–82.

Craig, T. J., J. A. Jackson, K. PRIESTLEY, and D. MCKENZIE (2011), Earthquake distribution patterns in Africa: their relationship to variations in lithospheric and geological structure, and their rheological implications, *Geophysical Journal International*, *185*(1), 403–434.

Crawford, W. C., and S. C. Webb (2000), Identifying and Removing Tilt Noise from Low-Frequency (¡0.1 Hz) Seafloor Vertical Seismic Data, *Bulletin of the Seismological Society of America*, *90*(4), 952–963.

Crossley, R. (1984), Controls of sedimentation in the Malawi Rift valley, Central Africa, *Sedimentary Geology*, *40*, 33–50.

Crossley, R., and M. Crow (1980), The malawi rift, *Geodynamic evolution of the Afro-Arabian rift system: Accademia Nationale Lincei*, pp. 77–87.

Curry, M. A. E., J. B. Barnes, and J. P. Colgan (2016), Testing fault growth models with low-temperature thermochronology in the northwest Basin and Range, USA, *Tectonics*, *35*, 2467–2492.

Daly, M. C., J. Chorowicz, and J. D. Fairhead (1989), Rift basin evolution in Africa: the influ;ence of reactivated steep basement shear zones, in *Inversion Tectonics*, edited by M. A. Cooper and G. D. Williams, pp. 309–334, Geological Society Special Publications No. 44.

Dave, R., and A. Li (2016), Destruction of the Wyoming craton: Seismic evidence and geodynamic processes, *Geology*, *44*(11), 883–886.

Dawers, N. H., and M. H. Anders (1995), Displacement-length scaling and fault linkage, *Journal of Structural Geology*, *17*(5), 607–614.

Dawers, N. H., M. H. Anders, and C. H. Scholz (1993), Growth of normal faults: Displacement-length scaling, *Geology*, *21*, 1107–1110.

De Chabalier, J.-B., and J.-P. Avouac (1994), Kinematics of the Asal Rift (Djibouti) Determined from the Deformation of Fieale Volcano, *Science*, *265*, 1677–1681.

De Waele, B., J.-P. Liégeois, A. A. Nemchin, and F. Tembo (2006), Isotopic and geochemical evidence of proterozoic episodic crustal reworking within the irumide belt of south-central Africa, the southern metacratonic boundary of an Archaean Bangweulu Craton, *Precambrian Research*, *148*(3-4), 225–256.

Delescluse, M., T. Funck, S. Dehler, K. E. Louden, and L. Watremez (2015), The oceanic crustal structure at the extinct, slow to ultraslow Labrador Sea spreading center, *Journal of Geophysical Research: Solid Earth*, *120*, 5249–5272.

Delph, J. R., K. M. Ward, G. Zandt, M. N. Ducea, and S. L. Beck (2017), Imaging a magma plumbing system from MASH zone to magma reservoir, *Earth and Planetary Science Letters*, *457*, 313–324.

Delvaux, D. (1991), The Karoo to recent rifting in the Western Branch of the East African Rift System: A bibliogrpahical synthesis, *Royal Museum of Central Africa - Annual Report*, *1989-1990*, 63–83.

Delvaux, D. (2001), Karoo rifting in western Tanzania: precursor of Gondwana break-up?, in *Contributions to Geology and Palaeontology of Gondwana in Honour of Helmut Wopfner*, edited by R. H. Weiss, pp. 111–125, University of Cologne, Cologne.

Delvaux, D., R. Moeys, G. Stapel, A. Melnikov, and V. Ermikov (1995), Palaeostressreconstructions and geodynamics of the Baikal region, Central Asia, Part I. Palaeozoic and Mesozoic pre-rift evolution, *Tectonophysics*, *252*, 61–101.

Delvaux, D., F. Kervyn, A. S. Macheyeki, and E. B. Temu (2012), Geodynamic significance of the TRM segment in the East African Rift (W-Tanzania): Active tectonics and paleostress in the Ufipa plateau and Rukwa basin, *Journal of Structural Geology*, *37*(C), 161–180.

Dugda, M. T., A. A. Nyblade, J. Julia, C. A. Langston, C. J. Ammon, and S. Simiyu (2005), Crustal structure in Ethiopia and Kenya from receiver function analysis: Implications for rift development in eastern Africa, *Journal of Geophysical Research*, *110*(B01303).

Dugda, M. T., A. A. Nyblade, and J. Julia (2007), Thin Lithosphere Beneath the Ethiopian Plateau Revealed by a Joint Inversion of Rayleigh Wave Group Velocities and Receiver Functions, *Journal of Geophysical Research*, *112*(B8), B08,305.

Dunbar, J. A., and D. S. Sawyer (1989), How preexisting weaknesses control the style of continental breakup, *Journal of Geophysical Research*, *94*, 7278–7292.

Ebinger, C., T. Yemane, G. Woldegabriel, J. Aronson, and R. Walter (1993a), Late eocene–recent volcanism and faulting in the southern main ethiopian rift, *Journal of the Geological Society*, *150*(1), 99–108.

Ebinger, C., D. Poudjom, E. Mbede, A. Foster, and J. B. Dawson (1997), Rifting Archaean lithosphere: the Eyasi–Manyara–Natron rifts, East Africa, *Journal of the Geological Society of London*, *154*, 947–960.

Ebinger, C. J. (1989a), Geometric and kinematic development of border faults and accomodation zones, Kivu-Rusizi Rift, Africa, *Tectonics*, *8*(1), 117–133.

Ebinger, C. J. (1989b), Tectonic development of the western branch of the East African rift system, *Geological Society of America Bulletin*, *101*, 885–903.

Ebinger, C. J., and M. Casey (2001), Continental breakup in magmatic provinces: An Ethiopian example, *Geology*, *29*(6), 527–530.

Ebinger, C. J., and C. A. Scholz (2012), Continental rift basins: the East Africa Perspective, in *Tectonics of Sedimentary Basins Recent Advances*, edited by C. Busby and A. Azor, pp. 185–208, Blackwell Publishing Ltd.

Ebinger, C. J., and N. H. Sleep (1998), Cenozoic magmatism throughout east Africa resulting from impact of a single plume, *Nature*, *395*, 788–791.

Ebinger, C. J., B. R. Rosendahl, and D. J. Reynolds (1987), Tectonic model of the Malawi rift, Africa, *Tectonophysics*, *141*(1-3), 215–235.

Ebinger, C. J., A. L. Deino, E. Drake, and A. L. Tesha (1989), Chronology of volcanism and rift basin propagation: Rungwe Volcanic Province, East Africa, *Journal of Geophysical Research*, *94*, 15,785–15,803.

Ebinger, C. J., G. D. Karner, and J. K. WEISSEL (1991), Mechanical Strength of Extended Continental Lithosphere - Constraints From the Western Rift System, East-Africa, *Tectonics*, *10*(6), 1239–1256.

Ebinger, C. J., A. L. Deino, A. L. Tesha, T. Becker, and U. Ring (1993b), Tectonic controls on rift basin morphology: Evolution of the northern Malawi (Nyasa) Rift, *Journal of Geophysical Research*, *98*, 17,821–17,836.

Ebinger, C. J., J. A. Jackson, A. N. Foster, and N. J. Hayward (1999), Extensional basin geometry and the elastic lithosphere, *Philosophical Transactions of the Royal Society A: Mathematical, Physical and Engineering Sciences*, *357*, 741–765.

Ebinger, C. J., T. Yemane, D. J. Harding, S. Tesfaye, S. Kelley, and D. C. Rex (2000), Rift deflection, migration, and propagation: Linkage of the Ethiopian and Eastern rifts, Africa, *Geological Society of America Bulletin*, *112*(2), 163–176.

Ekström, G., A. M. Dziewoński, and M. Nettles (2012), The global CMT project 2004-2010: Centroid-moment tensors for 13,017 earthquakes, *Physics of the Earth and Planetary Interiors*, *200-201*(C), 1–9.

Ellis, M. A., and J. B. Barnes (2015), A global perspective on the topographic response to fault growth, *Geosphere*, *11*(4), 1008–1023.

Fagereng, A. (2013), Fault segmentation, deep rift earthquakes and crustal rheology: Insights from the 2009 Karonga sequence and seismicity in the Rukwa–Malawi rift zone, *Tectonophysics*, *601*(C), 216–225.

Fagereng, A., M. Hodge, J. Biggs, L. Huang, N. Hellebrekers, and H. Mdala (2017), Perspectives on the effect of pre-existing weaknesses in the malawi rift, east africa, in *GSA Fall Meeting Abstracts*.

Farr, T. G., P. A. Rosen, E. Caro, R. Crippen, R. Duren, S. Hensley, M. Kobrick, M. Paller, E. Rodriguez, L. Roth, D. Seal, S. Shaffer, J. Shimada, J. Umland, M. Werner, M. Oskin, D. Burbank, and D. Alsdorf (2007), The Shuttle Radar Topography Mission, *Reviews of Geophysics*, *45*(2).

Faul, U., and I. Jackson (2005), The seismological signature of temperature and grain size variations in the upper mantle, *Earth and Planetary Science Letters*, *234*(1-2), 119–134.

Faulds, J. E., and R. J. Varga (1998), The role of accommodation zones and transfer zones in the regional segmentation of extended terranes, in *Accommodation Zones and Transfer Zones The Regional Segmentation of hte Basin and Range Province*, edited by J. E. Faulds and J. H. Stewart, pp. 1–45, Geological Society of America.

Ferguson, D. J., J. Maclennan, I. D. Bastow, D. M. Pyle, S. M. Jones, D. Keir, J. D. Blundy, T. Plank, and G. Yirgu (2013), Melting during late-stage rifting in Afar is hot and deep, *Nature*, *499*(7456), 70–73.

Fishwick, S. (2010), Surface wave tomography: Imaging of the lithosphere–asthenosphere boundary beneath central and southern Africa?, *LITHOS*, *120*(1-2), 63–73.

Flannery, J. W., and B. R. Rosendahl (1990), The seismic stratigraphy of Lake Malawi, Africa: implications for interpreting geological processes in lacustrine rifts, *Journal of African Earth Sciences (and the Middle East)*, *10*(3), 519–548.

Flinders, A. F., and Y. Shen (2017), Seismic evidence for a possible deep crustal hot zone beneath Southwest Washington, *Scientific Reports*, *2017*(Aug), 1–10.

Fontijn, K., G. G. J. Ernst, M. A. Elburg, D. Williamson, E. Abdallah, S. Kwelwa, E. Mbede, and P. Jacobs (2010a), Holocene explosive eruptions in the Rungwe Volcanic Province, Tanzania, *Journal of Volcanology and Geothermal Research*, *196*(1-2), 91–110.

Fontijn, K., D. Delvaux, G. G. J. Ernst, M. Kervyn, E. Mbede, and P. Jacobs (2010b), Tectonic control over active volcanism at a range of scales: Case of the Rungwe Volcanic Province, SW Tanzania; and hazard implications, *Journal of African Earth Sciences*, *58*(5), 764–777.

Fontijn, K., D. Williamson, E. Mbede, and G. G. J. Ernst (2012), The Rungwe Volcanic Province, Tanzania - A volcanological review, *Journal of African Earth Sciences*, *63*, 12–31.

Forsyth, D., and S. Uyeda (1975), On the Relative Importance of the Driving Forces of Plate Motion, *Geophysical Journal International*, *43*(1), 163–200.

Forsyth, D. W. (1992), Finite extension and low-angle normal faulting, *Geology*, *20*, 27–30.

Foster, A. N., and J. A. Jackson (1998), Source parameters of large African earthquakes: implications for crustal rheology and regional kinematics, *Geophysical Journal International*, *134*, 422–448.

Fourel, L., L. Milelli, C. Jaupart, and A. Limare (2013), Generation of continental rifts, basins, and swells by lithosphere instabilities, *Journal of Geophysical Research: Solid Earth*, *118*(6), 3080–3100.

Frezzotti, M. L., S. Ferrando, A. Peccerillo, M. Petrelli, F. Tecce, and A. Perucchi (2010), Chlorine-rich metasomatic H2O–CO2 fluids in amphibole-bearing peridotites from Injibara (Lake Tana region, Ethiopian plateau): Nature and evolution of volatiles in the mantle of a region of continental flood basalts, *Geochimica et Cosmochimica Acta*, *74*(10), 3023–3039.

Fritz, H., V. Tenczer, C. Hauzenberger, E. Wallbrecher, and S. Muhongo (2009), Hot granulite nappes — Tectonic styles and thermal evolution of the Proterozoic granulite belts in East Africa, *Tectonophysics*, *477*(3-4), 160–173.

Fritz, H., M. Abdelsalam, K. A. Ali, B. Bingen, A. S. Collins, A. R. Fowler, W. Ghebreab, C. A. Hauzenberger, P. R. Johnson, T. M. Kusky, P. Macey, S. Muhongo, R. J. Stern, and G. Viola (2013), Orogen styles in the East African Orogen: A review of the Neoproterozoic to Cambrian tectonic evolution, *Journal of African Earth Sciences*, *86*(C), 65–106.

Furman, T. (1995), Melting of metasomatized subcontinental lithosphere: undersaturated mafic lavas from Rungwe, Tanzania, *Contribuations to Mineral Petrology*, *122*, 97–115.

Furman, T. (2007), Geochemistry of East African Rift basalts: An overview, *Journal of African Earth Sciences*, *48*(2-3), 147–160.

Furman, T., K. M. Kaleta, J. G. Bryce, and B. B. Hannan (2006), Tertiary Mafic Lavas of Turkana, Kenya: Constraints on East African Plume Structure and the Occurrence of High-μ Volcanism in Africa, *Journal of Petrology*, *47*(6), 1221–1244.

Gallacher, R. J., D. Keir, N. Harmon, G. Stuart, S. Leroy, J. O. S. Hammond, J. M. Kendall, A. Ayele, B. Goitom, G. Ogubazghi, and A. Ahmed (2016), The initiation of segmented buoyancy-driven melting during continental breakup, *Nature Communications*, *7*.

Garrett, I., J. Lin, and C. W. Gable (1996), Dynamics of mantle flow and melting at a ridge-centered hotspot: Iceland and the Mid-Atlantic Ridge, *Earth and Planetary Science Letters*, *144*, 53–74.

George, R., N. Rogers, and S. Kelley (1998), Earliest magmatism in Ethiopia: Evidence for two mantle plumes in one flood basalt province, *Geology*, *26*(10), 923–926.

Gobba, J. M. (1989), Kimberlite exploration in Tanzania, *Journal of African Earth Sciences*, *9*, 565–578.

Goldsworthy, M., and J. Jackson (2001), Migration of activity within normal fault systems: examples from the Quaternary of mainland Greece, *Journal of Structural Geology*, *23*, 489–506.

Grijalva, A. N. (2017), P and S body wave tomography of the northern Lake Malawi Rift Basin and Rungwe Volcanic Province, Master's thesis, The Pennsylvania State University, The Pennsylvania State University.

Guidarelli, M., G. Stuart, J. O. S. Hammond, J.-M. Kendall, A. Ayele, and M. Belachew (2011), Surface wave tomography across Afar, Ethiopia: Crustal structure at a rift triple-junction zone, *Geophysical Research Letters*, *38*(24).

Hacker, B. R., and G. A. Abers (2004), Subduction Factory 3: An Excel worksheet and macro for calculating the densities, seismic wave speeds, and H 2O contents of minerals and rocks at pressure and temperature, *Geochemistry, Geophysics, Geosystems*, *5*(1).

Halldorsson, S. A., D. R. Hilton, P. Scarsi, T. Abede, and J. Hopp (2014), A common mantle plume source beneath the entire East African Rift System revealed by coupled helium-neon systematics, *Geophysical Research Letters*, *41*, 2304–2311.

Hamblock, J. M., C. L. Andronicos, K. C. Miller, C. G. Barnes, M. H. Ren, M. G. Averill, and E. Y. Anthony (2007), A composite geologic and seismic profile beneath the southern Rio Grande rift, New Mexico, based on xenolith mineralogy, temperature, and pressure, *Tectonophysics*, *442*(1-4), 14–48.

Hamilton, E. L. (1976), Variations of Density and Porosity with Depth in Deep-sea Sediments, *Journal of Sedimentary Petrology*, *46*(2), 280–300.

Hammond, J. O. S., J.-M. Kendall, G. W. Stuart, D. Keir, C. Ebinger, A. Ayele, and M. Belachew (2011), The nature of the crust beneath the Afar triple junction: Evidence from receiver functions, *Geochemistry, Geophysics, Geosystems*, *12*(12).

Hammond, W. C., and E. D. Humphreys (2000), Upper mantle seismic wave velocity: Effects of realistic partial melt geometries, *Journal of Geophysical Research*, *105*, 10,975–10,986.

Hansen, S. E., and A. A. Nyblade (2013), The deep seismic structure of the Ethiopia/Afar hotspot and the African superplume, *Geophysical Journal International*, *194*(1), 118–124.

Hansen, S. E., A. A. Nyblade, and M. H. Benoit (2012), Mantle structure beneath Africa and Arabia from adaptively parameterized P-wave tomography: Implications for the origin of Cenozoic Afro-Arabian tectonism, *Earth and Planetary Science Letters*, *319-320*(C), 23–34.

Hansen, S. M., K. G. Dueker, J. C. Stachnik, R. C. Aster, and K. E. Karlstrom (2013), A root-less rockies-Support and lithospheric structure of the Colorado Rocky Mountains inferred from CREST and TA seismic data, *Geochemistry, Geophysics, Geosystems*, *14*(8), 2670–2695.

Hanson, R. E. (2003), Proterozoic geochronology and tectonic evolution of southern Africa, in *Proterozoic East Gondwana Supercontinent Assembly and Breakup*, edited by M. Yoshida, B. F. Windley, and S. Dasgupta, pp. 427–463, The Geological Society of London.

Hauzenberger, C. A., V. Tenczer, A. Bauernhofer, H. Fritz, U. Klötzli, J. Košler, E. Wallbrecher, and S. Muhongo (2014), Termination of the Southern Irumide Belt in Tanzania: Zircon U/Pb geochronology, *Precambrian Research*, *255*, 144–162.

Havlin, C., E. M. Parmentier, and G. Hirth (2013), Dike propagation driven by melt accumulation at the lithosphere–asthenosphere boundary, *Earth and Planetary Science Letters*, *376*(C), 20–28.

Hayward, N. J., and C. J. Ebinger (1996), Variations in the along-axis segmentation of the Afar Rift system, *Tectonics*, *15*, 244–257.

Herrmann, R. B. (2013), Computer Programs in Seismology: An Evolving Tool for Instruction and Research, *Seismological Research Letters*, *84*(6), 1081–1088.

Hier-Majumder, S., and A. Courtier (2011), Seismic signature of small melt fraction atop the transition zone, *Earth and Planetary Science Letters*, *308*(3-4), 334–342.

Hilton, D. R., S. A. Halldórsson, P. H. Barry, T. P. Fischer, J. M. de Moor, C. J. Ramirez, F. Mangasini, and P. Scarsi (2011), Helium isotopes at Rungwe Volcanic Province, Tanzania, and the origin of East African Plateaux, *Geophysical Research Letters*, *38*(21).

Hodgson, I., F. Illsley-Kemp, R. J. Gallacher, D. Keir, C. J. Ebinger, and K. Mtelela (2017), Crustal structure at a young continental rift: A receiver function study from the tanganyika rift, *Tectonics*.

Holtzman, B. K. (2016), Questions on the existence, persistence, and mechanical effects of a very small melt fraction in the asthenosphere, *Geochemistry, Geophysics, Geosystems*, *17*(2), 470–484.

Hopper, E., J. Gaherty, and D. Shillington (2017), Rifting the continental lithosphere: case studies of the lithosphere-asthenosphere system in rifted settings across the western u.s. and in the southern east african rift, in *AGU Fall Meeting Abstracts*.

Hutchinson, D. R., A. J. Golmshtok, L. P. Zonenshain, T. C. Moore, C. A. Scholz, and K. D. Klitgord (1992), Depositional and tectonic framework of the rift basins of Lake Baikal from multichannel seismic data, *Geology*, *20*, 589–592.

Jackson, C. A. L., R. E. Bell, A. Rotevatn, and A. B. M. Tvedt (2017), Techniques to determine the kinematics of synsedimentary normal faults and implications for fault growth models, *Geological Society, London, Special Publications*.

Jackson, I., and U. H. Faul (2010), Grainsize-sensitive viscoelastic relaxation in olivine: Towards a robust laboratory-based model for seismological application, *Physics of the Earth and Planetary Interiors*, *183*(1-2), 151–163.

Jackson, J., and T. Blenkinsop (1993a), The Malawi Earthquake of March 10, 1989: Deep Faulting within the East African Rift System, *Tectonics*, *12*(5), 1131–1139.

Jackson, J., and T. Blenkinsop (1993b), The Malawi Earthquake of March 10, 1989: Deep Faulting within the East African Rift System, *Tectonics*, *12*(5), 1131–1139.

Jackson, J., and T. Blenkinsop (1997), The Bilila-Mtakataka fault in Malawi: An active, 100-km long, normal fault segment in thick seismogenic crust, *Tectonics*, *16*, 137–150.

Jacobs, L. L., D. A. Winkler, Z. M. Kaufulu, and W. R. Downs (1990), The Dinosaur Beds of Northern Malawi, Africa, *National Geographic Research*, *6*(2), 196–204.

Jakovlev, A., G. Rumpker, H. Schmeling, I. Koulakov, M. Lindenfeld, and H. Wallner (2013), Seismic images of magmatic rifting beneath the western branch of the East African rift, *Geochemistry, Geophysics, Geosystems*, *14*(11), 4906–4920.

Jin, G., and J. B. Gaherty (2015), Surface wave phase-velocity tomography based on multichannel cross-correlation, *Geophysical Journal International*, *201*(3), 1383–1398.

Jin, G., J. B. Gaherty, G. A. Abers, Y. Kim, Z. Eilon, and W. R. Buck (2015), Crust and upper mantle structure associated with extension in the Woodlark Rift, Papua New Guinea from Rayleigh-wave tomography, *Geochemistry, Geophysics, Geosystems*, *16*(11), 3808–3824.

Johnson, T. C., J. D. Wells, and C. A. Scholz (1995), Deltaic sedimentation in a modern rift lake, *Geological Society of America Bulletin*, *107*(7), 812–829.

Karato, S.-i. (1993), Importance of anelasticity in the interpretation of seismic tomography, *Geophysical Research Letters*, *20*, 1623–1626.

Katumwehe, A. B., M. G. Abdelsalam, and E. A. Atekwana (2015), The role of pre-existing Precambrian structures in rift evolution: The Albertine and Rhino grabens, Uganda, *Tectonophysics*, *646*(C), 117–129.

Katz, R. F., M. Spiegelman, and C. H. Langmuir (2003), A new parameterization of hydrous mantle melting, *Geochemistry, Geophysics, Geosystems*, *4*(9).

Keir, D., I. D. Bastow, K. A. Whaler, E. Daly, D. G. Cornwell, and S. Hautot (2009), Lower crustal earthquakes near the Ethiopian rift induced by magmatic processes, *Geochemistry, Geophysics, Geosystems*, *10*(6).

Kemp, J. (1975), *The geology of the Uzumara area*, Government Printer, South Africa.

Kendall, J.-M., G. W. Stuart, C. J. Ebinger, I. D. Bastow, and D. Keir (2005), Magma-assisted rifting in Ethiopia, *Nature*, *433*, 146–148.

Kendall, J.-M., S. Pilidou, D. Keir, G. W. Stuart, and A. Ayele (2006), Mantle upwellings, melt migration and rifting in Africa: insights from seismic anisotropy, in *The Afar Volcanic Province within the East African Rift System*, edited by G. Yirgu, C. J. Ebinger, and P. K. H. Maguire, pp. 55–72, Geological Society of London, Special Edition.

Keranen, K., and R. Horne (2014), Magma and underplating in the ethiopian lower crust from a re-analysis of eagle active-source seismic profiles, in *AGU Fall Meeting Abstracts*.

Keranen, K., and S. L. Klemperer (2008), Discontinuous and diachronous evolution of the Main Ethiopian Rift: Implications for development of continental rifts, *Earth and Planetary Science Letters*, *265*(1-2), 96–111.

Keranen, K., S. L. Klemperer, R. Gloaguen, and EAGLE Working Group (2004), Three-dimensional seismic imaging of a protoridge axis in the Main Ethiopian rift, *Geology*, *32*(11), 949.

Keranen, K. M., S. L. Klemperer, J. Julia, J. F. Lawrence, and A. A. Nyblade (2009), Low lower crustal velocity across Ethiopia: Is the Main Ethiopian Rift a narrow rift in a hot craton?, *Geochemistry, Geophysics, Geosystems*, *10*(5).

Key, R. M., B. Bingen, E. Barton, E. X. F. Daudi, S. Manuel, and A. Moniz (2007), Kimberlites in a Karoo graben of northern Mozambique: Tectonic setting, mineralogy and Rb-Sr geochronology, *South African Journal of Geology*, *110*(1), 111–124.

Kieffer, B., N. Arndt, H. LaPierre, F. Bastien, D. Bosch, A. Pecher, G. Yirgu, D. Ayalew, D. Weis, D. A. Jerram, F. Keller, and C. Meuginot (2004), Flood and Shield Basalts from Ethiopia: Magmas from the African Superswell, *Journal of Petrology*, *45*(4), 793–834.

Kilembe, E. A., and B. R. Rosendahl (1992), Structure and stratigraphy of the Rukwa rift, *Tectonophysics*, *209*, 143–158.

Kim, S., A. A. Nyblade, and C. E. BAAG (2010), Crustal velocity structure of the Rukwa Rift in the Western Branch of the East African Rift System, *South African Journal of Geology*, *112*(3-4), 251–260.

Kim, S., A. A. Nyblade, J. Rhie, C.-E. Baag, and T.-S. Kang (2012), Crustal S-wave velocity structure of the Main Ethiopian Rift from ambient noise tomography, *Geophysical Journal International*.

Kim, Y.-S., and D. J. Sanderson (2005), The relationship between displacement and length of faults: a review, *Earth-Science Reviews*, *68*(3-4), 317–334.

Kinabo, B. D., J. P. Hogan, E. A. Atekwana, M. G. Abdelsalam, and M. P. Modisi (2008), Fault growth and propagation during incipient continental rifting: Insights from a combined aeromagnetic and Shuttle Radar Topography Mission digital elevation model investigation of the Okavango Rift Zone, northwest Botswana, *Tectonics*, *27*(3).

King, S. D., and d. L. Anderson (1995), An alternative mechanism of flood basalt formation, *Earth and Planetary Science Letters*, *136*, 269–279.

King, S. D., and J. Ritsema (2000), African Hot Spot Volcanism: Small-Scale Convection in the Upper Mantle Beneath Cratons, *Science*, *290*, 1137–1140.

Kirby, S. H. (1985), Rock mechanics observations pertinent to the rheology of the continental lithosphere and the localization of strain along shear zones, *Tectonophysics*, *119*, 1–27.

Koptev, A., E. Calais, E. Burov, S. Leroy, and T. Gerya (2015), Dual continental rift systems generated by plume-lithosphere interaction, *Nature Geoscience*, *8*(5), 388–392.

Koptev, A., S. Cloetingh, T. Gerya, E. Calais, and S. Leroy (in press), Non-uniform splitting of a single mantle plume by double cratonic roots: Insight into the origin of hte central and southern East African Rift System, *Terra Nova*.

Korenaga, J., W. S. Holbrook, G. M. Kent, P. B. Kelemen, R. S. Detrick, H. C. Larsen, J. R. Hopper, and T. Dahl-Jensen (2000), Crustal structure of the southeast Greenland margin from joint refraction and reflection seismic tomography, *Journal of Geophysical Research: Solid Earth*, *105*(B9), 21,591–21,614.

Korostelev, F., C. Weemstra, S. Leroy, L. Boschi, D. Keir, Y. Ren, I. Molinari, A. Ahmed, G. W. Stuart, F. Rolandone, K. Khanbari, J. O. S. Hammond, J.-M. Kendall, C. Doubre, I. Al Ganad,

B. Goitom, and A. Ayele (2015), Magmatism on rift flanks: Insights from ambient noise phase velocity in Afar region, *Geophysical Research Letters*, *42*, 2179–2188.

Kreuser, T., H. Wopfner, C. Z. Kaaya, S. Markwort, P. M. Semkiwa, and P. Aslandis (1990), Depositional evolution of Permo-Triassic Karoo basins in Tanzania with reference to their economic potential, *Journal of African Earth Sciences*, *10*, 151–167.

Lao-Davila, D. A., H. S. Al-Salmi, M. G. Abdelsalam, and E. A. Atekwana (2015), Hierarchical segmentation of the Malawi Rift: The influence of inherited lithospheric heterogeneity and kinematics in the evolution of continental rifts, *Tectonics*, pp. 1–19.

Le Gall, B., P. Nonnotte, J. Rolet, M. Benoit, H. Guillou, M. Mousseau-Nonnotte, J. Albaric, and J. Deverchère (2008), Rift propagation at craton margin. Distribution of faulting and volcanism in the North Tanzanian Divergence (East Africa) during Neogene time, *Tectonophysics*, *448*(1-4), 1–19.

Lee, C.-T. A., P. Luffi, and E. J. Chin (2011), Building and Destroying Continental Mantle, *Annual Review of Earth and Planetary Sciences*, *39*(1), 59–90.

Lee, H., J. D. Muirhead, T. P. Fischer, C. J. Ebinger, S. A. Kattenhorn, Z. D. Sharp, and G. Kianji (2016), Massive and prolonged deep carbon emissions associated with continental rifting, *Nature Geoscience*, *9*(2), 145–149.

Lin, F.-C., and M. H. Ritzwoller (2011), Helmholtz surface wave tomography for isotropic and azimuthally anisotropic structure, *Geophysical Journal International*, *186*(3), 1104–1120.

Lin, F.-C., M. H. Ritzwoller, and R. Snieder (2009), Eikonal tomography: surface wave tomography by phase front tracking across a regional broad-band seismic array, *Geophysical Journal International*, *177*(3), 1091–1110.

Lyons, R. P., C. A. Scholz, M. R. Buoniconti, and M. R. Martin (2011), Late Quaternary stratigraphic analysis of the Lake Malawi Rift, East Africa: An integration of drill-core and seismic-reflection data, *Palaeogeography, Palaeoclimatology, Palaeoecology*, *303*(1-4), 20–37.

Macgregor, D. (2015), History of the development of the East African Rift System: A series of interpreted maps through time, *Journal of African Earth Sciences*, *101*, 232–252.

Maguire, P., G. R. Keller, S. L. Klemperer, G. D. Mackenzie, K. Keranen, S. Harder, B. OReilly, H. Thybo, L. Asfaw, M. A. Khan, and M. Amha (2006), Crustal structure of the northern Main Ethiopian Rift from the EAGLE controlled-source survey; a snapshot of incipient lithospheric break-up, in *The Afar Volcanic Province within the East African Rift System*, edited by G. Yirgu, C. J. Ebinger, and P. K. H. Maguire, pp. 269–291, Geological Society of London, Special Edition.

Masters, G., M. Barmine, and S. Kientz (2014), Mineos users' manual, in *Computational Infrastructure for Geodynamics*, Computational Infrastructure for Geodynamics, Pasadena.

McCartney, T., and C. A. Scholz (2016), A 1.3 million year record of synchronous faulting in the hangingwall and border fault of a half-graben in the Malawi (Nyasa) Rift, *Journal of Structural Geology*, *91*(C), 114–129.

McCartney, T., C. A. Scholz, D. J. Shillington, C. J. Ebinger, N. J. Accardo, P. R. N. Chindandali, and G. Kamihanda (2016), Implications of longlived intrabasin faulting in the hangingwall of the 120 km long border fault of the deeply subsided central basin of the Malawi (Nyasa) Rift, in *American Geophysical Union Fall Meeting*.

McConnell, B. B. (1972), Geological Development of the Rift System of Eastern Africa, *Geological Society of America Bulletin*, *83*, 2549–2572.

Menke, W., and G. Jin (2015), Waveform Fitting of Cross Spectra to Determine Phase Velocity Using Aki's Formula, *Bulletin of the Seismological Society of America*, *105*(3), 1619–1627.

Mesko, G., C. Class, M. Maqway, N. Boniface, S. Manya, and S. Hemming (2014), The timing of early magmatism and extension in the southern east african rift: Tracking geochemical source variability with 40ar/39ar geochronology at the rungwe volcanic province, sw tanzania, in *AGU Fall Meeting Abstracts*.

Mesko, G., C. Class, M. Maqway, N. Boniface, S. Manya, and S. Hemming (in prep), Character and quantification of plume influence at rungwe volcanic province, *Geophysical Journal International*.

Modisi, M. P., E. A. Atekwana, A. B. Kampunzu, and T. H. Ngwisanyi (2000), Rift kinematics during the incipient stages of continental extension: Evidence from the nascent Okavango rift basin, northwest Botswana, *Geology*, *28*, 939–942.

Moeller, S., I. Grevemeyer, C. R. Ranero, C. Berndt, D. Klaeschen, V. Sallares, N. Zitellini, and R. de Franco (2013), Early-stage rifting of the northern Tyrrhenian Sea Basin: Results from a combined wide-angle and multichannel seismic study, *Geochemistry, Geophysics, Geosystems*, *14*(8), 3032–3052.

Morley, C. K. (1988), Variable extension in Lake Tanganyika, *Tectonics*, *7*(4), 785–801.

Morley, C. K. (1999), Patterns of Displacement Along Large Normal Faults: Implications for Basin Evolution and Fault Propagation, Based on Examples from East Africa, *American Association of Petroleum Geologists*, *83*, 613–634.

Morley, C. K. (2002), Evolution of large normal faults: Evidence from seismic reflection data, *American Association of Petroleum Geologists*, *86*(6), 961–978.

Morley, C. K. (2010), Stress re-orientation along zones of weak fabrics in rifts: An explanation for pure extension in 'oblique' rift segments?, *Earth and Planetary Science Letters*, *297*(3-4), 667–673.

Morley, C. K., R. A. Nelson, T. L. Patton, and S. G. Munn (1990), Transfer Zones in the East African Rift System and Their Relevance to Hydrocarbon Exploration in Rifts, *American Association of Petroleum Geologists*, *74*(8), 1234–1253.

Morley, C. K., S. M. Cunningham, R. M. Harper, and W. A. Wescott (1992), Geology and geophysics of the Rukwa Rift, East Africa, *Tectonics*, *11*, 69–81.

Mortimer, E., D. A. Paton, C. A. Scholz, M. R. Strecker, and P. Blisniuk (2007), Orthogonal to oblique rifting: effect of rift basin orientation in the evolution of the North basin, Malawi Rift, East Africa, *Basin Research*, *19*(3), 393–407.

Mortimer, E., L. A. Kirstein, F. M. Stuart, and M. R. Strecker (2016a), Spatio-temporal trends in normal-fault segmentation recorded by low-temperature thermochronology: Livingstone fault

scarp, Malawi Rift, East African Rift System, *Earth and Planetary Science Letters*, *455*(C), 62–72.

Mortimer, E. J., D. A. Paton, C. A. Scholz, and M. R. Strecker (2016b), Implications of structural inheritance in oblique rift zones for basin compartmentalization: Nkhata Basin, Malawi Rift (EARS), *Marine and Petroleum Geology*, *72*(C), 110–121.

Moustafa, A. R. (2002), Controls on the geometry of transfer zones in the Suez rift and northwest Red Sea: Implications for the structural geometry of rift systems, *American Association of Petroleum Geologists*, *86*(6), 979–1002.

Mulibo, G. D., and A. A. Nyblade (2013), The P and S wave velocity structure of the mantle beneath eastern Africa and the African superplume anomaly, *Geochemistry, Geophysics, Geosystems*, *14*(8), 2696–2715.

Mulibo, G. D., and A. A. Nyblade (2016), The seismotectonics of Southeastern Tanzania: Implications for the propagation of the eastern branch of the East African Rift, *Tectonophysics*, *674*, 20–30.

Müller, R. D., M. Seton, S. Zahirovic, S. E. Williams, K. J. Matthews, N. M. Wright, G. E. Shephard, K. T. Maloney, N. Barnett-Moore, M. Hosseinpour, D. J. Bower, and J. Cannon (2016), Ocean Basin Evolution and Global-Scale Plate Reorganization Events Since Pangea Breakup, *Annual Review of Earth and Planetary Sciences*, *44*(1), 107–138.

Nicholson, S. E., D. Klotter, and G. Chavula (2013), A detailed rainfall climatology for Malawi, Southern Africa, *International Journal of Climatology*, *34*(2), 315–325.

Nicol, A., J. Walsh, K. Berryman, and S. Nodder (2005), Growth of a normal fault by the accumulation of slip over millions of years, *Journal of Structural Geology*, *27*(2), 327–342.

Nixon, C. W., L. C. McNeill, J. M. Bull, R. E. Bell, R. L. Gawthorpe, T. J. Henstock, D. Christodoulou, M. Ford, B. Taylor, D. Sakellariou, G. Ferentinos, G. Papatheodorou, M. R. Leeder, R. E. L. Collier, A. M. Goodliffe, M. Sachpazi, and H. Kranis (2016), Rapid spatiotempo-

ral variations in rift structure during development of the Corinth Rift, central Greece, *Tectonics*, *35*(5), 1225–1248.

Nyblade, A. A., and R. A. Brazier (2002), Precambrian lithospheric controls on the development of the East African rift system, *Geology*, *30*(8), 755–758.

Nyblade, A. A., and C. A. Langston (2002), Broadband Seismic Experiments Probe the East African Rift, *Eos*, *83*, 405–416.

Nyblade, A. A., T. J. Owens, H. Gurrola, J. Ritsema, and C. A. Langston (2000), Seismic evidence for a deep upper mantle thermal anomaly beneath east Africa, *Geology*, *28*(7), 599–602.

O'Donnell, J. P., A. Adams, A. A. Nyblade, G. D. Mulibo, and F. Tugume (2013), The uppermost mantle shear wave velocity structure of eastern Africa from Rayleigh wave tomography: constraints on rift evolution, *Geophysical Journal International*, *194*(2), 961–978.

O'Donnell, J. P., K. Selway, A. A. Nyblade, R. A. Brazier, N. E. Tahir, and R. J. Durrheim (2016), Thick lithosphere, deep crustal earthquakes and no melt: a triple challenge to understanding extension in the western branch of the East African Rift, *Geophysical Journal International*, *204*(2), 985–998.

Olive, J.-A., M. D. Behn, and L. C. Malatesta (2014), Modes of extensional faulting controlled by surface processes, *Geophysical Research Letters*, *41*(19), 6725–6733.

Parsons, B., and J. G. Sclater (2007), An analysis of the variation of ocean floor bathymetry and heat flow with age, *Journal of Geophysical Research*, *82*, 1–25.

Pasyanos, M. E., and A. A. Nyblade (2007), A top to bottom lithospheric study of Africa and Arabia, *Tectonophysics*, *444*(1-4), 27–44.

Paul, D., and S. Mitra (2013), Experimental models of transfer zones in rift systems, *AAPG Bulletin*, *97*(5), 759–780.

Peirce, J. W., and L. Lipkov (1988), Structural Interpretation of the Rukwa Rift, Tanzania, *Geophysics*, *53*, 824–836.

Pérez-Gussinyé, M., M. Metois, M. Fernández, J. Vergés, J. Fullea, and A. R. Lowry (2009), Effective elastic thickness of Africa and its relationship to other proxies for lithospheric structure and surface tectonics, *Earth and Planetary Science Letters*, *287*(1-2), 152–167.

Petit, C., and C. Ebinger (2000), Flexure and mechanical behavior of cratonic lithosphere: Gravity models of the East African and Baikal rifts, *Journal of Geophysical Research*, pp. 19,151–19,162.

Pik, R., C. Deniel, C. Coulon, G. Yirgu, and B. Marty (1999), Isotopic and trace element signatures of Ethiopian flood basalts: evidence for plume–lithosphere interactions, *Geochimica et Cosmochimica Acta*, *63*(15), 2263–2279.

Pinna, P., S. Muhongo, B. A. Micharo, E. Le Goff, Y. Deschamps, F. Ralay, and J. P. Milesi (2004), Geology and Mineral Map of Tanzania.

Plasman, M., C. Tiberi, C. Ebinger, S. Gautier, J. Albaric, S. Peyrat, J. Deverchère, B. Le Gall, P. Tarits, S. Roecker, F. Wambura, A. Muzuka, G. Mulibo, K. Mtelela, M. Msabi, G. Kianji, S. Hautot, J. Perrot, and R. Gama (2017), Lithospheric low-velocity zones associated with a magmatic segment of the Tanzanian Rift, East Africa, *Geophysical Journal International*, *210*(1), 465–481.

Précigout, J., and F. Gueydan (2009), Mantle weakening and strain localization: Implications for the long-term strength of the continental lithosphere, *Geology*, *37*(2), 147–150.

Priestley, K., and D. McKenzie (2006), The thermal structure of the lithosphere from shear wave velocities, *Earth and Planetary Science Letters*, *244*(1-2), 285–301.

Ramsay, T., and R. Pysklywec (2011), Anomalous bathymetry, 3D edge driven convection, and dynamic topography at the western Atlantic passive margin, *Journal of Geodynamics*, *52*(1), 45–56.

Rasskazov, S. V. (1994), Magmatism related to the Eastern Siberian Rift System and the geodynamics, *Bull. Centres. Rech. Explor. Elf Aquitaine*, *18*, 437–452.

Rasskazov, S. V., N. A. Logachev, A. V. Ivanov, A. A. Boven, M. N. Maslovskaya, E. V. Saranina, I. S. Brandt, and S. B. Brandt (2003), A magmatic episode in the western rift of East Africa (19-17 ma), , *Geologiya i Geofizika*, *44*(4), 317–324.

Rau, C. J., and D. W. Forsyth (2011), Melt in the mantle beneath the amagmatic zone, southern Nevada, *Geology*, *39*(10), 975–978.

Reed, C. A., K. H. Liu, P. R. N. Chindandali, B. Massingue, H. Mdala, D. Mutamina, Y. Yu, and S. S. Gao (2016), Passive rifting of thick lithosphere in the southern East African Rift: Evidence from mantle transition zone discontinuity topography, *Journal of Geophysical Research: Solid Earth*, *121*(11), 8068–8079.

Reeve, M. T., R. E. Bell, O. B. Duffy, C. A. L. Jackson, and E. Sansom (2015), The growth of non-colinear normal fault systems; What can we learn from 3D seismic reflection data?, *Journal of Structural Geology*, *70*(C), 141–155.

Regenauer-Lieb, K., and D. A. Yuen (1998), Rapid conversion of elastic energy into plastic shear heating during incipient necking of the lithosphere, *Geophysical Research Letters*, *25*, 2737–2740.

Regenauer-Lieb, K., G. Rosenbaum, and R. F. Weinberg (2008), Strain localisation and weakening of the lithosphere during extension, *Tectonophysics*, *458*(1-4), 96–104.

Ring, U. (1994), The influence of preexisting structure on the evolution of the Cenozoic Malawi rift (East African rift system), *Tectonics*, *13*, 313–326.

Ritsema, J., and H. van Heijst (2000), New seismic model of the upper mantle beneath Africa, *Geology*, *28*, 63–66.

Roberts, E. M., P. M. O'Connor, M. D. Gottfried, N. Stevens, S. Kapalima, and S. Ngasala (2004), Revised stratigraphy and age of the Red Sandstone Group in the Rukwa Rift Basin, Tanzania, *Cretaceous Research*, *25*(5), 749–759.

Roberts, E. M., P. M. O'Connor, N. J. Stevens, M. D. Gottfried, Z. A. Jinnah, S. Ngasala, A. M. Choh, and R. A. Armstrong (2010), Sedimentology and depositional environments of the Red

Sandstone Group, Rukwa Rift Basin, southwestern Tanzania: New insight into Cretaceous and Paleogene terrestrial ecosystems and tectonics in sub-equatorial Africa, *Journal of African Earth Sciences*, *57*(3), 179–212.

Roberts, E. M., N. J. Stevens, and P. M. O'Connor (2012), Initiation of the western branch of the East African Rift coeval with the eastern branch, *Nature Geoscience*, *5*(4), 289–294.

Rooney, T. O., I. D. Bastow, and D. Keir (2011), Insights into extensional processes during magma assisted rifting: Evidence from aligned scoria cones, *Journal of Volcanology and Geothermal Research*, *201*(1-4), 83–96.

Rosenbaum, G., K. Regenauer-Lieb, and R. F. Weinberg (2010), Interaction between mantle and crustal detachments: A nonlinear system controlling lithospheric extension, *Journal of Geophysical Research*, *115*(B11).

Rosendahl, B. R. (1987), Architecture of Continental Rifts with Special Reference to East Africa, *Annual Review of Earth and Planetary Sciences*, *15*, 445–503.

Rosendahl, B. R., E. Kilembe, and K. Kaczmarick (1992), Comparison of the Tanganyika, Malawi, Rukwa and Turkana Rift Zones From Analyses of Seismic-Reflection Data, *Tectonophysics*, *213*(1-2), 235–256.

Ruppel, C. (1995), Extensional processes in continental lithosphere, *Journal of Geophysical Research*, *100*(B12), 24,187–24,215.

Rychert, C. A., N. Schmerr, and N. Harmon (2012), The Pacific lithosphere-asthenosphere boundary: Seismic imaging and anisotropic constraints from SS waveforms, *Geochemistry, Geophysics, Geosystems*, *13*(9).

Sarafian, E., R. L. Evans, M. G. Abdelsalam, E. Atekwana, J. Elsenbeck, A. G. Jones, and E. Chikambwe (2018), Imaging Precambrian lithospheric structure in Zambia using electromagnetic methods, *Gondwana Research*, *54*, 38–49.

Saria, E., E. Calais, D. S. Stamps, D. Delvaux, and C. J. H. Hartnady (2014), Present-day kinematics of the East African Rift, *Journal of Geophysical Research*, *119*, 3584–3600.

Schlische, R. W., S. S. Young, R. V. Ackermann, and A. Gupta (1996), Geometry and scaling relations of a population of very small rift-related normal faults, *Geology*, *24*, 683–686.

Schmeling, H., and H. Wallner (2012), Magmatic lithospheric heating and weakening during continental rifting: A simple scaling law, a 2-D thermomechanical rifting model and the East African Rift System, *Geochemistry, Geophysics, Geosystems*, *13*(8).

Scholz, C. A. (1989), *Seismic Atlas of Lake Malawi (Nyasa), East Africa*, Project PROBE, Duke University.

Scholz, C. A. (1995a), Deltas of the Lake Malawi Rift, East Africa: Seismic Expression and Exploration Implications, *AAPG Bulletin*, *79*(11), 1679–1697.

Scholz, C. A. (1995b), Seismic stratigraphy of an accommodation-zone margin rift-lake delta, Lake Malawi, Africa, in *Hydrocarbon Habitat in Rift Basins*, edited by J. J. Lambiase, pp. 183–195, Geological Society Special Publications.

Scholz, C. A., and B. R. Rosendahl (1988), Low Lake Stands in Lakes Malawi and Tanganyika, East Africa, Delineated with Multifold Seismic Data, *Science*, *240*(4859), 1645–1648.

Scholz, C. A., A. S. COHEN, T. C. Johnson, J. King, M. R. Talbot, and E. T. Brown (2011), Scientific drilling in the Great Rift Valley: The 2005 Lake Malawi Scientific Drilling Project — An overview of the past 145,000years of climate variability in Southern Hemisphere East Africa, *Palaeogeography, Palaeoclimatology, Palaeoecology*, *303*(1-4), 3–19.

Scholz, C. H., and J. C. Contreras (1998), Mechanics of continental rift architecture, *Geology*, *26*(11), 967–970.

Shillington, D., C. Scholz, J. Gaherty, N. Accardo, T. McCartney, P. Chindandali, G. Kamihanda, P. Trinhammer, D. Wood, M. Khalfan, et al. (2015), Active-source seismic imaging below lake malawi (nyasa) from the segment project, in *AGU Fall Meeting Abstracts*.

Shillington, D. J., C. L. Scott, T. A. Minshull, R. A. Edwards, P. J. Brown, and N. White (2009), Abrupt transition from magma-starved to magma-rich rifting in the eastern Black Sea, *Geology*, *37*(1), 7–10.

Shillington, D. J., J. B. Gaherty, C. J. Ebinger, C. A. Scholz, K. Selway, A. A. Nyblade, P. A. Bedrosian, C. Class, S. L. Nooner, M. E. Pritchard, J. Elliott, P. R. N. Chindandali, G. Mbogoni, R. Wambura Ferdinand, N. Boniface, S. Manya, G. Kamihanda, E. Saria, G. Mulibo, J. Salima, A. Mruma, L. Kalindekafe, N. J. Accardo, D. Ntambila, M. Kachingwe, G. T. Mesko, T. McCartney, M. Maquay, J. P. O'Donnell, G. Tepp, K. Mtlela, P. Trinhammer, D. Wood, E. Aaron, M. Gibaud, M. Rapa, C. Pfiefer, F. Mphepo, D. Gondwe, G. Arroyo, C. Eddy, B. Kamoga, and M. Moshi (2016), Acquisition of a Unique Onshore/Offshore Geophysical and Geochemical Dataset in the Northern Malawi (Nyasa) Rift, *Seismological Research Letters*, *87*(6), 1–11.

Sippel, J., C. Meeßen, M. Cacace, J. Mechie, S. Fishwick, C. Heine, M. Scheck-Wenderoth, and M. R. Strecker (2017), The Kenya rift revisited: insights into lithospheric strength through data-driven 3-D gravity and thermal modelling, *Solid Earth*, *8*(1), 45–81.

Smith, M., and P. Mosley (1993), Crustal heterogeneity and basement influence on the development of the Kenya Rift, East Africa, *Tectonics*, *12*, 591–606.

Soreghan, M. J., C. A. Scholz, and J. T. Wells (1999), Coarse-Grained, Deep-Water Sedimentation Along a Border Fault Margin of Lake Malawi, Africa: Seismic stratigraphic analysis, *Journal of Sedimentary Research*, *69*(4), 832–846.

Specht, T. D., and B. R. Rosendahl (1989), Architecture of the Lake Malawi Rift, East Africa, *Journal of African Earth Sciences*, *8*, 355–382.

Stachnik, J. C., A. F. Sheehan, D. W. Zietlow, Z. Yang, J. Collins, and A. Ferris (2012), Determination of New Zealand Ocean Bottom Seismometer Orientation via Rayleigh-Wave Polarization, *Seismological Research Letters*, *83*(4), 704–713.

Stamps, D. S., L. M. Flesch, E. Calais, and A. Ghosh (2014), Current kinematics and dynamics of Africa and the East African Rift system, *Journal of Geophysical Research: Solid Earth*, *119*, 5161–5186.

Stern, R. J. (1994), Arc Assembly and Continental Collision in the Neoproterozoic East African Orogen: Implications for the Consolidation of Gondwanaland, *Annual Review of Earth and Planetary Sciences*, *22*, 319–351.

Stern, R. J., K. C. Nielsen, E. Best, M. Sultan, R. E. Arvidson, and A. Kroner (1990), Orientation of late Precambrian sutures in the Arabian-Nubian shield, *Geology*, *18*, 1103–1106.

Stiefenhofer, J., and D. J. Farrow (2004), Geology of the Mwadui kimberlite, Shinyanga district, Tanzania, *LITHOS*, *76*(1-4), 139–160.

Stuart, G. W., I. D. Bastow, and C. J. Ebinger (2006), Crustal structure of the northern Main Ethiopian Rift from receiver function studies, *Geological Society, London, Special Publications*, *259*(1), 253–267.

ten Brink, U. S. (1991), Volcano spacing and plate rigidity, *Geology*, *19*, 397–400.

ten Brink, U. S., and M. H. Taylor (2002), Crustal structure of central Lake Baikal: Insights into intracontinental rifting, *Journal of Geophysical Research*, *107*(B7).

Tepp, G. (2016), Seismic Analysis of Magmatism in the Galapagos Archipelago and East Africa, Ph.D. thesis, ProQuest Dissertations Publishing, University of Rochester.

Theunissen, K., J. Klerkx, A. Melnikov, and A. Mruma (1996), Mechanisms of inheritance of rift faulting in the western branch of the East African Rift, Tanzania, *Tectonics*, *15*(4), 776–790.

Toomey, D., R. Allen, A. Barclay, S. Bell, P. Bromirski, R. Carlson, X. Chen, J. Collins, R. Dziak, B. Evers, D. Forsyth, P. Gerstoft, E. Hooft, D. Livelybrooks, J. Lodewyk, D. Luther, J. McGuire, S. Schwartz, M. Tolstoy, A. Trehu, M. Weirathmueller, and W. Wilcock (2014), The Cascadia Initiative: A Sea Change In Seismological Studies of Subduction Zones, *Oceanography*, *27*(2), 138–150.

Turcotte, D., and G. Schubert (2014), *Geodynamics*, Cambridge University Press.

Upcott, N. M., R. K. Mukasa, C. J. Ebinger, and G. D. Karner (1996), Along-axis segmentation and isostasy in the Western rift, East Africa, *Journal of Geophysical Research*, *101*(B2), 3247–3268.

Van Avendonk, H. J. A., L. L. Lavier, D. J. Shillington, and G. Manatschal (2009), Extension of continental crust at the margin of the eastern Grand Banks, Newfoundland, *Tectonophysics*, *468*(1-4), 131–148.

van der Lee, S. (2002), High-resolution estimates of lithospheric thickness from Missouri to Massachusetts, USA, *Earth and Planetary Science Letters*, *203*, 15–23.

van Wijk, J. W., J. F. Lawrence, and N. W. Driscoll (2008), Formation of the Transantarctic Mountains related to extension of the West Antarctic Rift system, *Tectonophysics*, *458*(1-4), 117–126.

van Wyk de Vries, B., and O. Merle (1996), The effect of volcanic constructs on rift fault patterns, *Geology*, *24*, 643–646.

Venzke, E., R. Wunderman, L. McClelland, T. Simkin, J. Luhr, L. Siebert, G. Mayberry, and S. Sennert (2002), Global volcanism, 1968 to the present, *Smithsonian Institution, Global Volcanism Program Digital Information Series, GVP-4 (http://www. volcano. si. edu/reports/)*.

Versfelt, J., and B. R. Rosendahl (1989), Relationships between pre-rift structure and rift architecture in Lakes Tanganyika and Malawi, East Africa, *Nature*, *337*(6205), 354–357.

Vidale, J. E. (1990), Finite-difference calculation of traveltimes in three dimensions, *Geophysics*, *55*(5), 521–526.

Vollmer, M. K., H. A. Bootsma, R. E. Hecky, G. Patterson, J. D. Halfman, J. M. Edmond, D. H. Eccles, and R. F. Weiss (2005), Deep-water warming trend in Lake Malawi, East Africa, *Limnology and Oceanography*, pp. 727–732.

Walker, K. T., A. A. Nyblade, S. L. Klemperer, G. H. R. Bokelmann, and T. J. Owens (2004), On the relationship between extension and anisotropy: Constraints from shear wave splitting across the East African Plateau, *Journal of Geophysical Research*, *109*(B8), B08,302.

Walsh, J. J., A. Nicol, and C. Childs (2002), An alternative model for the growth of faults, *Journal of Structural Geology*, *24*, 1669–1675.

Wanless, V. D., M. D. Kurz, J. Elsenbeck, J. Curtice, A. M. Shaw, and E. A. Atekwana (2016), Helium isotopes in hot spring gases as magmatic tracers during incipient rifting in malawi and zambia, in *AGU Fall Meeting Abstracts*.

Watanabe, T. (1993), Effects of Water and Melt on Seismic Velocities and their Application to Characterization of Seismic Reflectors, *Geophysical Research Letters*, *20*, 2933–2936.

Watremez, L., K. W. Helen Lau, M. R. Nedimović, and K. E. Louden (2015), Traveltime tomography of a dense wide-angle profile across Orphan Basin, *Geophysics*, *80*(3), B69–B82.

Webb, S. C. (1998), Broadband seismology and noise under the ocean, *Reviews of Geophysics*, *36*(1), 105–142.

Webb, S. C., and W. C. Crawford (1999), Long-Period Seafloor Seismology and Deformation under Ocean Waves, *Bulletin of the Seismological Society of America*, *89*(6), 1535–1542.

Weeraratne, D. S., D. W. Forsyth, K. M. Fischer, and A. A. Nyblade (2003), Evidence for an upper mantle plume beneath the Tanzanian craton from Rayleigh wave tomography, *Journal of Geophysical Research*, *108*(B9).

Wescott, W. A., W. N. Krebs, D. W. Engelhardt, and S. M. Cunningham (1991), New Biostratigraphic Age Dates from the Lake Rukwa Rift Basin in Western Tanzania, *American Association of Petroleum Geologists*, *75*, 1255–1263.

Whaler, K. A., and S. Hautot (2006), The electrical resistivity structure of the crust beneath the northern Main Ethiopian Rift, *Special Publications -Geological ...*.

Wheeler, W. H., and J. A. Karson (1989), Structure and kinematics of the Livingstone Mountains border fault zone, Nyasa (Malawi) Rift, southwestern Tanzania, *Journal of African Earth Sciences*, *8*, 393–413.

Wheeler, W. H., and B. R. Rosendahl (1994), Geometry of the Livingstone Mountains Border Fault, Nyasa (Malawi) Rift, East Africa, *Tectonics*, *13*, 303–312.

Whipp, P. S., C. A.-L. Jackson, R. L. Gawthorpe, T. Dreyer, and D. Quinn (2014), Normal fault array evolution above a reactivated rift fabric; a subsurface example from the northern Horda Platform, Norwegian North Sea, *Basin Research*, *26*(4), 523–549.

White, R. S., J. W. Bown, and J. R. Smallwood (1995), The temperature of the Iceland plume and origin of outward-propagating V-shaped ridges, *Journal of the Geological Society of London*, *152*, 1039–1045.

Whitmarsh, R. B., S. M. Dean, T. A. Minshull, and M. Tompkins (2000), Tectonic implications of exposure of lower continental crust beneath the Iberia Abyssal Plain, Northeast Atlantic Ocean: Geophysical evidence, *Tectonics*, *19*(5), 919–942.

Wilde-Piórko, M., M. Świeczak, M. Grad, and M. Majdański (2010), Integrated seismic model of the crust and upper mantle of the Trans-European Suture zone between the Precambrian craton and Phanerozoic terranes in Central Europe, *Tectonophysics*, *481*(1-4), 108–115.

Wilson, J. T. (1966), Did the Atlantic close and then repoen?, *Nature*, *211*, 676–681.

Wölbern, I., G. Rümpker, A. Schumann, and A. Muwanga (2010), Crustal thinning beneath the Rwenzori region, Albertine rift, Uganda, from receiver-function analysis, *International Journal of Earth Sciences*, *99*(7), 1545–1557.

Wölbern, I., G. Rumpker, K. Link, and F. Sodoudi (2012), Melt infiltration of the lower lithosphere beneath the Tanzania craton and the Albertine rift inferred from S receiver functions, *Geochemistry, Geophysics, Geosystems*, *13*(8).

WoldeGabriel, G., R. C. Walter, W. K. Hart, and S. A. Mertzman (1999), *Temporal relations and geochemical features of felsic volcanism in the central sector of the Main Ethiopian Rift*, Acta Vulcanologica.

Wolfe, C. J., I. T. Bjarnason, J. C. VanDecar, and S. C. Solomon (1997), Seismic structure of the Iceland mantle plume, *Nature*, *385*, 245–247.

Wolfenden, E., C. Ebinger, G. Yirgu, A. Deino, and D. AYALEW (2004), Evolution of the northern Main Ethiopian rift: birth of a triple junction, *Earth and Planetary Science Letters*, *224*(1-2), 213–228.

Wolfenden, E., C. Ebinger, G. Yirgu, P. R. Renne, and S. P. Kelley (2005), Evolution of a volcanic rifted margin: Southern Red Sea, Ethiopia, *Geological Society of America Bulletin*, *117*(7-8), 846–864.

Wood, D. A., H. J. Zal, C. A. Scholz, C. J. Ebinger, and I. Nizere (2015), Evolution of the Kivu Rift, East Africa: interplay among tectonics, sedimentation and magmatism, *Basin Research*, *29*(2), 175–188.

Wopfner, H. (1994), The Malagasy Rift, a chasm in the Tethyan margin of Gondwana, *Journal of Southeast Asian Earth Sciences*, *9*(4), 451–461.

Wopfner, H. (2002), Tectonic and climatic events controlling deposition in Tanzanian Karoo basins, *Journal of African Earth Sciences*, *34*, 167–177.

Xu, P., and D. Zhao (2009), Upper-mantle velocity structure beneath the North China Craton: implications for lithospheric thinning, *Geophysical Journal International*, *177*(3), 1279–1283.

Yu, Y., S. S. Gao, M. Moidaki, C. A. Reed, and K. H. Liu (2015), Seismic anisotropy beneath the incipient Okavango rift: Implications for rifting initiation, *Earth and Planetary Science Letters*, *430*(C), 1–8.

Zelt, C. A. (1999), Modelling strategies and model assessment for wide-angle seismic traveltime data, *Geophysical Journal International*, pp. 183–204.

Zelt, C. A., and P. J. Barton (1998), Three-dimensional seismic refraction tomography: A comparison of two methods applied to data from the Faeroe Basin, *Journal of Geophysical Research*, *103*(4), 7187–7210.

Zha, Y., S. C. Webb, and W. Menke (2013), Determining the orientations of ocean bottom seismometers using ambient noise correlation, *Geophysical Research Letters*, *40*(14), 3585–3590.

Zha, Y., S. C. Webb, S. S. Wei, D. A. Wiens, D. K. Blackman, W. Menke, R. A. Dunn, and J. A. Conder (2014), Seismological imaging of ridge–arc interaction beneath the Eastern Lau Spreading Center from OBS ambient noise tomography, *Earth and Planetary Science Letters*, *408*(C), 194–206.

Appendices

A APPENDIX A

This appendix includes supplementary materials that accompanies Chapter 2 and has been published with *Accardo, N. J. et al. (2017), Surface wave imaging of the weakly extended Malawi Rift from ambient-noise and teleseismic Rayleigh waves from onshore and lake-bottom seismometers, Geophys. J. Int., 209(3), 1892-1905, doi:10.1093/gji/ggx133..*

A.1 Introduction

This supplement includes a figure showing estimates of standard deviation on the teleseismic phase velocity estimates (Figure A.1), a figure showing the number of crossing interstation ray paths for a given cell for the teleseismic phase velocity processing (Figure A.2), a checkerboard resolution test for the ambient-noise phase velocity measurements (Figure A.3), a figure showing the number of crossing interstation ray paths for a given cell for the ambient noise processing (Figure A.4), and a figure comparing absolute phase velocity determined from ambient-noise and teleseismic Rayleigh waves (Figure A.5).

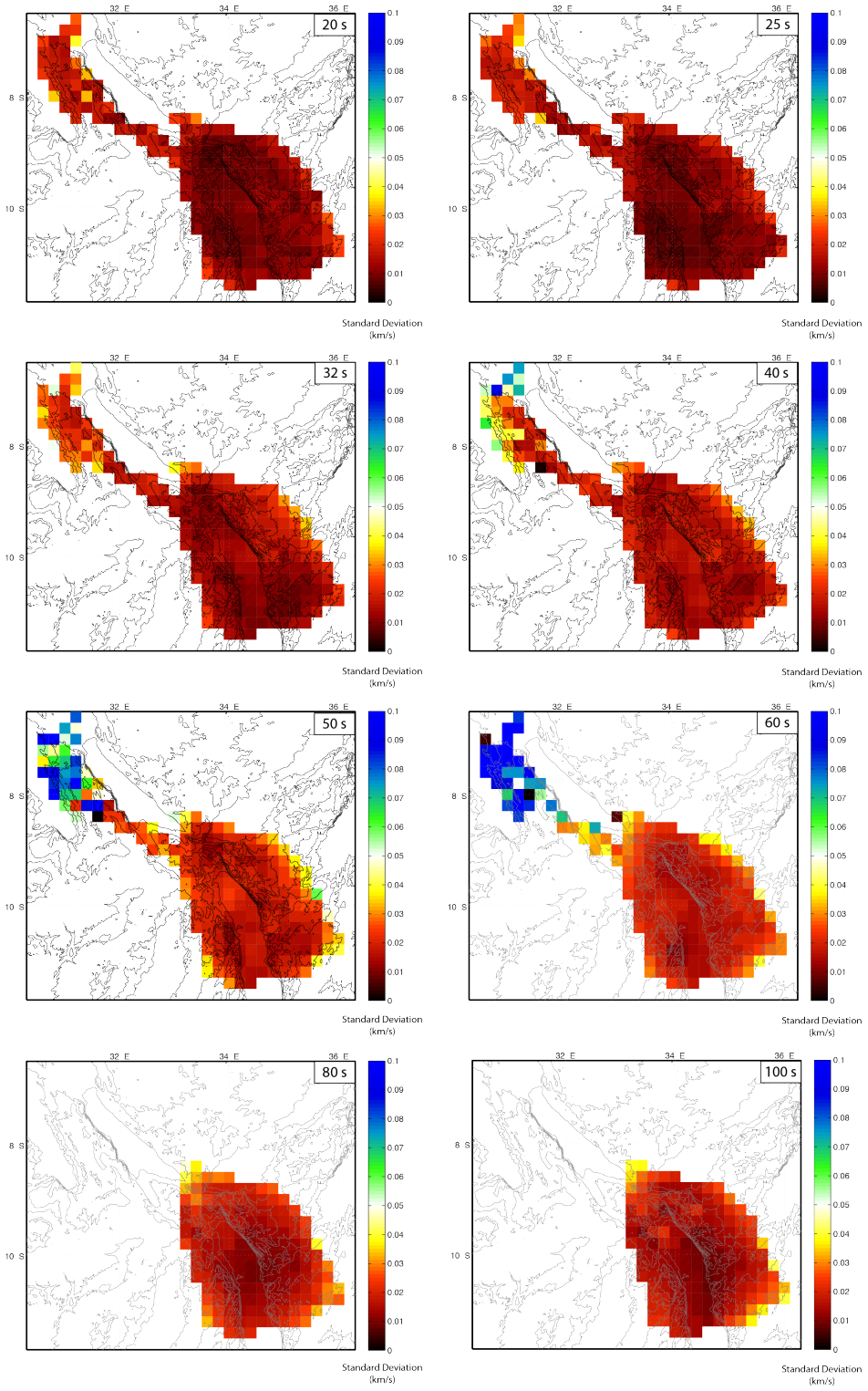

Figure A.1: Estimates of standard deviation of the mean of phase velocity measurements calculated via Helmholtz tomography. Individual event phase velocity maps are stacked to estimate structural phase velocity which allows for the straight forward estimate of standard deviation. The period of interest is shown in the top right of each panel. All color scales range from 0 to 0.1. Grey contours indicate regional elevation.

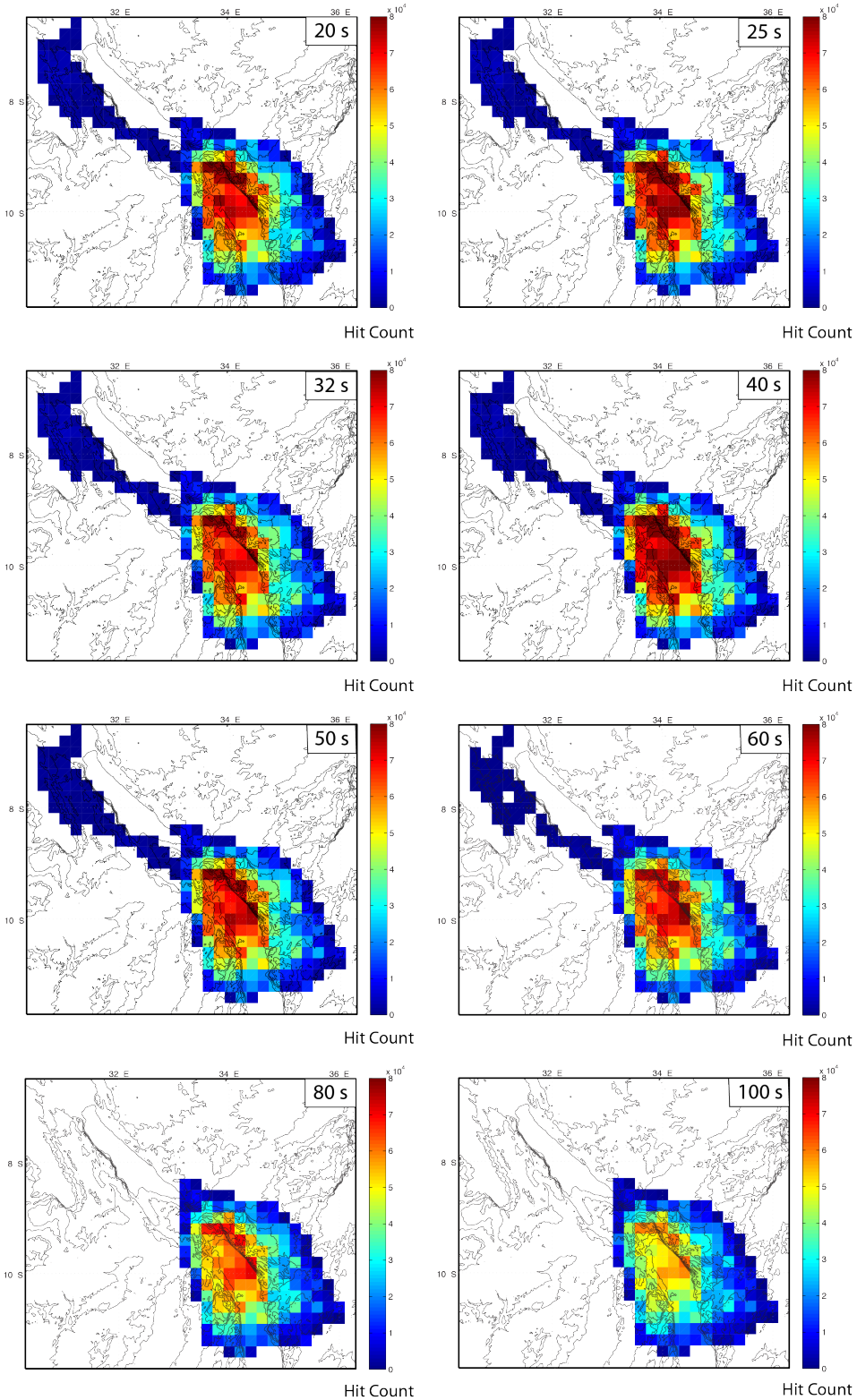

Figure A.2: Maps of the number of interstation ray-paths for a given cell at the periods of interest used when determining teleseismic phase velocity. The color scale is constant across all periods.

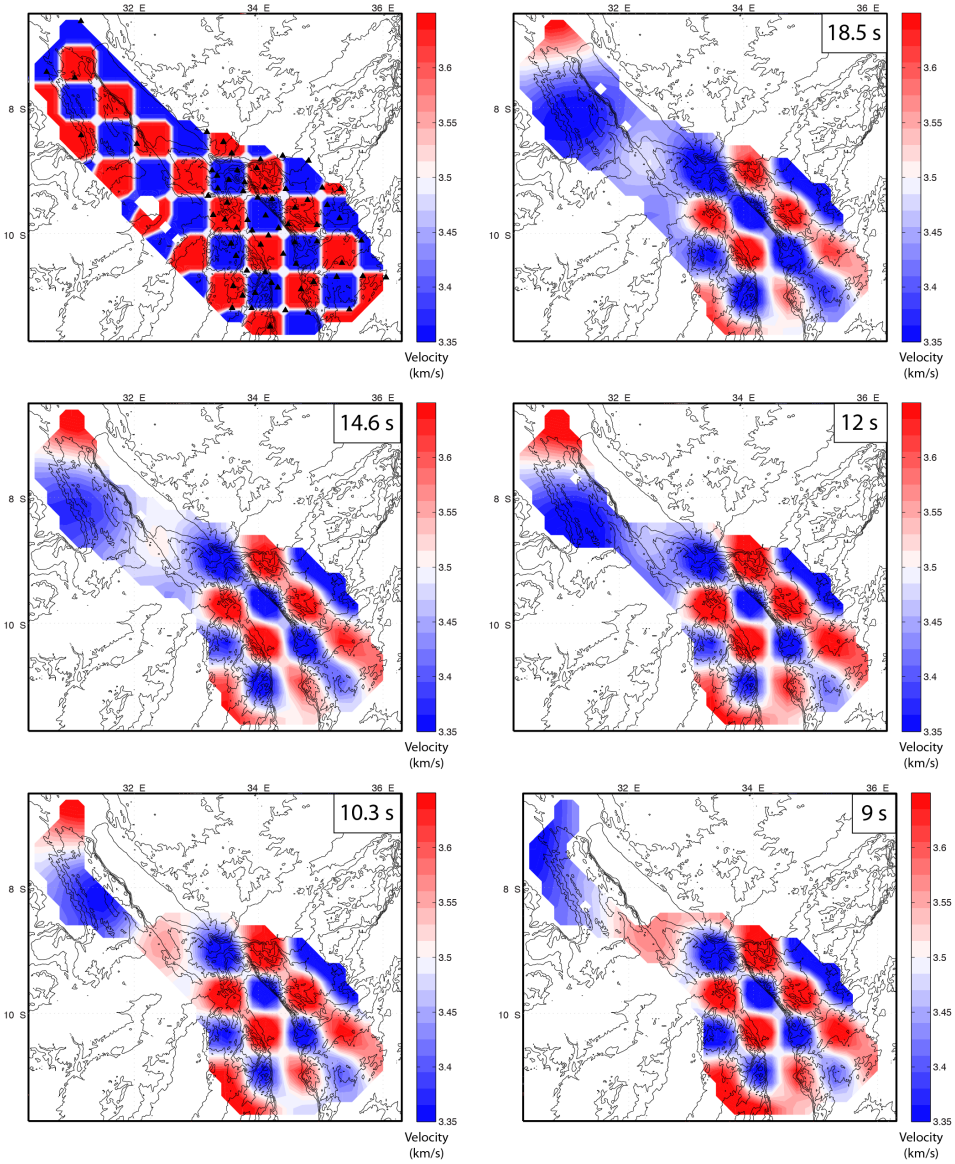

Figure A.3: Results of a checkboard test of the ambient noise tomography at all periods used in this study. Checkerboard squares are 0.6x0.6. The top left panel shows the input grids and the resulting grids are shown in the remaining panels. The period of observation is given in the top right-hand corner of each panel. Color bars give the input/output phase velocity.

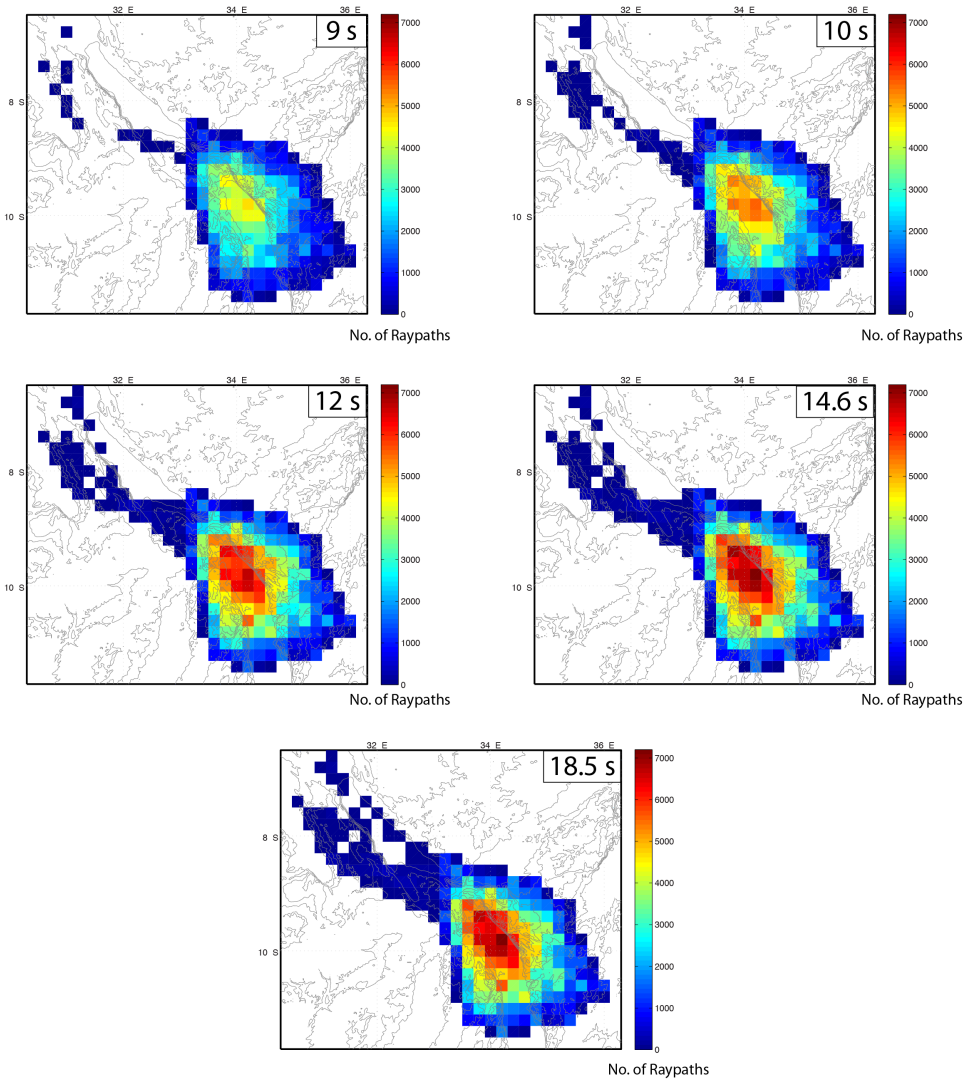

Figure A.4: Maps of the number of crossing interstation ray-paths used in the determination of ambient-noise phase velocity. The color scale is constant across all periods.

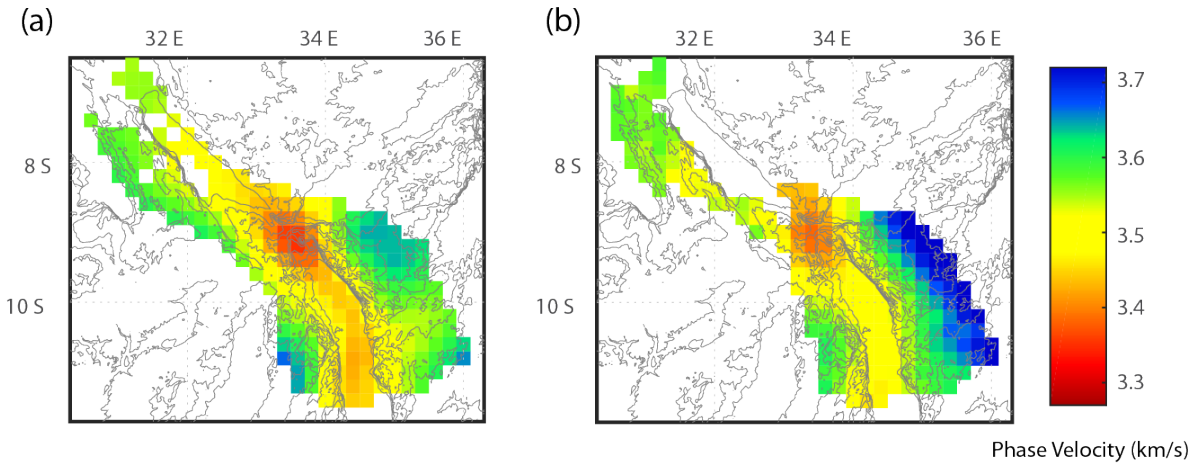

Figure A.5: (a) Phase velocity measured from ambient noise Rayleigh waves at 20 s. (b) Phase velocity measured from teleseismic Rayleigh waves at 20 s.

B | APPENDIX B

This appendix includes supplementary materials for Chapter 3: *The Growth and Interaction of Large Border Faults in the Malawi Rift revealed by 3D Seismic Refraction Imaging*

B.1 Introduction

This supplement includes Section B2 and Figures B.1-B.3 detailing the analysis steps taken to estimate the elevation profile for the footwalls of the Usisya and Livingstone faults. An iterative procedure was implemented to minimize the influence of low elevations due to erosional features.

B.2 Method to Estimate Elevation of Footwall Escarpment

We estimate elevation profiles along the Usisya and Livingstone faults using the 30-m digital elevation model (DEM) provided by the Shuttle Radar Topography Mission (SRTM) (*Farr et al.*, 2007). In the first step, we follow the method of *Ellis and Barnes* (2015) to extract profiles of elevation orthogonal to the strike of the border fault (structural dip direction). The measured height of the footwall is then taken as the maximum elevation within each orthogonal profile. We approximate the strike of the border fault following the visible onshore topographic scarp (Fig. B.1). By making the orthogonal profiles sufficiently long (7 km), we ensure that we capture the maximum footwall elevation regardless of the specific interpretation of the footwall strike (Fig. B.2).

To minimize the influence of secondary erosional features, such as river valleys, we next implement an iterative procedure to down-weight anomalously low elevations. We split the elevation profile for each fault into 14-km-long segments along strike. To identify anomalously low elevations, we calculate the Z-score of each point within the segment. Z-scores are defined as:

$$Z = \frac{X - \mu}{\sigma} \tag{B.1}$$

where X is the elevation for a given point, μ represents the mean of elevation within the segment, and σ represents the standard deviation of all elevations within the segment. We iteratively discard all elevations with Z-scores less than -1. We then recalculate the mean, standard deviation, and Z-scores. We continue this process until changes in the mean elevation are less than 20 m (typically <5 iterations). During this process, we do not discard the endpoints of the fault so as to ensure that the long-wavelength character of the fault is not lost. To further down-weight low elevations missed in our Z-score analysis, we fit the data with a 5th order polynomial and remove all elevation points that are more than 30 m below the polynomial line. We then refit the remaining data with a 5th order polynomial and use that polynomial as our final elevation profile (Figure B.3).

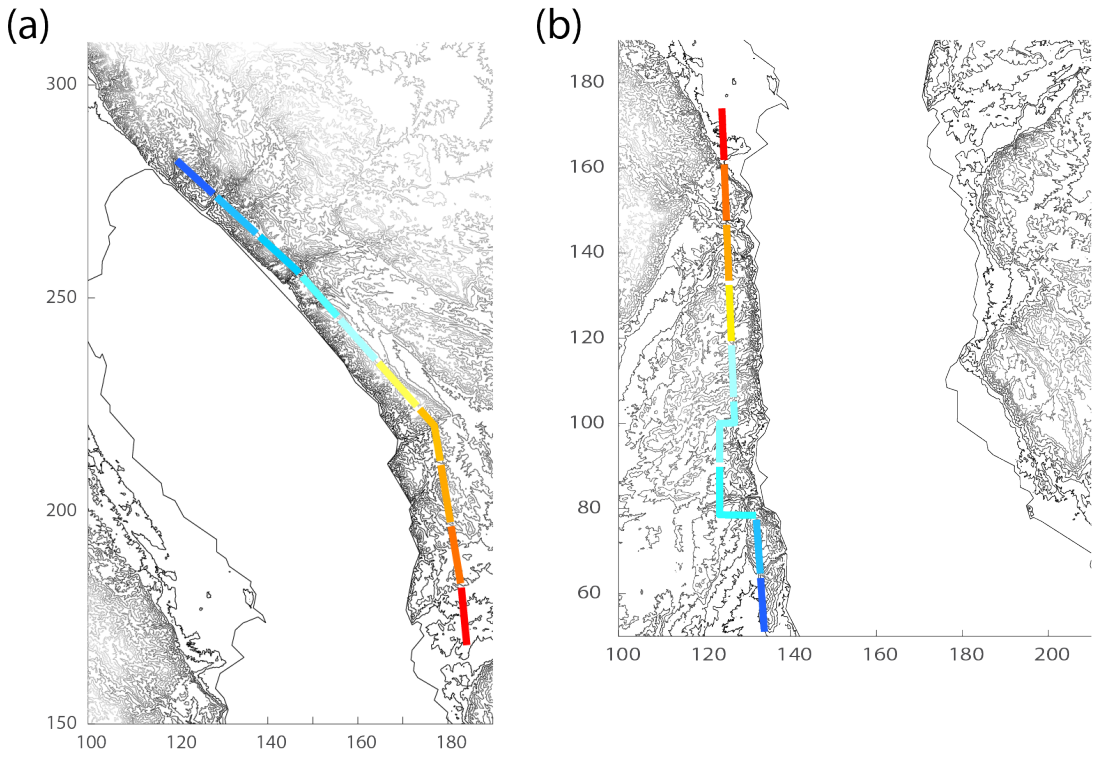

Figure B.1: Map showing our visually defined strike lines along the (a) Livingstone and (b) Usisya faults. Colors indicate the different segments used when calculating the Z-scores of the elevation.

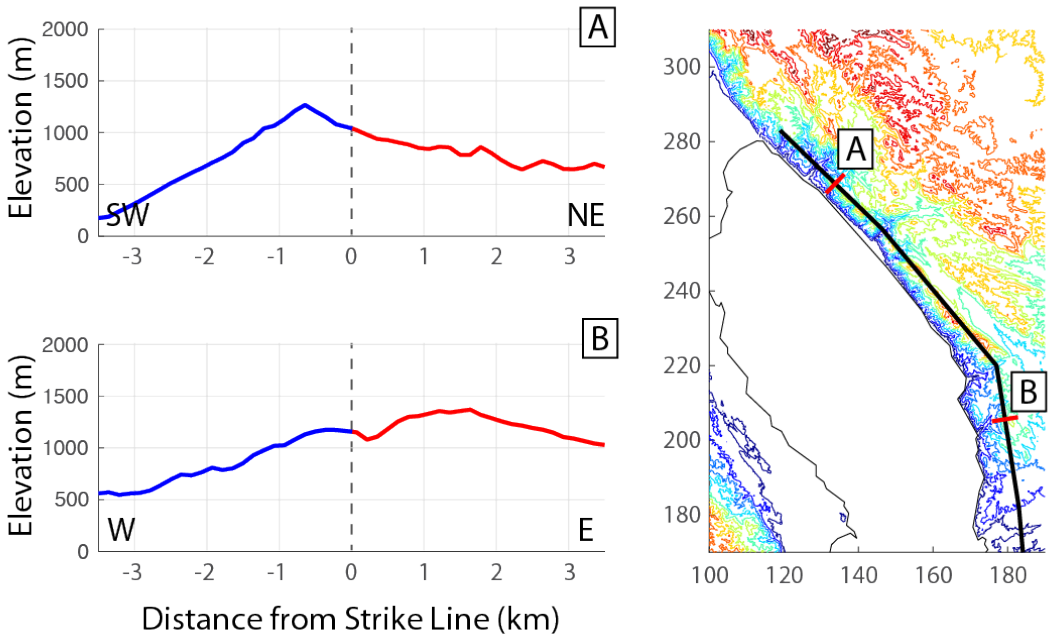

Figure B.2: (left) Examples of elevations extracted orthogonal to the strike line of the Livingstone Fault. Dashed line at 0 indicates the location of the strike line. Location for these two elevation profiles are shown in the map (right). Background shows contours of elevation. All elevations are given with respect to lake level (454 m) and coordinates of the map are given in the local coordinate system as detailed in Section 3.3.2 of the manuscript.

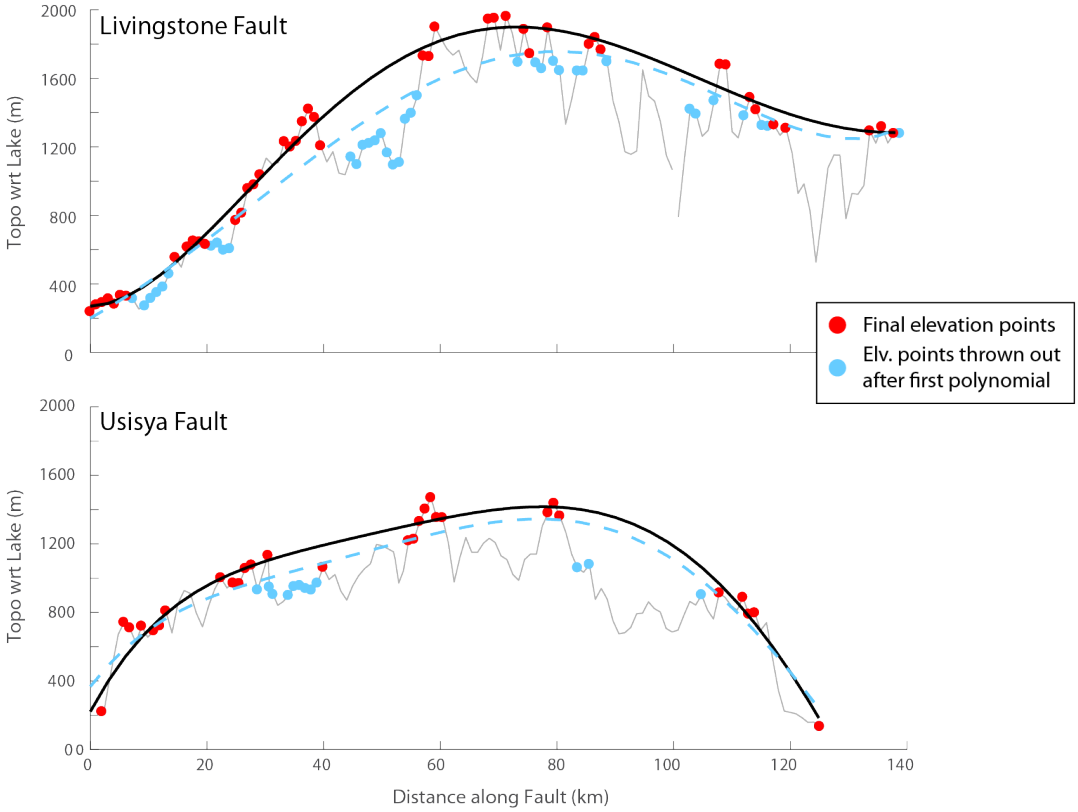

Figure B.3: Example showing evolution of the elevation profiles during our iterative procedure for the Livingstone (top) and Usisya (bottom) faults. The thin grey line depicts the original elevation profile. Blue points are data that were accepted based on their Z-scores but then thrown out after the first polynomial fitting (dashed blue line). Red points represent the final elevation points that are then fit with the second polynomial (black line). This second polynomial represents the final elevation profile. All elevations are given with respect to lake level (454 m). Both profiles are from South (left) to North (right)

C | APPENDIX C

This appendix includes supplementary materials for Chapter 4: *Crust and upper mantle shear velocity structure beneath the weakly-extended Malawi Rift with comparison to the mature Main Ethiopian Rift*

C.1 Datasets in the Main Ethiopian Rift and Afar Depression

This study leverages the extensive previous instrumentation of Afar, Ethiopia that began in 1999. We obtained vertical component seismograms recorded on seven co-located temporary arrays, two Global Seismograph Network stations (FURI, ATD), and three Africa Array stations (beginning in 2006) for a total of 107 stations (Fig. C.1). Three temporary arrays were deployed in the area beginning in ∼1999 and ending in early 2003 (Ethiopia Afar Geoscientific Lithospheric Experiment; *Bastow et al.* (2011), Ethiopia Kenya Broadband Seismic Experiment; *Nyblade and Langston* (2002); and the Horn of Africa experiment). From 2007-2009 two temporary arrays operated with footprints limited to the Afar Depression (Afar2007 and Afar Consortium Network). Between 2009 to 2011, two additional experiments operated in the Afar Depression (Afar2009 and Afar Depression Dense Seismic Array). The combined networks give a combined aperture of ∼ 700 km with minimum station spacing of <40 km allowing for reliable measurements of Rayleigh waves from ambient-noise processing between 9 and 20 s and from teleseismic processing between 25 and 100 s period. Instrument types range from short-period to broadband thus measurements at the longest periods were only made on the broadband instruments.

For ambient-noise processing, we acquired all available continuous data in 12-hour segments for the 107 stations in the study region. For the teleseismic processing we initially selected all events with Ms greater than 6.0 between epicentral distances of 5°and 120°. The resulting traces

show highly scattered yet coherent energy within the surface wave coda likely stemming from the extremely heterogeneous structure of region at depth. Therefore, we exercised tight quality control constraints and only included events with the highest signal-to-noise-ratios. Figure C.2 shows the distribution of 199 events used for this study. All seismic traces both for the ambient noise and the teleseismic processing were deconvolved from their respective instrument response and downsampled to a sample rate of 1 Hz to ensure consistency across experiments. Figure C.3 shows an example record section used in the teleseismic processing and cross-correlation waveforms for station FURI used in the ambient noise processing.

C.2 Determination of phase velocity maps for Ethiopia

To construct 2-D Rayleigh wave phase velocity maps between 9 and 100 s for the Ethiopian study region, we follow the same analysis steps presented in *Accardo et al.* (2017). Briefly, ambient noise processing is done following the method of *Menke and Jin* (2015), which aims to estimate phase velocity from ambient-noise cross-correlograms in the frequency domain via waveform fitting using Aki's formula. Construction of phase velocity maps from teleseismic surface waves is done following the method of *Jin and Gaherty* (2015). This method recovers frequency-dependent phase and amplitude information via the narrow-band filtering of the broadband (10-150 s) cross-correlation function between the vertical-component seismic trace from a given station and time-windowed traces from all stations with interstation distances between 20-200 km. The method of *Jin and Gaherty* (2015) leverages amplitude information to correct for focusing and defocusing effects via Helmholtz tomography (*Lin and Ritzwoller*, 2011). Following the implementation of Accardo et al. [2017], we calculate station amplification terms and correct event-specific amplitude fields to minimize the influence of local geology and instrument/installation conditions prior to applying Helmholtz tomography. We tested the influence of damping/smoothness choices in the inversion step for both the ambient noise and teleseismic processing and chose those parameters that provided the best fit to the data while maintaining realistic variations in phase velocity. Figure C.4 presents the maps of phase velocity for the study region. Figure C.5 show the number of crossing interstation ray-paths used in the determination of phase velocity. We perform checkerboard resolution tests to understand the scale of anomalies we can resolve from both ambient noise and teleseismic phase velocities. Recovered models from the checkerboard tests are shown for teleseismic periods in Figure

C.6 and for ambient noise periods in Figure C.7.

C.3 Shear Velocity Inversion

We follow the same procedure outlined in Section 4.3.2 to invert individual dispersion curves from 9 - 100 s for each grid point within the study region for 1-D profiles of shear velocity. This is a Monte Carlo approach that aims to minimize the influence of choices in construction of the initial model as well as allow direct access to the model uncertainty. We use constraints on sediment and crustal thickness (*Dugda et al.*, 2005; *Hammond et al.*, 2011; *Stuart et al.*, 2006; *Keranen and Horne*, 2014) to guide the construction of the family of starting models and add Gaussian perturbations to randomize the models. Figure S8 shows a map of Moho-depth across the study region that we used to construct the starting models. Table C.1 shows the allowed perturbations to layer velocities and velocity interfaces. We use the *surf96* program (*Herrmann*, 2013) to invert the 100 unique starting models and discard the models with the largest misfits to the data (>20% above average misfit). The final model for a given grid point is taken as the mean of the best fitting models. The final 3-D model for the study region is constructed by combining the 1-D shear velocities from all grid points in the study region.

C.4 Results of Shear Velocity Inversion

Figure S9 shows depth slices and a cross-section through the final shear velocity model of the MER and Afar Depression. A broad low-velocity zone (LVZ) is imaged between ∼80-135 km across the entire study region with the slowest velocities at the juncture between the MER and Afar and in the southern MER. Velocities within the LVZ average ∼4.05-4.15 km/s and shallow from the southwest to the northeast. A pronounced high-velocity lithospheric lid is imaged beneath both the Ethiopian and Somalian plateaus with velocities >4.4 km/s reaching depths ∼ 70 km beneath the Ethiopian Plateau and ∼ 50 km depth beneath the Eastern Plateau. As observed in previous studies, a similarly fast velocity lithospheric lid is absent along the rift axis (*Bastow et al.*, 2008; *Gallacher et al.*, 2016). At the crustal scale we image similar structure to that of previous ambient noise studies (*Kim et al.*, 2012; *Guidarelli et al.*, 2011; *Korostelev et al.*, 2015) with low velocities associated with MER rift axis, locations of rift flank volcanism, and magmatic segments within the Afar depression.

Table C.1: Allowed perturbations to the starting models for the shear velocity inversion for the Main Ethiopian Rift and Afar Depression.

Parameter	**Allowed perturbation**
Sediment Velocity	±10%
Crustal Velocity	±10%
Mantle Velocity	±10%
Sediment Thickness	±1 km
Moho Depth	±5 km

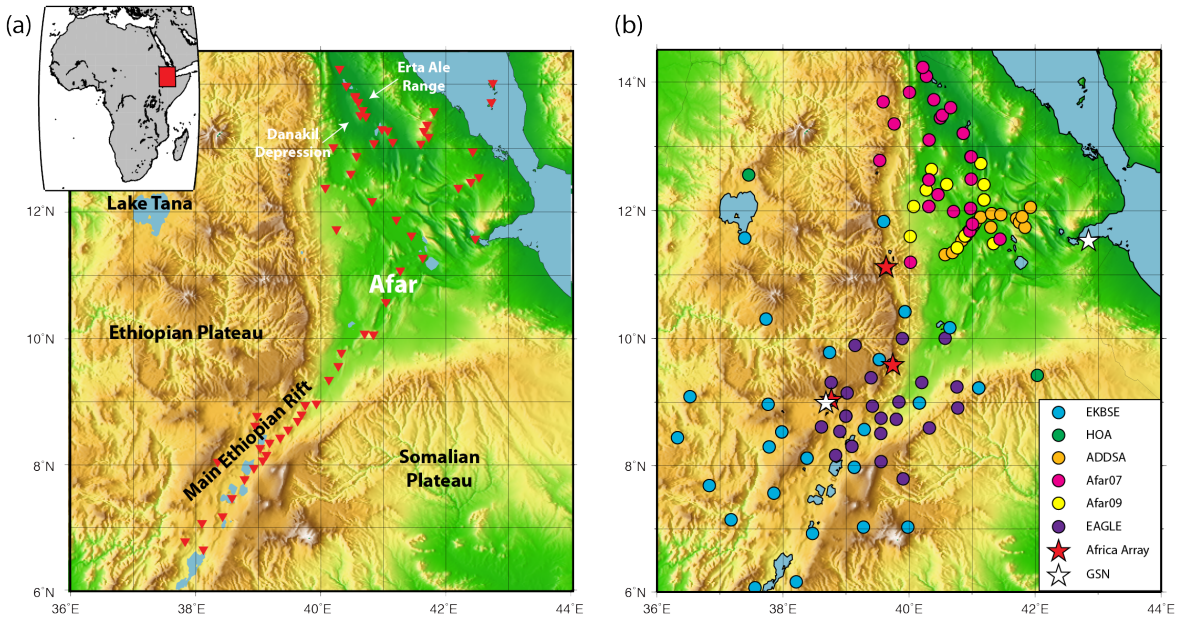

Figure C.1: Map of the Ethiopian study region showing locations of interest (a) and station locations (b). Red triangles in (a) show the locations of Quaternary-recent active volcanos from the Global Volcanism Program (*Venzke et al.*, 2002). The inset map in (a) shows the location of the study region. The inset key in (b) labels the different temporary arrays and permanent stations used in this study.

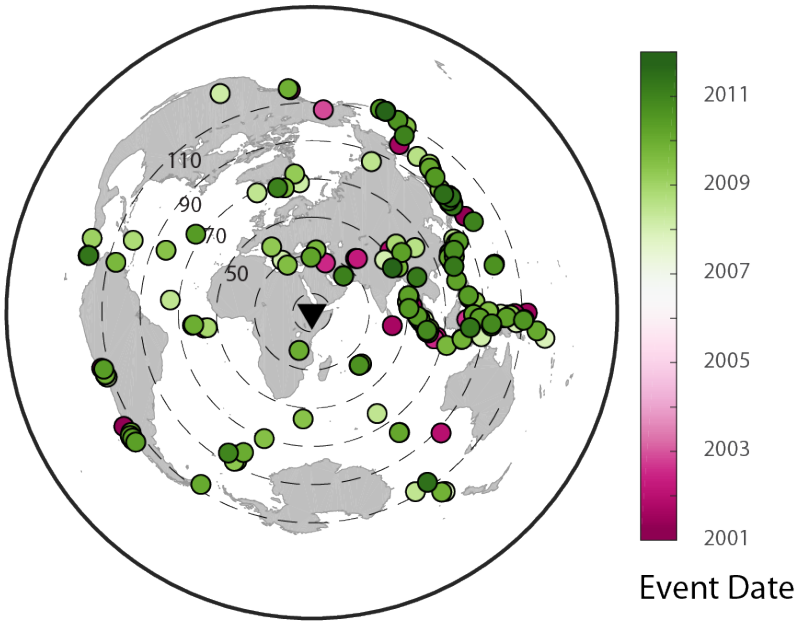

Figure C.2: Distribution of events used to determine teleseismic Rayleigh wave phase velocities between 2001 and 2011. The color of the symbols denote the date of the event.

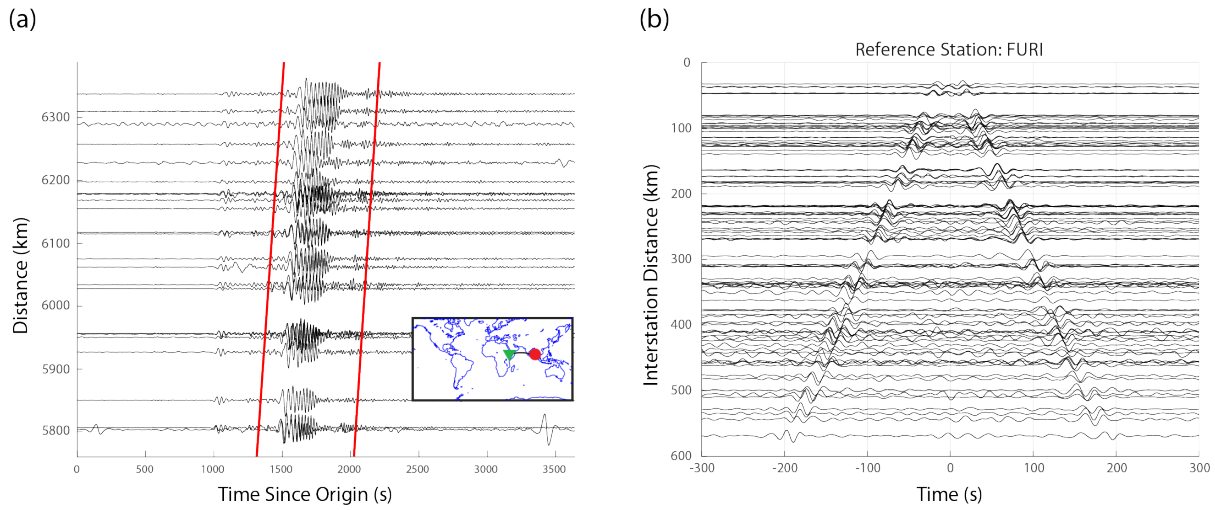

Figure C.3: Data examples from the networks in the Main Ethiopian Rift and Afar Depression. (a) Rayleigh waves filtered between 10-100 s from the M 6.0 event on March 15, 2001. The inset map shows the location of the event (circle) and the array (triangle). Red lines indicate the window of interest. (b) Ambient noise cross-correlograms for station FURI filtered between 8 - 25 s.

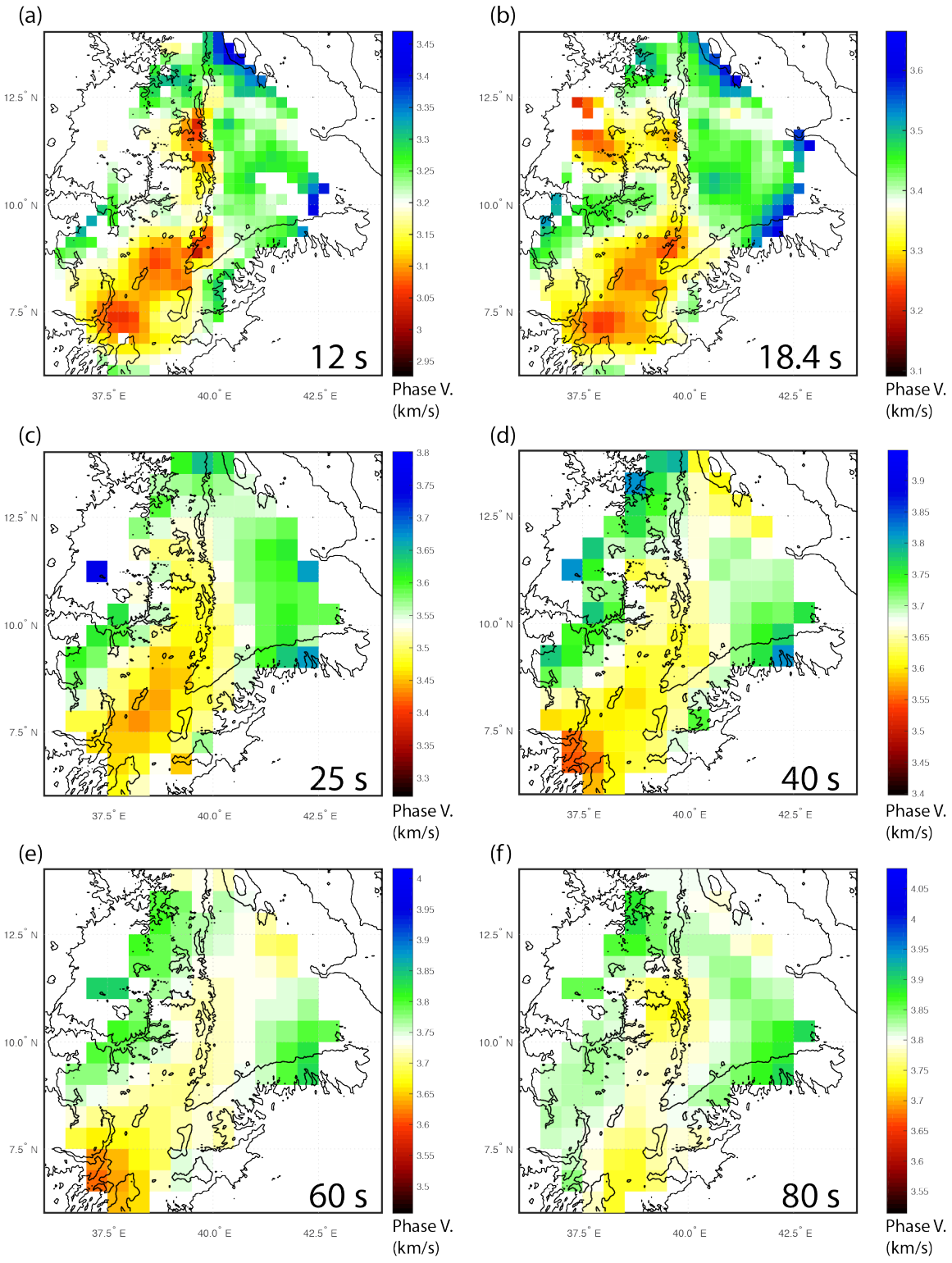

Figure C.4: Maps of phase velocity for ambient noise (a,b) and teleseismic (c-f) Rayleigh waves for periods between 12 and 80 s.

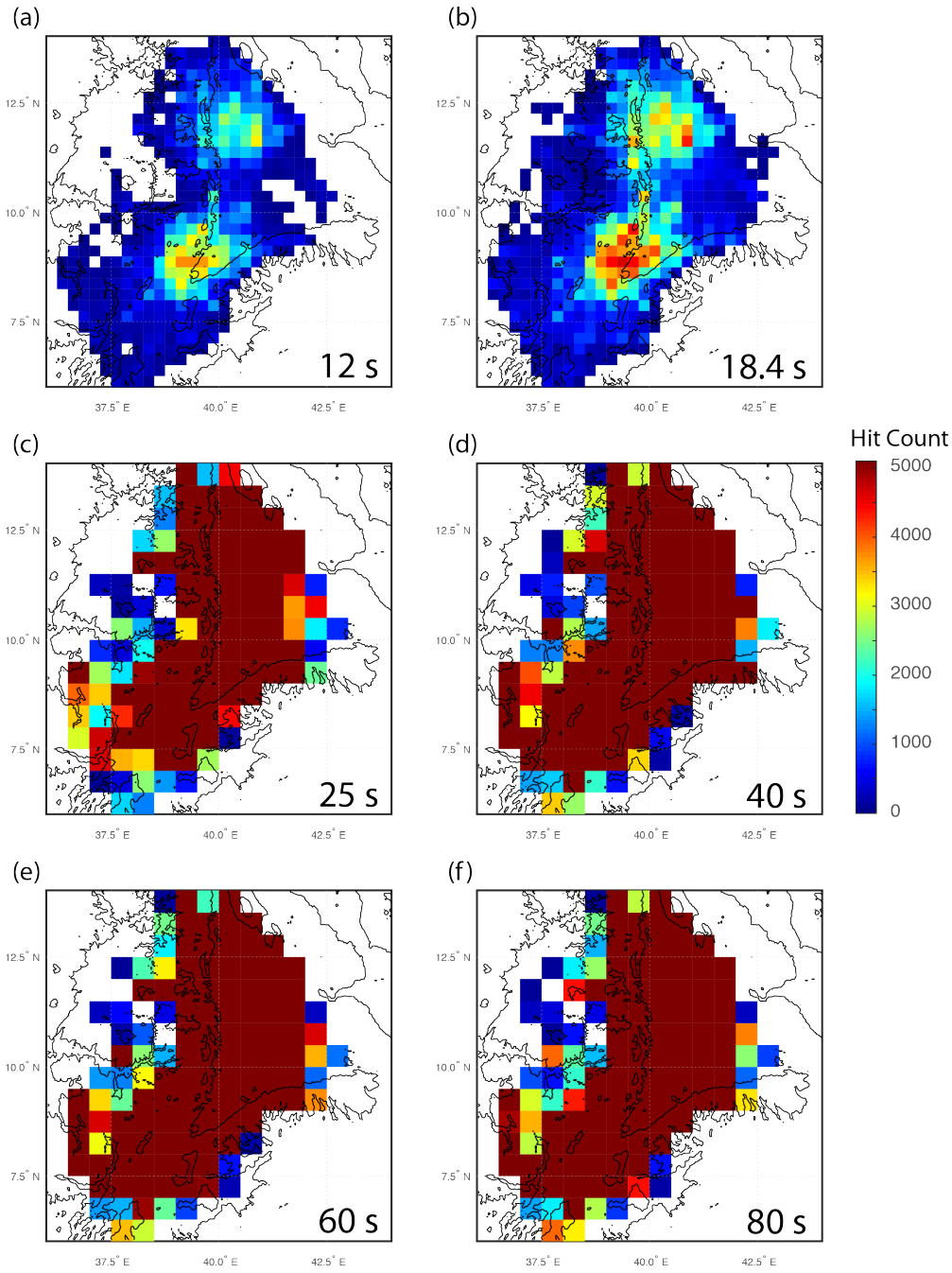

Figure C.5: Maps of the number of interstation ray-paths for ambient noise (a,b) and teleseismic (c-f) Rayleigh wave phase velocities.

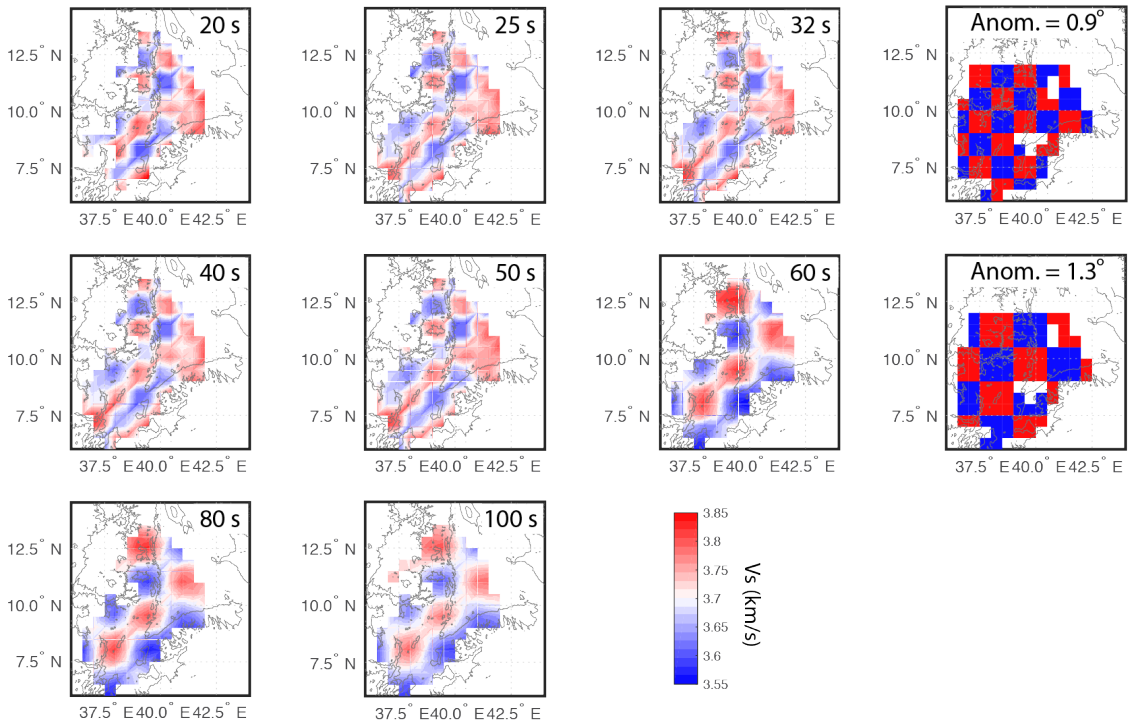

Figure C.6: Checkerboard tests for teleseismic Rayleigh waves with alternating fast and slow anomalies of 0.9°and 1.3°dimension. Two checkerboards for the different anomaly sizes are shown for an example event on the far right. The final recovered model is created by stacking the individual recovered models for each event used in the estimation of phase velocity.

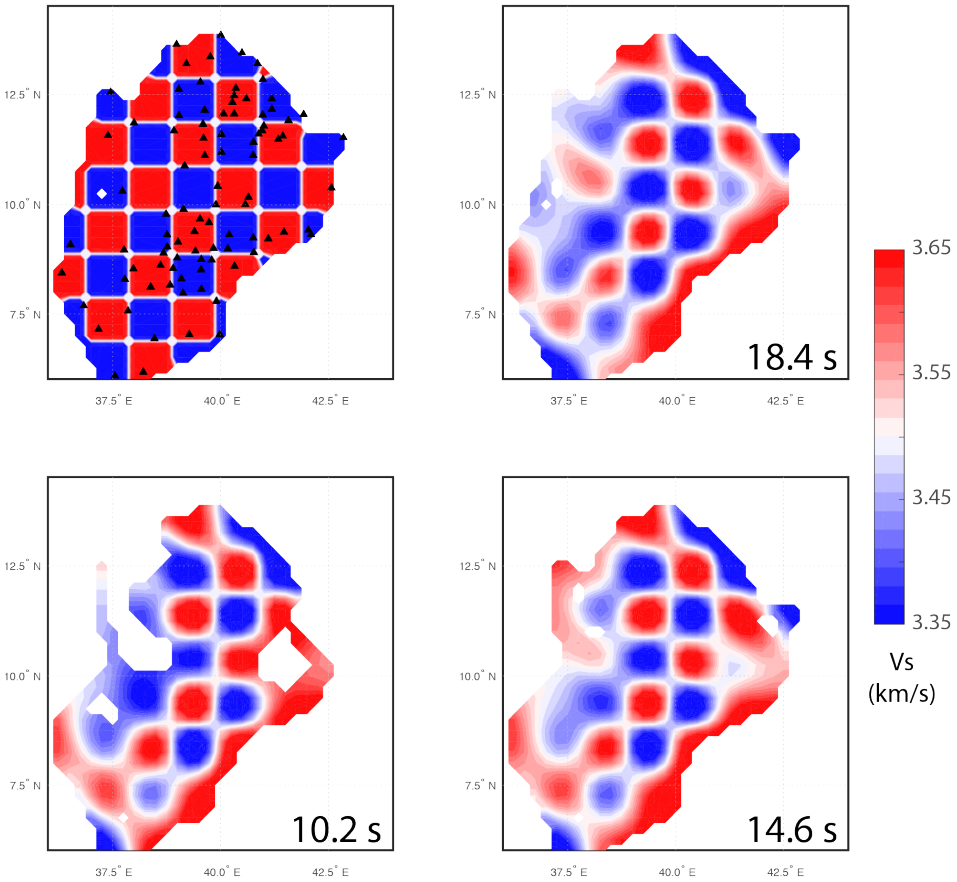

Figure C.7: Checkerboard test for ambient-noise Rayleigh wave phase velocities with anomalies of 0.9°dimension. Input checkerboard is shown in the top left panel with locations of stations shown by black triangles.

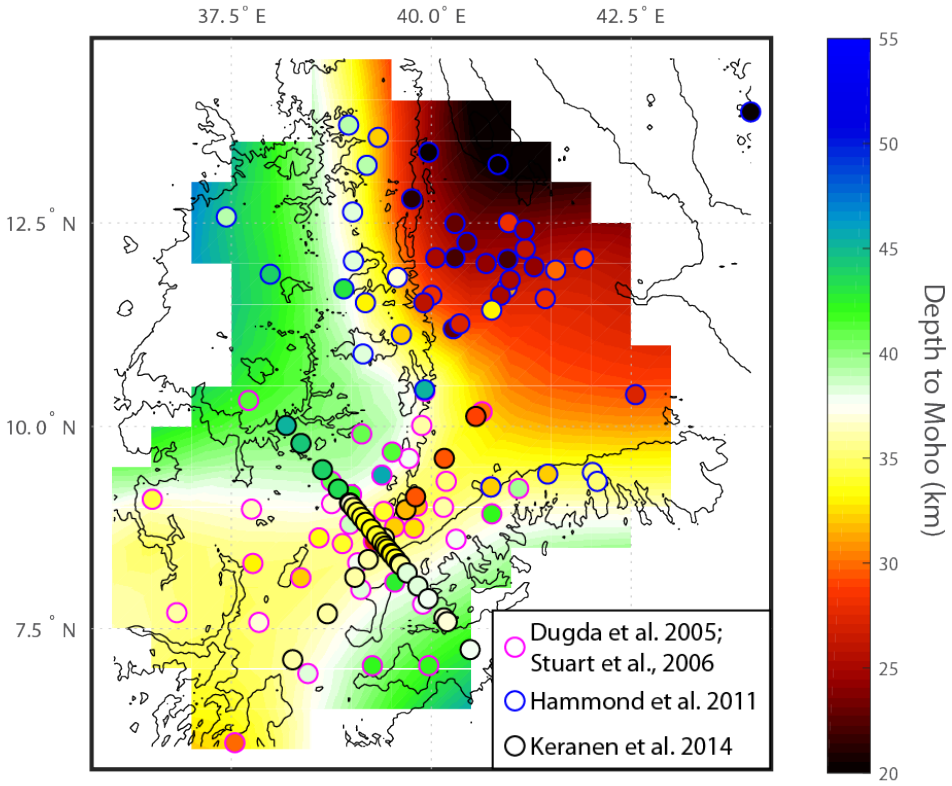

Figure C.8: Map of variation in Moho-depth for the study region using constraints from *Dugda et al.* (2005), *Hammond et al.* (2011), *Stuart et al.* (2006), and *Keranen and Horne* (2014). Circles show locations and estimates of individual measurements of Moho-depth where the color of the outline indicates the source. The background grid shows the calculated surface fit to the individual measurements.

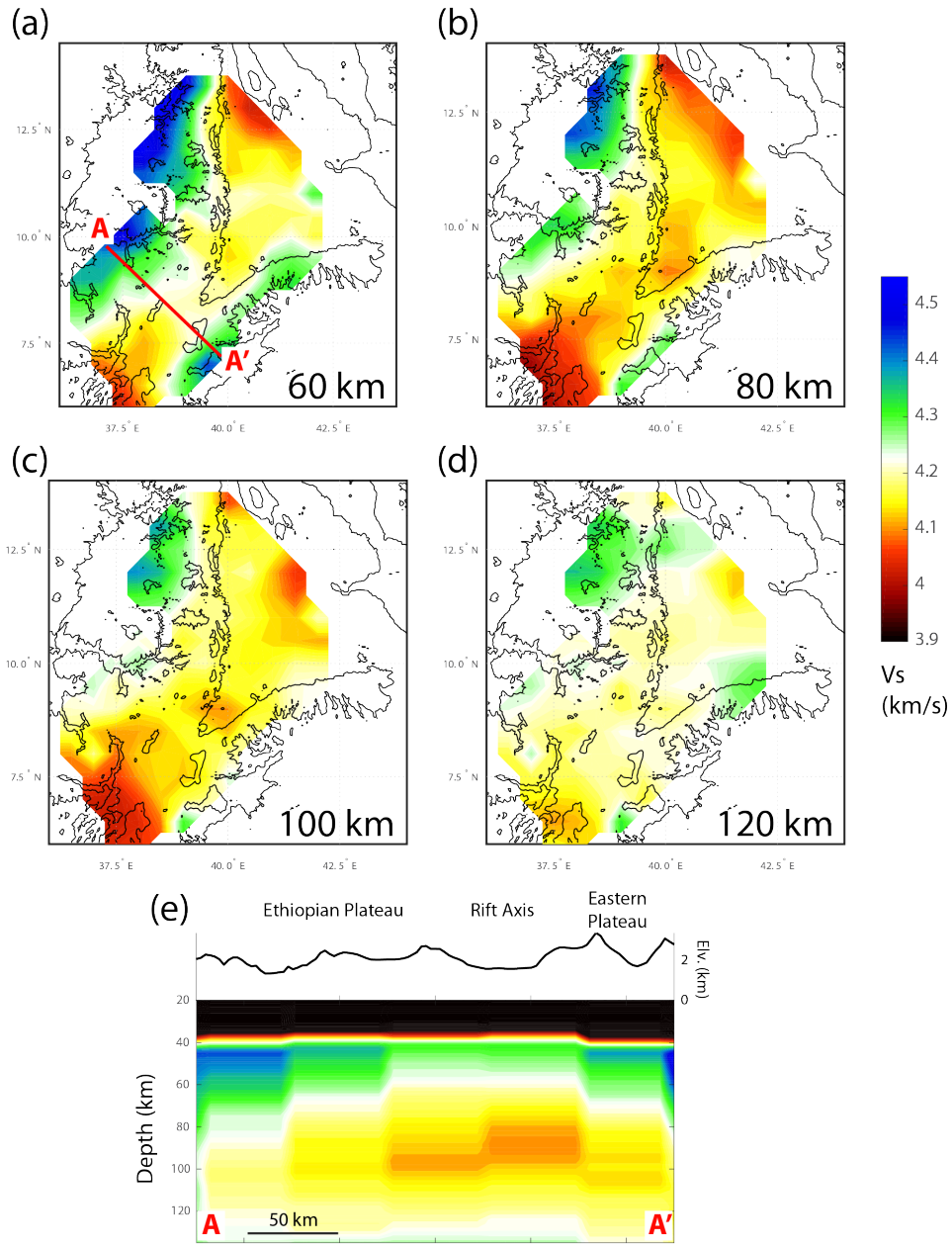

Figure C.9: Depth slices (a-d) and a cross-section through the shear velocity model of the Main Ethiopian Rift and Afar Depression. The location of the cross-section is shown in (a). The velocity color scale is constant across all figures. Elevation and locations of interest are shown in (e) above the model cross-section.